Western Graduate&PostdoctoralStudies

Western University
Scholarship@Western

Electronic Thesis and Dissertation Repository

11-8-2013 12:00 AM

Two dimensional angular domain optical imaging in biological tissues

Eldon Ng, *The University of Western Ontario*

Supervisor: Jeffrey J.L. Carson, *The University of Western Ontario*

A thesis submitted in partial fulfillment of the requirements for the Master of Science degree in Medical Biophysics

© Eldon Ng 2013

Follow this and additional works at: https://ir.lib.uwo.ca/etd

Part of the Optics Commons

Recommended Citation

Ng, Eldon, "Two dimensional angular domain optical imaging in biological tissues" (2013). *Electronic Thesis and Dissertation Repository*. 1796.
https://ir.lib.uwo.ca/etd/1796

This Dissertation/Thesis is brought to you for free and open access by Scholarship@Western. It has been accepted for inclusion in Electronic Thesis and Dissertation Repository by an authorized administrator of Scholarship@Western. For more information, please contact wlswadmin@uwo.ca.

TWO DIMENSIONAL ANGULAR DOMAIN OPTICAL IMAGING IN BIOLOGICAL TISSUES

(Thesis format: Integrated Article)

by

Eldon Ng

Graduate Program in Medical Biophysics

A thesis submitted in partial fulfillment
of the requirements for the degree of
Master of Science

The School of Graduate and Postdoctoral Studies
The University of Western Ontario
London, Ontario, Canada

© Eldon Ng 2013

Abstract

Optical imaging is a modality that can detect optical contrast within a biological sample that is not detectable with other conventional imaging techniques. Optical trans-illumination images of tissue samples are degraded by optical scatter. Angular Domain Imaging (ADI) is an optical imaging technique that filters scattered photons based on the trajectory of the photons. Previous angular filters were limited to one-dimensional arrays, greatly limiting the imaging capability of the system.

We have developed a 2D Angular Filter Array (AFA) that is capable of acquiring two-dimensional projection images of a sample. The AFA was constructed using rapid prototyping techniques. The contrast and the resolution of the AFA were evaluated. The results suggest that a 2D AFA can be used to acquire two-dimensional projection images of a sample with a reduced acquisition time compared to a scanning 1D AFA.

Keywords

Optical imaging, angular domain imaging, angular filter array, trans-illumination imaging, contrast analysis, resolution analysis, structured illumination, digital light processing

Co-Authorship Statement

This section describes the contribution from various authors for the work completed in Chapters 2 and 3 as well as Appendices 1 and 2.

Chapter 2: E. Ng, J. J. L. Carson. "Angular domain imaging with a 2D angular filter array," Article in preparation for submission to Applied Optics.

Dr. Carson aided in the project design and the experimental direction. I aided in the design and the construction of the angular filters. I designed and conducted the experiments, analyzed the results, and wrote the manuscript.

Chapter 3: E. Ng, J. J. L. Carson. "Two-dimensional angular domain imaging with a 3D printed angular filter," Article in preparation for submission to Applied Optics.

Dr. Carson aided in the project design and the experimental direction. I designed and constructed the imaging system. I designed and conducted the experiments and I analyzed the results and wrote the manuscript.

Appendix A: E. Ng, F. Vasefi, B. Kaminska, J. J. L. Carson, "Three-dimensional angular domain optical projection tomography," SPIE Annual Meeting, Symposium on Biomedical Optics (BiOS) 7897-0V, (2011).

Dr. Carson aided in the project design and the experimental direction. Dr. Vasefi provided insight on angular domain imaging. I designed and constructed the imaging system. I wrote the software needed to conduct the experiments and to automate image acquisition. I designed and conducted the experiments analyzed and interpreted the results and wrote the manuscript.

Appendix B: E. Ng, F. Vasefi, J. J. L. Carson, "Multispectral angular domain imaging with a tunable pulsed laser," SPIE Annual Meeting, Symposium on Biomedical Optics (BiOS) 8225-2C, (2012).

Dr. Carson aided in the project design and the experimental direction. Dr. Vasefi provided insight on angular domain imaging and multispectral imaging. I designed and constructed the imaging system. I wrote the software needed to conduct the experiments and to automate image acquisition. I designed and conducted the experiments analyzed and interpreted the results and wrote the manuscript.

Acknowledgements

Dr. Carson, the passion that you show towards your life inside and outside of the lab is inspiring. I would not be where I am today without your mentorship and motivation.

Dr. Mo-Reza, you have kept my stomach full and happy for the past few years. Thank you for all of your help.

Dr. Vasefi, you have taught me a great deal over the years. It was a great experience to work alongside you and to cultivate new ideas together.

To all the people at the Carson Lab, you have made the past few years fun and exciting. Thank you Astrid, Michelle, Pinhas, Michael, Gen, Ivan, Pantea, Avery, Phil, Esther, Candice, and Camilla.

Finally, I would like to acknowledge the financial support provided by UWO, SPIE, the Translational Breast Cancer Research Unit, Canadian Institutes of Health Research, and the Natural Sciences and Engineering Research Council of Canada.

Table of Contents

Abstract ii

Keywords ii

Co-Authorship Statement iii

Acknowledgements v

Table of Contents vi

Table of Figures xv

List of Appendices xx

List of Abbreviations and Symbols xxi

Preface xxiii

Chapter 1 1

1 Introduction 1

1.1 Medical Imaging 2

1.2 Optical Imaging 3

1.3 Light Tissue Interactions 3

1.4 Overview of Optical Imaging Modalities 6

1.4.1 Optical Coherence Tomography 6

1.4.2 Time domain imaging 7

1.4.3 Diffuse optical tomography 8

1.4.4 Hybrid optical ultrasound imaging 8

1.5 Angular Domain Imaging (ADI) 9

1.5.1 Fourier-based ADI 10

1.5.2 Lensless ADI 11

1.5.3 ADI simulations 12

1.6 Previous AFA design 15

1.6.1 Silicon AFA fabrication process 15

1.6.2 Chemically etched AFAs 16

1.6.3 Deep Reactive Ion Etching AFAs 16

1.6.4 Internal reflections 16

1.7 ADI Illumination sources 18

1.8 Previous ADI studies 19

1.8.1 Hybrid ADI systems 19

1.8.2 Background scatter estimation 19

1.8.3 Deep illumination ADI 20

1.8.4 Tomographic ADI 21

1.8.5 Fluorescence ADI 22

1.8.6 Multispectral and Hyperspectral ADI 22

1.9 Motivation 23

1.10 Thesis objective and scope 25

1.11 References 26

Chapter 2 31

2 Angular domain imaging with a 2D angular filter array 31

2.1 Introduction 31

2.1.1 Optical trans-illumination imaging 31

2.1.2 Angular Domain Imaging (ADI) 32

2.1.3 Dependence of ADI on illumination geometry 33

2.1.4 Dependence of ADI contrast on AFA aspect ratio 33

2.1.5 Background scatter estimation in ADI 34

2.1.6 Objective and approach 35

2.2 Methods 36

2.2.1 Fabrication of the 2D AFA 36

2.2.2 Illumination and detection 37

2.2.3 Imaging Target 38

2.2.4 Image collection 39

2.2.5 Analysis of fabricated 2D AFAs 39

2.2.6 Contrast with sparsely structured illumination 39

2.2.7 Contrast with varying aspect ratio 39

2.2.8 Background scatter correction 40

2.2.9 Image Analysis 40

2.3 Results 41

2.3.1 Fabrication of the 2D AFA 41

2.3.2 Contrast with sparsely structured illumination 41

2.3.3 Dependence of contrast on aspect ratio 43

2.3.4 Background scatter estimation 44

2.4 Discussion 46

2.4.1 General 46

2.4.2 Fabrication of the 2D AFA 47

2.4.3 Contrast with structured illumination 48

2.4.4 Contrast with varying acceptance angle 49

2.4.5 Background scatter estimation 51

2.5 Conclusions and future work 52

2.6 Acknowledgements 52

2.7 References 53

Chapter 3 55

3 Two-dimensional angular domain imaging with a 3D printed angular filter array 55

3.1 Introduction 55

3.1.1 Optical trans-illumination imaging 55

3.1.2 Angular Domain Imaging (ADI) 56

3.1.3 Two-Dimensional AFA 57

3.1.4 AFA Scanning 58

3.1.5 Structured illumination 58

3.1.6 AFA channel crosstalk 59

3.1.7 Objective and approach 59

3.2 Methods 60

3.2.1 AFA fabrication 60

3.2.2 Illumination and detection 62

3.2.3 Imaging Targets 63

3.2.4 System resolution experiments 64

3.2.5 Channel crosstalk experiments 65

3.2.6 Tissue imaging experiments 65

3.2.7 Image processing and analysis 66

3.3 Results 69

3.3.1 Channel crosstalk 69

3.3.2 Knife edge resolution 70

3.3.3 4 rods absorption target 71

3.3.4 Chicken breast target 73

3.4 Discussion 76

3.4.1 Channel crosstalk 76

3.4.2 Knife edge resolution 76

3.4.3 4 rods absorption target 78

3.4.4 Chicken breast target 79

3.5 Conclusions and future work 81

3.6 Acknowledgements 82

3.7 References 82

Chapter 4 85

4 Discussion and future work 85

4.1 Summary of work 85

4.1.1 System design 85

4.1.2 Experimental studies 86

4.2 Improvements and limitations 86

4.2.1 Benefits 86

4.2.2 Limitations 87

4.3 Illumination and detection improvements 88

4.3.1 Illumination source 88

4.3.2 Structured light 89

4.3.3 Detection 90

4.4 AFA design improvements 90

4.4.1 Discontinuous Walls 91

4.4.2 AFA size & resolution 91

4.5 Experimental design improvements 93

4.5.1 Tissue samples 93

4.5.2 Attenuating targets 94

4.6 Applications 95

4.6.1 Small animal imaging 95

4.6.2 Tissue sample imaging 96

4.7 Conclusions 96

4.8 References 97

Appendix A 98

A Three dimensional angular domain optical projection tomography 98

A.1 INTRODUCTION 98

A.1.1 Trans-illumination imaging 98

A.1.2 Angular domain imaging 99

A.1.3 Angular domain optical projection tomography 100

A.2 Experimental Setup and methods 101

A.2.4 Illumination and detection 101

A.2.5 Imaging target 101

A.2.6 Image pre-processing 102

A.2.7 Tomographic reconstruction 104

A.3 Results and discussion 106

A.3.8 Projection data 106

A.3.9 Slice reconstructions 107

A.3.10 3D image representation 109

A.4 Conclusions and future work 110

A.5 Acknowledgements 111

A.6 References 111

Appendix B 113

B Multispectral angular domain imaging with a tunable pulsed laser 113

B.1 INTRODUCTION 113

B.1.1 Trans-illumination optical imaging 113

B.1.2 Angular domain imaging 114

B.1.3 Multispectral angular domain imaging 115

B.2 Experimental setup and methods 116

B.2.1 Illumination and detection 116

B.2.2 Imaging target 117

B.2.3 Image pre-processing 117

B.3 Results and discussion 119

B.4 Conclusions and Future work 122

B.5 Acknowledgements 123

B.6 References 123

Curriculum Vitae 125

Table of Figures

Figure 1-1: Henyey-Greenstein scattering function with different anisotropy factors (g=0, 0.3, 0.6, 0.9, 0.95) 4

Figure 1-2: Possible photon paths through a scattering sample 6

Figure 1-3: Fourier-based ADI 11

Figure 1-4: Angular domain imaging with two aligned pinholes 12

Figure 2-1: Two-dimensional angular filter array made from 3D prototyping. (a) 3D rendering of the AFA construction process with alternating horizontal and vertical parallel walls. Rendering not to scale. (b) Top view photograph of the AFA. Blue outline: channel aperture, red outline: channel wall. White outline, defective channels due to imperfections in plastic deposition. Green outline, channels with rounded edges. 37

Figure 2-2: Schematic of the AFA-based ADI setup. Pulsed illumination at 780 nm from a laser (L) was spectrally filtered with a 780 ± 5 nm bandpass filter (SF), restricted with a 1 mm aperture (A) and collimated, expanded, and spatially filtered with collimating optics (C.O.). The collimated light passed through an illumination mask (I.M.), then through the sample (S) and the 2D AFA (AFA). The light was then detected with a CCD camera (C). 38

Figure 2-3: Raw AFA images of a 0.9 mm attenuating target in 0.5 % Intralipid® dilution at 1 cm path length collected with a 2D AFA 12 cm in length. (a) No illumination mask, (b) 3 cm illumination mask. Field of view was 8 mm x 8 mm..... 42

Figure 2-4: Transmission (a) and contrast (b) of a 0.9 mm attenuating target in 0.5 % Intralipid® dilution at 1 cm path length with a 12 cm 2D AFA and varying illumination mask length. Target was located at the 4th channel column. (a) blue:

no mask, dark green: 1 cm mask, red: 3 cm mask, teal: 6 cm mask, purple: 9 cm mask, olive green: 12 cm mask. 43

Figure 2-5: Transmission (a) and contrast (b) of a 0.9 mm attenuating target in 0.5 % Intralipid® dilution at 1 cm path length with a 3 cm illumination mask and varying 2D AFA lengths. (a) blue: no AFA, green: 1 cm AFA, red: 3 cm AFA, teal: 6 cm AFA, purple: 9 cm AFA, yellow: 12 cm AFA. 44

Figure 2-6: (a-c) AFA images of a 0.9 mm attenuating target in Intralipid® dilution at 1 cm path length collected with a 15 cm 2D AFA and 3 cm illumination mask after background subtraction. (a) 0.5% Intralipid®, (b) 0.6% Intralipid®, (c) 0.7% Intralipid® d) Transmission at varying Intralipid® concentrations at 1 cm path length, blue: 0.5% green: 0.6%, red: 0.7%. 46

Figure 3-1: Two-dimensional angular filter array fabricated with 3D printing. (a) Exploded 3D rendering of the 2D AFA fabrication details with alternating horizontal and vertical parallel walls. (b) Top view of the AFA. 61

Figure 3-2: Schematic of the ADI setup. Laser: 780 nm pulsed diode laser, Collimating Optics: Lens-pinhole spatial filter, beam expander and collimator, DLP: 608 x 684 pixel DLP chip (Texas Instruments), Beam Expander: 4x beam expander, Sample: Cuvette filled with a scattering medium, AFA: 2D Angular filter array, Camera: CCD Camera with telecentric lens 63

Figure 3-3: Images (a, c) and point spread functions (b, d) of a single illuminated channel in chicken (a, b) and Intralipid® (c, d). (a) Image of a point illumination through 10 mm chicken tissue. FOV = 8 mm x 8 mm (b) Normalized projections of a point illumination through 6 mm (blue), 8 mm (green), 10 mm (red). (c) Image of a point illumination through 0.65% Intralipid®. FOV = 8 mm x 8 mm (d) Normalized projections of a point illumination through 0.45% (blue), 0.55% (green), 0.65% (red), 0.75% (teal) Intralipid®. 70

Figure 3-4: Knife edge submerged in Intralipid® (a) 0.65% Intralipid® blue: quasi-ballistic subtraction profile of knife edge averaged from 0.5 mm x 15 mm central region in the image, red: fitted profile using dual logistic function. (b) Fitted edge spread functions for the knife edge submerged in 0.45% (blue), 0.55% (green), 0.65% (red), 0.75% (teal) Intralipid®. 71

Figure 3-5: 4 rods (0.2, 0.5, 0.7, 0.9 mm) submerged in (a) 0.6%, (b) 0.7%, (c) 0.75% Intralipid®. Images are quasi-ballistic images obtained by subtracting the background estimation image from the original image. (d) One-dimensional profiles obtained by averaging across 1 mm height, blue (0.6%), red (0.7%), black (0.75%). The field of view was 15 mm x 8 mm. 73

Figure 3-6: 4 rods ((a, c, e, g):0.2, 0.5,(b, d, f, h):0.9, 0.7 mm) positioned at the illumination side of a 1 cm cuvette containing a chicken breast slab. Images (a, b) are quasi-ballistic images obtained by raster scanning a structured illumination pattern. The column by column average (c:blue, d:blue) of (a, b) respectively, and the column by column average of the corresponding breast tissue with the rods removed (c:red, d:red). Trans-illuminated photographs of the imaging target collected from the illumination side (e, f) and from the detection (g, h) side of the target. The field of view was approximately 15 mm x 8 mm. 74

Figure 3-7: 0.5 mm rod positioned at the central depth position of a 1 cm cuvette containing a chicken breast slab. Image (a) is a quasi-ballistic image obtained by raster scanning a structured illumination pattern. (c) Column by column average of (a). Trans-illuminated photographs of the imaging target collected from the illumination side (b) and from the detection (d) side of the target. The field of view was approximately 15 mm x 8 mm. 75

Figure A-1 a) Cartoon of AFA: 80 μm x 80 μm x 2 cm, 200 elements. Channel count and dimensions are not to scale. b) SEM image (top removed) of a reflection-trapped AFA. 100

Figure A-2: Experimental Setup. Laser: Thorlabs 808 nm diode laser, ASL: Aspheric Lens, P: Pinhole, Collimating Optics: f = -6 mm, f = 100 mm cylindrical lens, Cuvette: 1 cm path length, AFA: element size 80 μm x 80 μm x 2 cm, 200 elements, Camera: Mightex TCE-1304-U. 101

Figure A-3: Imaging target, 4 truncated cones & cylinders. a) top view, b) side view, c) three dimensional rendering. All measurements are in millimeters..... 102

Figure A-4: a) Projection of a 0.5 mm graphite rod placed in the center of a 1 cm path length cuvette, submerged in 0.5% Intralipid®. Red: raw camera signal. Blue dashed: Signal re-binning. Blue: Defective channel removed by averaging signal from neighboring channels. FOV ~2 mm. b) Projection of graphite rod in (a) displayed in absorption units. FOV ~1 cm. c) Sample projection of imaging target, slice #25, ~1.2 mm from cone tips. Target diameter ~360 μm. 103

Figure A-5: Sinograms of the imaging target suspended in 0.5% Intralipid® dilution, 60 projections. Field of view is ~1 cm. a) Slice #25 ~1.2 mm from cone tips, target diameter: ~360 μm b) slice #125 ~9.2 mm from cone tips, target diameter: ~1.4 mm. 107

Figure A-6: 2D reconstructions of the 4 cone imaging target suspended in 0.5% Intralipid® dilution at 2 axial slices. a & b) Slice #25 ~1.2 mm from cone tips with filtered backprojection and iterative reconstruction methods, respectively. c & d) slice #125 ~9.2 mm from cone tips, reconstructed with filtered backprojection and iterative reconstruction methods, respectively. 108

Figure A-7: 3D reconstruction of the 4 cones imaging target using a) filtered backprojection and b) iterative reconstruction. The field of view for each slice is ~1 cm x 1 cm. 110

Figure B-1: a) Schematic of an AFA (channel count and dimensions not to scale). b) SEM image (top removed) of a reflection-trapped AFA. 115

Figure B-2: Experimental Setup. Laser: Continuum Surelite OPO, SF: Spectral Filter, Collimating Optics: f = 125 mm, f = 150 mm, Cuvette: 1 cm path length, AFA: element size 80 µm x 80 µm x 2 cm, 200 elements, Camera: Mightex TCE-1304-U. 117

Figure B-3: a) Projection of a 0.7 mm graphite rod placed in the center of a 1 cm path length cuvette, submerged in 0.25% Intralipid®; blue: raw camera signal; black: Signal re-binning; red: Signal with no absorbing target. FOV ~2mm. b) Projection of graphite rod in (a) displayed in absorption units. FOV ~1.5cm. 119

Figure B-4: a) Contrast of a 0.7 mm absorbing rod submerged in 4 levels of scattering at varying wavelengths. blue: 0.15%; green: 0.2%; red: 0.25%;teal: 0.3% Intralipid®. b-d) Computed absorption for 0.7 mm absorbing rod at Intralipid® dilutions of (b) 0.2%, (c) 0.25%, (d) 0.3%. blue: 480nm; green 520 nm; red 560 nm; teal 600 nm; purple: 640 nm; gold 680 nm. FOV ~1.5 cm..... 121

List of Appendices

A - Three dimensional angular domain optical projection tomography 98

B - Multispectral angular domain imaging with a tunable pulsed laser 113

List of Abbreviations and Symbols

1D, 2D, 3D	One, two, three dimensional
ABS	Acrylonitrile Butadiene Styrene
ADI	Angular domain imaging
AFA	Angular filter array
cm	Centimeter
CT	Computed tomography
CW	Continuous wave
DOT	Diffuse optical tomography
DRIE	Deep reactive ion etching
DTCC	3-diethylthiatricarbocyani
EMCCD	Electron multiplied charged coupled device
FDM	Fused deposition modelling
fs	Femtosecond
FWHM	Full width at half-maximum
g	Anisotropy factor
HG	Henyey-Greenstein
HDMI	High-definition multimedia interface
ICG	Indocyanine Green
LED	Light emitting diode

MEMS	Microelectromechanical systems
mm	Millimeter
MRI	Magnetic resonance imaging
NIR	Near infrared
nm	Nanometer
OCT	Optical coherence tomography
PET	Positron emission tomography
ps	Picosecond
PTS	Photon transport simulator
RTAFA	Reflection trapped angular filter array
s	Second
SCARA	Selective compliance assembly robot arm
SLR	Single-lens reflex
SLS	Selective laser sintering
SPECT	Single-photon emission computed tomography
SVD	Singular value decomposition
US	Ultrasonogrpahy
UV	Ultraviolet
μm	Micrometer
μM	Micromolar

Preface

This thesis summarizes the work completed through the duration of my MSc degree at the University of Western Ontario and Lawson Health Research Institute. This thesis consists of 4 chapters and 2 appendices. Chapter 1 discusses optical imaging the context of medical and biological imaging. The background of trans-illumination optical imaging is presented and the principles behind angular domain imaging and the angular filter array are described. The chapter concludes with a review of the various approaches, applications, and developments for angular domain imaging.

Chapters 2 and 3 are based on manuscripts in preparation for submission to peer-reviewed journals that were written over the course of my degree. The first publication focused on the design of the novel angular filter array and the optimization of the various design parameters to obtain images with the highest contrast for a particular imaging task. A method for structuring the illumination is presented. Chapter 3 describes a resolution analysis of the angular filter arrays presented in Chapter 2. Chapter 3 also introduces a scanning mechanism that can be implemented to improve the resolution of the images collected. Chapter 4 provides a summary and discussion of the project. Chapter 4 also discusses potential areas where the system can be improved.

Appendices A and B discusses advancements that were made to angular domain imaging. The experiments performed in Appendices A and B were conducted with the previous generation one-dimensional angular filter array. Appendix A discusses the acquisition of three-dimensional images by performing tomography. Appendix B demonstrates the collection of images at multiple wavelengths using a tunable light source. The various improvements can be applied to the two-dimensional angular filter array discussed in Chapters 2, 3, and 4. Both appendices were published as conference manuscripts.

Chapter 1

1 Introduction

This chapter includes a brief introduction of optical-based medical imaging. Angular domain imaging is an optical imaging modality which illuminates a sample with a light source, and detects the light exiting the sample with an optical angular filter. In order to understand angular domain imaging, optical scatter in biological tissue will be described in detail. The two main approaches to angular domain imaging will then be described in detail. Various other approaches to optical imaging through scattering media will be discussed as well.

Angular domain imaging has been studied extensively in the past. Several prototypes of angular filters have designed and improved upon. Angular domain imaging has also been combined with other scatter discrimination techniques such as polarization and time domain imaging. It has been extended to collect three-dimensional images via tomography. Additionally, multi-spectral and hyper-spectral light sources have been employed to image spectral targets, and to detect fluorescence through scatter. A brief summary of previous angular domain imaging studies will be presented.

The objective of this work was to develop a two-dimensional angular filter array to acquire two-dimensional angular domain images with minimal scanning. Previous angular domain imaging systems utilized a one-dimensional angular filter, which was inefficient at acquiring two-dimensional or three-dimensional images. By extending the angular filter to two-dimensions, two-dimensional images can be acquired significantly faster, and with minimal scanning. The development of the two-dimensional angular filter represented a significant hurdle as conventional fabrication technologies used to construct the one-dimensional angular filter could not easily construct two-dimensional objects. This chapter will discuss the various hurdles associated with the construction of the two-dimensional angular filter, and it will also discuss the novel fabrication methods used to construct the two-dimensional filters. After the two-dimensional angular filters were successfully constructed,

their imaging performance was quantified by evaluating the contrast (Chapter 2) and resolution (Chapter 3) of known absorbing objects embedded in various scattering samples. This chapter includes background relevant to the understanding of technical details introduced in Chapters 2 and 3.

1.1 Medical Imaging

The growing need for improving medical diagnoses has necessitated the development of various medical imaging modalities. Current medical imaging technologies include magnetic resonance imaging (MRI), x-ray computed tomography (CT), ultrasonography (US), single photon emission computed tomography (SPECT), and positron emission tomography (PET). The numerous medical imaging technologies have differing strengths and capabilities. The various imaging resolutions, contrast mechanisms, sensitivities and specificities are all factors which are accounted for when selecting an imaging modality for a specific task.

Generally, MRI provides strong contrast between varying soft tissues. It is capable of imaging at a large range of depths and resolutions including whole body imaging and small animal imaging. However, it is often associated with a high cost due to the expensive equipment, and relatively long acquisition times. CT is capable of generating high contrast images between bone and soft tissues but it is often incapable of detecting soft tissue abnormalities. SPECT and PET are capable of functional imaging by imaging radio-labeled molecules which have been introduced to a subject. However, the resulting images often lack anatomical detail, and often rely on a second imaging modality to serve as an anatomical reference. CT, SPECT and PET all utilize ionizing radiation, which can potentially be harmful if used excessively. Ultrasonography is capable of detecting various tissue densities in real time. Many tissue abnormalities are often not associated with different tissue densities, and consequently have poor contrast when imaging with ultrasound.

1.2 Optical Imaging

Optical imaging is an emerging medical imaging modality which is currently being explored as it utilizes a different contrast mechanism from the other commonly used medical imaging modalities. Optical absorption and scatter provide sources of contrast which cannot be detected with other imaging modalities. Multispectral imaging can help identify tissue structures and abnormalities, and potentially measure oxygen saturation or molecular concentrations. While scatter can often serve as a source of contrast for many optical imaging modalities, it is a limitation for most optical imaging techniques. Optical scatter often limits optical imaging to relatively small penetration depths (microns to centimeters). In general, for purely optical imaging modalities, penetration depth can be increased at the expense of resolution. For example, ballistic optical imaging can image thin objects at high resolutions, while diffuse optical tomography can image through thick specimens, but at a reduced resolution [1,2].

1.3 Light Tissue Interactions

Light travelling through a scattering medium such as a biological tissue sample, can either pass through unperturbed, or interact with the sample through absorption or scattering processes. An absorption process is described as the extraction of energy from light by a molecular species (Figure 1.2, absorption). A scattering process can be described as a change in the direction of light. Light scattering can be caused by a multitude of processes. For example, a mismatch in the index of refraction between sub-cellular organelles and the surrounding cytoplasm can be a source of optical scatter [3].

It is important to note that when light scatters in tissue, the scattering is anisotropic. Scattering events in tissue tend to be forward directed. The scattering phase function for tissue is typically modeled after the Henyey-Greenstein function (Eq. 1-1) [4]. The function models the angular scattering distribution with the use of the average of the cosine of the scattering angle, g.

$$P_{HG}(\theta) = \frac{1}{4\pi} \frac{1-g^2}{(1+g^2-2g\cos(\theta))^{3/2}} \text{ where } g = 2\pi \int_0^{\pi} \cos(\theta) P_{HG}(\theta) \sin(\theta) d\theta \qquad \text{Eq. 1-1}$$

In the Henyey-Greenstein function, g ranges from [-1,1] and describes the possible scattering directions from perfect backscattering (g = -1) to isotropic scattering (g = 0) to complete forward scattering (g = 1). Typical values of anisotropy range from 0.6 to 0.99 for biological tissues, and are wavelength dependent [5]. The phase functions of varying scattering values (g) are displayed in Figure 1-1.

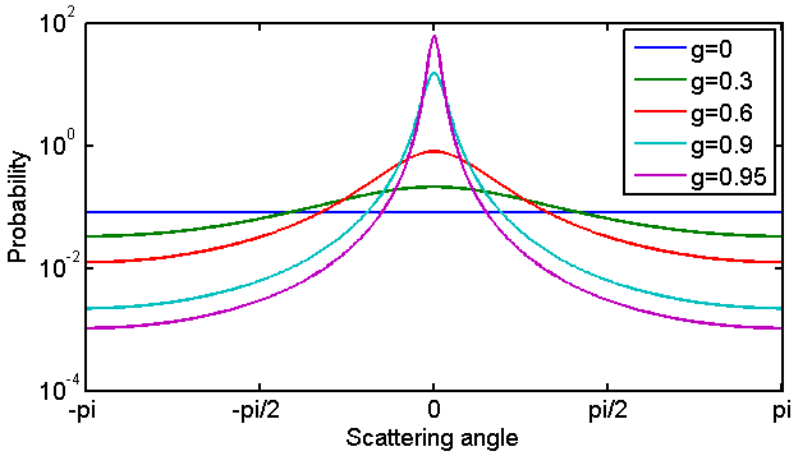

Figure 1-1: Henyey-Greenstein scattering function with different anisotropy factors (g=0, 0.3, 0.6, 0.9, 0.95)

While optical imaging can refer to any imaging at wavelengths from ultraviolet to near infrared, several optical imaging techniques tend to restrict the imaging wavelength to the tissue optical window, a small range in the near infrared spectrum from 700 to 1100 nm. Within this wavelength band, intrinsic optical absorbers are at a minimum. Below 700 nm, hemoglobin is highly absorbing, and beyond 1100 nm, light is absorbed by water. The lack of intrinsic absorbers in this diagnostic window allows light to penetrate further in the imaging sample.

When a photon of light passes through a scattering sample, there is a possibility that the photon will not interact with the scattering sample, and pass through the sample unperturbed (Figure 1-2, ballistic). Unscattered photons, also called ballistic photons, are of particular interest in optical trans-illumination imaging as ballistic photons can be used to generate high resolution images. The probability a photon passing through a sample unscattered is dependent on the scattering nature of the sample, and the thickness of the sample. Generally, the number of ballistic photons decreases exponentially with thickness. When imaging through thin tissue samples, (1-2 mm), it becomes difficult to detect ballistic photons. For tissue samples thicker than 2 mm, virtually no ballistic photons remain [6].

Light scatters through tissue in a forward directed nature. Consequently, when a sample is illuminated, a small subset of the photons exiting the sample will have undergone a series of small angle scattering events. These photons are termed quasi-ballistic or snake photons (Figure 1-2, quasi-ballistic). This subset of photons can potentially be used to generate higher resolution images compared to purely scattered photons. Theoretically, these quasi-ballistic photons are able to travel farther through a scattering sample compared to ballistic photons due to the relaxed nature of their classification. Consequently, when imaging a relatively thick tissue sample, (2 mm - 2 cm) quasi-ballistic imaging of a sample is possible, whereas a purely ballistic imaging system will be either unable to generate an image, or will require a significantly long acquisition time to acquire an image. For many imaging applications, the tradeoff between resolution and imaging depth or acquisition speed is often desirable, resulting in considerable interest to develop a quasi-ballistic optical imaging system.

When a photon scatters within the scattering sample, the path that it travels through the sample is generally not recoverable. A typical detector will be able to detect the position at which the photon exits the sample, and a sophisticated detector may even be able to measure the time the photon travelled within the sample. Multiply scattered light imaging such as Diffuse Optical Tomography (DOT) utilizes this information to create general inferences on the probable path of the photon using probability theories and simulated experiments. These inferences allow for the imaging of thicker tissue samples (1-10 cm)

using multiply scattered light (Figure 1-2, scattered). However, the uncertainty in the images greatly reduces the potential resolution of an image generated with scattered light.

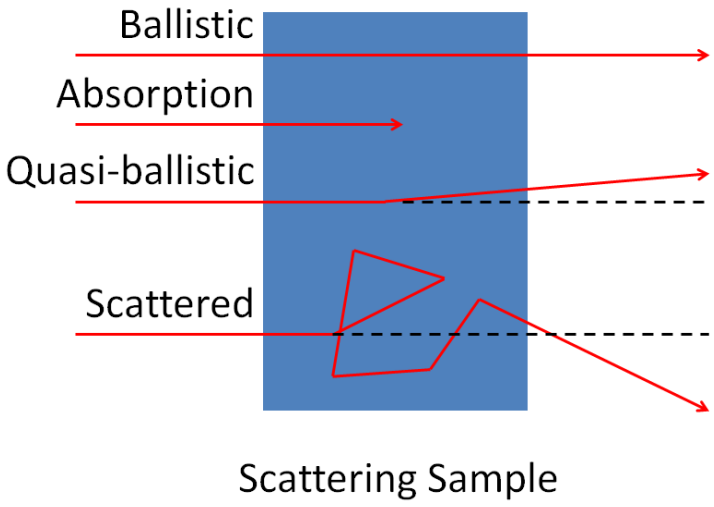

Figure 1-2: Possible photon paths through a scattering sample

1.4 Overview of Optical Imaging Modalities

Optical imaging techniques can be classified into two groups: purely optical imaging modalities and hybrid optical imaging modalities. A purely optical imaging modality probes and detects with light, whereas a hybrid optical imaging modality combines optical imaging with another method for probing or detecting.

1.4.1 Optical Coherence Tomography

Optical Coherence Tomography (OCT) is currently one of the most advanced optical imaging modalities. It is commercially available, and it has already been applied extensively for ophthalmic imaging to obtain images of the retina [7]. OCT relies on optical interferometry to obtain high resolution superficial images of a target. A low coherence beam of light is split into a reference beam and a sample beam. The reference beam passes through an optical path with an adjustable path length, while the sample beam is used to illuminate the sample. The light reflecting form the sample is then recombined with the reference beam

and the resulting interference pattern is analyzed. Constructive interference occurs when the path length of the sample arm is similar to the path length of the reference arm (within the coherence length of the illumination source). The sample arm is scanned in two axes and the reference path length is scanned in one axis to generate a three-dimensional image of the target. Alternatively, a full field illumination scheme can be employed to collect three-dimensional images by scanning only the reference arm [8]. The short coherence length serves as a scatter rejection mechanism as only photons that have travelled a similar path length as the reference arm are imaged. Multiply scattered photons typically travel longer distances before reaching the detector compared to a non-scattered photon. Due to the efficiency of the scatter rejection, OCT produces high resolution images (~10 μm typical or 1-2 μm for ultrahigh-resolution OCT) [7,9]. However, it is limited to superficial depths (2-3 mm) due to the lack of ballistic photons at larger depths.

1.4.2 Time domain imaging

Like OCT, time domain imaging discriminates between scattered photons and unscattered photons by the path length of the photon [10-12]. In time domain imaging, the path length is measured by the time of flight of a particular photon. Given that the speed of light is relatively constant through an imaging sample, the time of flight can be used to deduce the path length of the photon. In time domain imaging, an ultrafast light source (fs) is combined with an ultrafast detector (fs or ps resolution) to capture images of photons which have travelled within a given range of path lengths. The detector is controlled by a delay generator which can vary the time delay of the detector, and correspondingly vary the path length of the detected photons. When a time gate corresponding to the theoretical time of flight of an unscattered photon is employed, a near ballistic image will be generated. When the time gate is relaxed to an extent, a quasi-ballistic image can be obtained. Finally, with a long time gate, a scatter image can be obtained. A typical time domain ballistic imaging system is capable of imaging through a thin sample (< 1 mm tissue) with a diffraction-limited resolution, or through a slightly thicker sample (3.5 mm tissue) in the quasi-ballistic or snake regime with a resolution of ~200 μm [13]. Using this method, the bone within a human finger can be visualized [12]. One of the main disadvantages of time domain imaging is the expense

of the equipment required for a typical system. Femtosecond light sources and picosecond cameras are 10-100 times the cost of a comparable continuous wave (CW) light source and detector. An optical Kerr cell detection scheme significantly reduces the cost of the detector, but still requires an ultrafast illumination source.

1.4.3 Diffuse optical tomography

Diffuse optical tomography probes a sample with a series of sources and detectors [2]. Based on the geometry and scattering properties of the sample, the potential paths of a large population of photons can be modeled using various photon propagation theories or simulated via Monte Carlo simulations. A typical DOT system operates in the multiply scattered regime, where photons undergo several large angle scattering events before reaching the detector. In this regime, thick tissue samples can be imaged (3 cm – 10 cm). Due to the use of multiply scattered photons, the resolution of a typical DOT system (~1 cm) is much larger than an optical ballistic or quasi-ballistic system.

1.4.4 Hybrid optical ultrasound imaging

In addition to purely optical imaging modalities, several hybrid optical imaging technologies have been developed. Photoacoustic and acousto-optic imaging both combine ultrasonic imaging with optical imaging [14]. In photoacoustic imaging, a high powered short pulse of light is used to illuminate a sample. An optically absorbing object embedded within the sample will then absorb the pulse of light and convert the optical energy to heat. The rapid heating form the short light pulse will cause a thermoelastic expansion of the target resulting in the emission of a pressure wave. The pressure wave can then be detected with an ultrasonic detector, and the position of the target can be triangulated via various reconstruction algorithms.

Acousto-optic imaging utilizes a continuous wave laser as an illumination source. The illumination passing through the scattering sample will form a speckle pattern. The sample is then probed with a focused ultrasound transducer which ultrasonically tags a small region in the imaging volume. The ultrasound waves modulate the local refractive index, and displace

the scatterers within the sample, resulting in a modulation of the speckle pattern at the ultrasound frequency. By analyzing the modulation, the system is able to measure the optical properties of a small region within the sample [15]. A purely optical imaging system is unable accomplish this precise sampling of an imaging volume. In both photoacoustic and acousto-optic imaging systems, the high resolution of ultrasound is combined with the high contrast of optical imaging.

1.5 Angular Domain Imaging (ADI)

Angular domain imaging is a continuous wave method of quasi-ballistic imaging. Unlike time domain imaging, it does not require expensive instrumentation, and is relatively simple to implement. In angular domain imaging, the different types of photons, ballistic, quasi-ballistic, and scattered are differentiated by the angle at which the photon deviates from the initial illumination beam. Ballistic photons are unscattered by the imaging sample, and can therefore be found exiting the sample at the same angle at which it entered the sample. Quasi-ballistic photons undergo a few forward directed scattering events, and can be found at small angles with respect to the illumination direction. Finally scattered photons have undergone multiple large angle scattering events and can be found at large angles with respect to the illumination direction.

One common design flaw is apparent in angular domain imaging. Quasi-ballistic photons can be found near the axis of illumination. However photons exiting the sample near the axis of illumination are not necessarily quasi-ballistic photons. Assuming that the imaging sample is sufficiently scattering, scattered photons can be found at a wide range of angles with respect to the axis of illumination. Consequently, a small portion of the scattered photons will exit the sample at or near the same angle at which they entered the imaging sample. One major weakness of an angular domain imaging system is the inability to distinguish between quasi-ballistic photons, and multiply scattered photons which have scattered back to the axis of illumination.

Angular domain imaging can be performed using one of two methods. The first method involves the use of a Fourier domain angular filter. The second method involves the

use of a lensless collimator. There are subtle differences between the two methods. Regardless of the method, the effectiveness of the angular filtration is dependent on the precise positioning of the angular filter in ADI.

1.5.1 Fourier-based ADI

A Fourier-based ADI setup utilizes a converging lens and an aperture to perform angular filtration [11,16-20]. The aperture is positioned on the back focal plane of the converging lens. The light emitting from the aperture is then projected onto an imaging detector. The inclusion of a convex lens allows for the measurement of the Fourier image at the focal plane of the lens. An aperture positioned at the focal plane acts as a Fourier filter. The light emitting from the aperture is then transformed back to a real image which is then imaged with a detector. In the Fourier domain, the spatial frequency of large biological inclusions is much lower than the spatial frequency of the small random scatterers in a scattering medium. Consequently, the large biological inclusions will be represented near the center of the Fourier plane, while the high frequency scatter component will be located far from the center of the Fourier plane. By selecting an appropriate aperture size, the large biological inclusions can potentially be distinguished from the scatter photons. Alternatively, from the perspective of ADI, parallel rays of light will be focused by the converging lens to the focal point. Non-parallel light will focus elsewhere on the focal plane. A well-positioned aperture at the focal plane will reject photons that are not parallel with the optical axis (Figure 1-3). Using ray tracing simulations, the effective acceptance angle of a lens pinhole system can be computed.

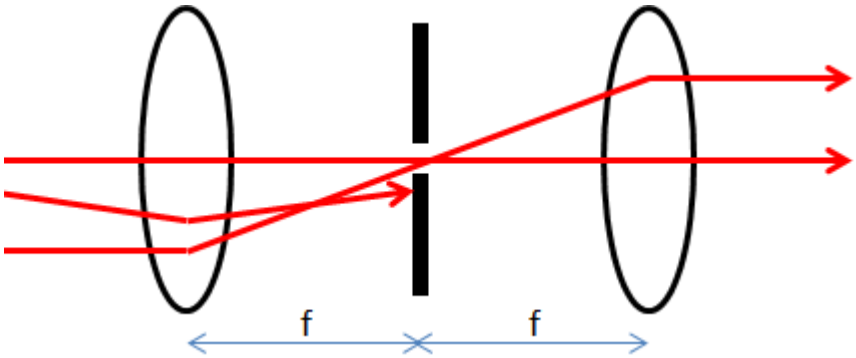

Figure 1-3: Fourier-based ADI

One interesting limitation of the lens aperture method to ADI is the scatter rejection of a pinhole is linked directly with the Fourier frequency. By using a smaller pinhole, the system will conceivably reject more high frequency scattered light. However, the rejection of high frequency scattered light also imposes a restriction on the potential resolution of the image as the high frequency Fourier component may be required to form a faithful image. A second limitation of the lens aperture method is the use of a lens in the filtration step. A lens is commonly associated with various aberrations (e.g. spherical, chromatic), and as a result cause deviations between the theoretical and experimental performance. In addition, chromatic aberrations may limit the ability to image at multiple wavelengths of light, potentially preventing multi-spectral or hyper-spectral imaging.

1.5.2 Lensless ADI

A lensless collimator can refer to a variety of designs. The simplest collimator consists of a pair of aligned pinholes separated by a distance (Figure 1-4). The first pinhole serves to restrict the light entering the collimator to a small aperture, while the second pinhole passes only light which has travelled in the axis of the collimator. The acceptance angle of this collimator is dependent on the size of the pinhole as well as the spacing between the pinholes. A larger pinhole and a shorter spacing will result in a larger acceptance angle, while a smaller pinhole and a larger spacing will result in a smaller acceptance angle. This simple design only allows for the imaging of a single point. Consequently, a two-dimensional image requires scanning to compile.

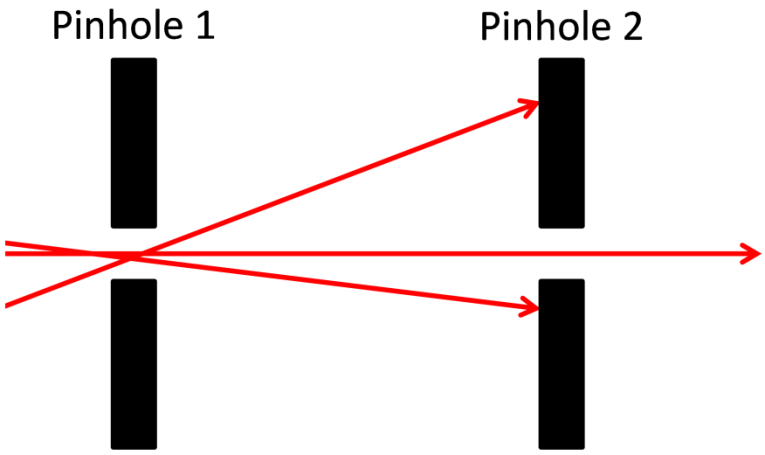

Figure 1-4: Angular domain imaging with two aligned pinholes

In order to parallelize the acquisition process, a series of pinholes can be used instead of a single pinhole. To prevent crosstalk between the pinholes, a lattice structure must be placed between the two arrays of pinholes. This design is the basis of a Söller collimator in x-ray imaging, or an Angular Filter Array (AFA) in optical imaging [21]. Much like the pair of pinholes, the acceptance angle of the AFA is based on the aspect ratio of the optical channel.

1.5.3 ADI simulations

Angular domain imaging using a lensless angular filter has been extensively studied by two research groups: the Chapman group at Simon Fraser University and our group, the Carson group, at the Lawson Health Research Institute. Previously, Monte Carlo simulations were conducted by the Chapman group to study the theoretical performance of an angle-based scatter rejection imaging method [22,23]. Monte Carlo simulations are considered the gold standard for simulating photon transport through a scattering medium as it is capable of simulating arbitrary complex geometries. The major drawback to the Monte Carlo method is the significant computational resources required to generate a statistically acceptable result. Previous simulations were conducted on a custom software package, Photon Transport Simulator (PTS), which was designed to model the effects of the various angular filters. In PTS, the photon transport modeling through a scattering medium was based on a previous Monte Carlo simulator described by Jacques and Wang [24].

Extensive simulations were conducted to test the theoretical performance of an ADI system. The first simulation tested the fundamental basis of ADI, and the principle of angular selection as a quasi-ballistic photon discriminator. A typical quasi-ballistic photon will exhibit a shorter path length through a scattering sample compared to a multiply scattered photon. A Monte Carlo simulation was performed to examine whether smaller angular deviations at the exit face of a sample corresponded to photons with shorter path lengths. The results indicated that for intermediate scattering levels, a smaller acceptance angle corresponded to a smaller mean photon path length. At higher scattering levels, this effect was not observed, suggesting that there is a fundamental limit of ADI and ADI systems are expected to fail when the scattering of the sample is beyond a particular limit [22]. The simulation conclusions were consistent with the results of a separate study which demonstrated that photons exiting the sample at smaller angles are related to the early arriving photons in a time domain system. In this study, the temporal point spread function was observed to decrease when a smaller acceptance angle was utilized. Measurements were conducted with various combinations of Intralipid® concentration and optical cell thicknesses, with the product of the concentration and the length held constant at the equivalent of 2% Intralipid® and 10 mm cell thickness [11]. Intralipid® is a lipid emulsion that serves as a convenient phantom to simulate optical scatter in biological tissue [25]. In a separate study, projection images of a target embedded in a scattering medium were collected with a collimated light beam. Image contrast was found to be greatly improved with the addition of a Fourier angular gate after the scattering medium [10]. Another study reported the imaging of 0.25 mm black bars submerged in a 5.5 cm thick optical cell filled with 2.5% Intralipid® with the use of a Fourier gate [16].

A second simulation was conducted by the Chapman group to test the theoretical resolution of a micro-channel array [22]. One concern of the micro-channel array was the potential relation between channel size and the resolution of the imaging system. A Monte Carlo simulation was conducted where an object smaller than the size of the channel was imaged through a scattering medium. The results indicated that the object was clearly resolvable for lower scattering levels. Higher scattering levels were unable to be tested with the simulation method as the simulations became computationally unfeasible. The results

indicate that the resolution of an AFA image is dependent on the resolution of the detector (camera) and not dependent on the size of the channels.

A third simulation conducted by the Chapman group tested the theoretical acceptance angle for an individual AFA channel. When a photon of light strikes the wall of the AFA, it can either be absorbed by the AFA or reflected. The probability of reflection increases as the angle of incidence with the wall increases (i.e. a photon that strikes the wall at a glancing angle has a higher probability of reflecting compared to a normally incident photon). Internal reflections increase the effective acceptance angle of an AFA compared to the theoretical acceptance angle of that AFA. The theoretical acceptance angle can be computed geometrically (Eq. 1-2) and is representative of the acceptance angle of the AFA under the assumption that all photons striking the walls of the channels attenuate. For a typical angular filter with an aspect ratio (collimator length / collimator diameter) of 200, the theoretical acceptance angle is 0.28°. Due to internal reflections, simulation studies show that the acceptance angle for a silicon-based AFA with an aspect ratio of 200 is approximately 2.3º [23].

$$\theta = \tan^{-1}\left(\frac{\text{collimator diameter}}{\text{collimator length}}\right) \qquad \text{Eq. 1-2}$$

A fourth simulation was conducted by the Chapman group to test the effect of aperture size on acceptance angle. For a micro-channel based collimator, the size of the aperture can potentially be changed without changing the acceptance angle by increasing the length of the channel correspondingly. A simulation was conducted where the aspect ratio of the channel was held constant at 200, while the diameter of the channel was varied from 10 µm to 100 µm. The simulation results demonstrated that the acceptance angle of the micro-channel array was constant for the various channel diameters, suggesting that the acceptance angle was indeed dependent on the aspect ratio of the channels and was not dependent on the size of the channel itself. The results also indicated that for smaller channels (< 100 µm diameter), the overall efficiency of the channel was decreased. This effect was attributed to diffraction effects from smaller sized channels. The results suggest that to optimize AFA throughput, the channel size should be above 100 µm [23].

1.6 Previous AFA design

Several collimator designs that fit the AFA description have been described previously in the literature [21]. However, the specifications and fabrication methods are often omitted in these studies. One silicon-based AFA design has been replicated in multiple studies by the Chapman and Carson groups [19,22,23,26-43]. The silicon-based AFA design utilizes MEMS-based fabrication techniques to create a series of channels in a silicon wafer. The first design was constructed using a chemical isotropic etchant. The second design replaced the chemical isotropic etchant with a Deep Reactive Ion Etching (DRIE) machine for added control during the etching process.

1.6.1 Silicon AFA fabrication process

The silicon-based AFAs were constructed by first allowing the growth of a layer of silicon dioxide (SiO_2) on a silicon wafer to act as a masking layer. A photoresist was then spin coated on the wafer and exposed with a UV lithography process to transfer a mask pattern onto the photoresist. The developed photoresist was used as a mask to etch the underlying SiO_2 layer. The patterned SiO_2 layer was then used as a mask for etching the silicon wafer via a chemical isotropic etchant or a DRIE machine. Finally, the SiO_2 layer was removed, leaving a series of micro-channels embedded in a silicon wafer. The wafer was then diced to expose the entrance and exit faces of the micro-channels. A second silicon wafer was then positioned on top of the micro-channels to enclose the top surface of the channels.

1.6.2 Chemically etched AFAs

The chemically etched AFAs resulted in a series of micro-channels with a semi-circular cross section due to the isotropic nature of the etchant. In this design, the semi-circular channels each had a radius of 25 μm and a length of 1 cm. Neighboring channels were spaced periodically at 100 μm. The acceptance angle of the channels can be computed geometrically under the assumption that no internal reflections occur. For this design, the angular acceptance was quoted as 0.29° [33]. One of the main drawbacks of the isotropic wet

chemical etching process was the poor reproducibility of the fabrication. The etch rate was sensitive to the agitation of the sample container. In addition, the resulting semicircular channel cross section suffered from a low fill factor due to the changing wall thicknesses between channels [34].

1.6.3 Deep Reactive Ion Etching AFAs

One method of improving the fill factor was changing the fabrication process to etch micro-channels with a square cross section. DRIE allows for anisotropic etching of the silicon wafer. In addition, the DRIE method was highly reproducible and resulted in channels with excellent uniformity across the entire area of the silicon wafer. By utilizing the DRIE method, the sizes of the micro-channels were highly customizable. AFAs with a wide range of channel sizes (20 μm x 20 μm to 80 μm x 80 μm) and channel lengths (0.5 cm to 2.0 cm) were constructed and a series of experiments were conducted by the Carson group to evaluate the contrast of each AFA [43]. The DRIE method was determined to be superior to the previous isotropic etching method for reproducibility and AFA design.

1.6.4 Internal reflections

In addition to highly reproducible fabrication, the DRIE method allowed for another improvement over the chemical etching method. One concern of the AFA collimator was the potential for photons to strike the walls of the channels at glancing angles, and reflect. An internal reflection will increase the effective acceptance angle of the channel, and result in an angular filter with poorer contrast and resolution performance. In previous studies by the Chapman group and the Carson group, two main approaches were used to attempt to minimize the internal reflections within the AFA.

The first approach was to deposit a thin layer of optically absorbing material on the surface of the micro-channels to improve the absorption of the photons that strike the walls of the AFA. A carbon arc evaporator system was first used to deposit a thin layer (30 - 40 nm) on the surface of the AFA. Preliminary studies were conducted where successive images of the AFA were collected after introducing pitch and yaw rotations to the AFA. The AFA

rotations allowed for the measurement of the internal reflections. The rotation studies indicated that the internal reflections were subdued to an extent when a carbon layer was deposited on the AFA however this result was never quantified by the author of the study [27]. One drawback of the evaporation method was the high level of debris generated, leading to the partial or full occlusion of several AFA tunnels. This deposition method was later improved by the Carson group with the use of a carbon sputter deposition process instead of an evaporation deposition process [42]. The sputter deposition method provided higher uniformity and excellent adhesion.

The second approach to minimize internal reflections was to reduce the angle of incidence of photons striking the walls of the AFA. This was accomplished by altering the smooth surface of the AFA walls. In the first design, the surface of the AFA was roughened by including an additional etching step to the fabrication process. The AFA was wet etched using a NH_4OH solution [27]. Preliminary experiments suggested that the roughened walls decreased the internal reflections within the channels, but this effect was not quantified. One weakness of the etching process was the uneven etching across the entire AFA. This problem was addressed in the second design of the wall roughening process. In the second design by the Carson group, a periodic wall pattern was incorporated into the lithography mask [40,42]. Ridges 2.5 μm tall were positioned at 20 μm intervals along the length of the AFA channels. The new AFA design was termed the Reflection Trapped AFA or (RTAFA). The ridges were designed to reduce the angle of incidence of any photon striking the walls of the channel to promote the absorption of the scattered light. The ridges also contained the scattered photons within the AFA to an extent. The new RTAFA design was demonstrated to improve the contrast of a resolution target suspended in a scattering medium compared to a conventional AFA design. For example, a 50% increase in image contrast was observed when utilizing a 60 μm x 60 μm x 1.5 cm RTAFA over a conventional AFA when imaging through a 0.3% Intralipid® dilution at a 2 cm optical path length [40]. Due to the nature of the fabrication process, the RTAFA only exhibited patterned vertical walls. The patterning of the top and bottom surfaces of the square channels would require additional lithography masks, and would greatly increase the complexity of the fabrication.

1.7 ADI Illumination sources

AFA-based ADI has been demonstrated with various illumination sources. For trans-illumination imaging, three main qualities are considered. The first is the imaging wavelength. Several biological targets are detectable at specific wavelengths. Much of the preliminary work in ADI has been conducted with tissue mimicking phantoms and wavelength independent targets. Consequently much of the early work in ADI was conducted at a multitude of arbitrary wavelengths. One particular study of interest by the Chapman group evaluated the performance of the ADI system at three wavelengths in the visible and near infrared spectrum [37]. Several attempts have also been made to combine ADI with a hyper-spectral light source. A study was conducted by the Carson group, with a Quartz Tungsten Halogen lamp, which emits light over a continuous range of wavelengths simultaneously [39]. An additional study published by the author was conducted with a wavelength tunable light source (Appendix B) [29].

In trans-illumination imaging, the collimation of the illumination source generally improves the quality of the resulting images [20,44]. Typically laser light sources can be highly collimated, and are suitable for ADI. A lamp typically generates light from a large filament, resulting in a source that is difficult to collimate efficiently.

In trans-illumination imaging, the geometry of the illumination source is also an important factor to consider. Generally, extended light sources perform poorer when compared to a scanning point light source. This is due to the potential for light to scatter into a neighboring area. A raster scanning point illumination system will be able to account for optical smearing due to scatter, while a full field image collects all the data simultaneously, and is therefore unable to intrinsically remove the excess scatter. In a previous study performed by the Chapman group, when a sample was illuminated with a line of light, image quality was improved compared to a full field illumination [26].

1.8 Previous ADI studies

1.8.1 Hybrid ADI systems

ADI has been studied extensively over the past decade. Several attempts have been made to combine ADI with a complimentary scatter rejection method to improve the performance of ADI at higher scattering levels. The Carson group examined the depolarization of light as a method to distinguish between ballistic and multiply scattered photons [38]. In addition to polarization gating, the Carson group utilized time gating in conjunction with ADI. An ultrafast pulsed laser (270 ps) was combined with a picosecond gated camera to provide time gating alongside the angular gating from ADI. Contrast was demonstrated to improve for a given scattering level, however the system was unable to image at scattering levels beyond the limit for ADI-only systems [40].

1.8.2 Background scatter estimation

When imaging near the scattering limit with ADI, it is possible to improve the contrast of images by estimating the background scatter signal. A typical ADI image contains signal from two components, a quasi-ballistic component and a background scatter component. The quasi-ballistic component is the information containing component, and the source of contrast in the image. The background scatter is present due to the imperfect nature of angular filtration based imaging at high scattering levels. At high scattering levels, multiply scattered photons can potentially scatter back into the axis of illumination and contribute to a background signal in the image. The background signal in an image reduces image contrast. One method of improving the image contrast is to estimate the background signal through various methods, and then subtract the background signal from the original image to obtain a better approximation of a quasi-ballistic image. In the combined angular and polarization gating experiment mentioned previously, the background scatter was estimated by obtaining an image with the analyzer and the polarizer positioned in the crossed position. The crossed polarization image was not expected to contain any quasi-ballistic signal, and served as a method of measuring the scattering component of the image. In the

hybrid time-angular domain imaging system mentioned previously, a scatter estimation image was obtained by imaging the sample at a late gate delay where no quasi-ballistic photons were expected to be detected [31]. In ADI systems described by the Carson group, the scattered component was measured by introducing an optical wedge into the illumination path. An optical wedge was expected to deviate the illumination by an angle larger than the acceptance angle of the AFA. As a result, when an image was collected with a scattering sample, the image was expected to contain only the scattering component [38]. The principle of scatter estimation has been applied to various other trans-illumination imaging systems including the use of a differentiometer to measure the difference between on axis and off axis light [45] and the use of a diffuser in the illumination path to destroy the collimation of the light, and obtain a scatter only image [46,47].

1.8.3 Deep illumination ADI

While some ADI studies have been focused on improving the imaging performance of ADI, other studies have been focused around finding potential applications for ADI. One example involves a significant change in the imaging setup from a trans-illumination imaging system to a reflection-based imaging system [36,48]. One of the main drawbacks of trans-illumination ADI is the limitation of sample thickness. ADI has only been successful at imaging samples with a small optical thickness (6 reduced mean free paths) [40]. This corresponds to a tissue thickness of approximately 6 mm, and significantly limits the application of ADI in a clinical setting. By switching the setup to collect reflected images, the ADI system will be able to capture images of samples up to 3 mm below the surface of a sample. This may potentially find applications in dermatology or endoscopy. Light scattering in tissue has been described to be forward directed. However, there is a small portion of light that undergoes backscattering. The backscattering was used as an illumination source for deep illumination ADI. Using this ADI setup, two-dimensional absorbing targets were observed when positioned 3 mm from the surface of a tissue mimicking phantom [36].

1.8.4 Tomographic ADI

Optical trans-illumination imaging is similar in principle to x-ray planar imaging. X-ray planar imaging has been successfully extended to collect three-dimensional images via computed tomography. Optical tomography has already been previously demonstrated with time domain imaging [49]. As a result, a natural extension of ADI was to collect tomographic images of a sample and to reconstruct the images to obtain three-dimensional images of a sample. In an initial study conducted by the Carson group, two attenuating rods of 0.9 mm diameter were submerged in a 2 cm optical cuvette filled with a 0.3% Intralipid® dilution. The two rods were imaged at 200 projections and successfully reconstructed. The author conducted a follow-up study where a series of four cylindrical rods ranging from 0.2 mm to 0.9 mm diameter suspended in a 0.6% Intralipid® dilution at 1 cm path length were imaged and successfully reconstructed with 60 projections. Two hex keys 1.2 mm wide and 2 mm wide were also reconstructed when placed in the same scattering solution. Finally a 2 cm diameter grape was imaged, and the seeds of the grape were successfully reconstructed [30]. The author conducted another study which involved the collection of three-dimensional angular domain images via rotation and scanning. A custom resolution target with four truncated cones varying in diameter from 1.2 mm to 0.2 mm was constructed and positioned in a scattering sample. The structure was successfully reconstructed in three dimensions [32].

1.8.5 Fluorescence ADI

While conventional ADI utilizes absorbing targets within a scattering medium as sources of contrast, a fluorescent target can be used as an optical source within the scattering sample itself. In one study conducted by the Carson group, two 1.2 mm diameter tubes filled with 3-diethylthiatricarbocyanin (DTTC, 20 μM) were positioned at a depth of 1 mm in a cuvette filled with 1% Intralipid® dilution. The tubes were successfully resolved when using an AFA. The tail of a hairless SKH1 mouse (6 weeks old) was also imaged after the injection of an optical bone marker (IRDye® 800CW BoneTag). The vertebrae of the mouse were resolved [35]. A second study conducted by the Carson group demonstrated the possibility of tomographic fluorescent imaging by imaging a 1.2 mm glass tube filled with 20 μM

Indocyanine Green (ICG) submerged in a 2 cm cuvette filled with a 0.1% Intralipid® dilution [41]. A third study by the Carson group demonstrated the possibility of performing fluorescence lifetime measurements of a fluorescent target submerged in a scattering medium. A pair of 1 mm diameter glass rods were filled with ICG (20 μM) and positioned in the center of a 1 cm path length cuvette holding a 0.1% Intralipid® dilution. The temporal point spread function was then measured across the length of the AFA, and the pixel locations corresponding to the ICG locations were observed to have a different temporal point spread function compared to the pixel locations with no ICG [28].

1.8.6 Multispectral and Hyperspectral ADI

One of the main advantages of optical imaging is the potential to image at various wavelengths in a relatively simple manner. In a multispectral setup, a series of lasers can be used to illuminate a sample at a multitude of discrete wavelengths. In a hyperspectral setup, a series of optical filters can be used to collect images at a series of wavelength ranges. Alternatively, a hyperspectral illumination source can be combined with an imaging spectrometer to collect hyperspectral images. Multispectral ADI has been previously demonstrated by the Chapman group with a series of three laser diodes a 670 nm, 808 nm, and 975 nm. A series of resolution targets ranging from 100 μm to 200 μm were resolved at all three wavelengths when positioned in the center of a cuvette filled with a milk dilution. A series of resolution targets ranging from 220 μm to 520 μm were positioned in the center and at the illumination surface of a chicken breast slab ranging from 2.2 mm to 5 mm thick. Generally contrast improved at longer wavelengths, and with thinner scattering samples as expected. The reduced scattering coefficient of milk was expected to decrease at longer wavelengths, resulting in higher contrast at longer wavelengths [37].

Previously, the author performed a multispectral study was conducted with a tunable pulsed laser light source (Appendix B) [29]. The laser was tuned to 13 wavelengths ranging from 460 nm to 700 nm at 20 nm increments. A 0.7 mm attenuating target was submerged in four Intralipid® concentrations ranging from 0.15% to 0.30% and the contrast of the target was measured for each wavelength and scattering sample. Contrast was found to improve at

longer wavelengths and at lower scattering levels. The scattering of Intralipid® was expected to decrease at longer wavelengths.

A third study was conducted by the Carson group with a broad band light source (Quartz Tungsten Halogen lamp) and an imaging spectrometer that was capable of imaging the one-dimensional AFA, at a spectrum of wavelengths in the near infrared region. In the study, solid tissue mimicking phantoms were constructed with various ICG inclusions with different concentrations embedded at a range of depths. In addition, mouse tissue sections were imaged. Tumorous tissue and muscle tissue from a mouse were both identifiable by their spectral signatures [39].

1.9 Motivation

Based on the review of literature in previous sections, it can be deduced that an AFA-based ADI system can image through tissue samples thinner than 1 cm. The depth penetration of quasi-ballistic light limits the potential applications of a quasi-ballistic based imaging system. Such an imaging system can potentially be used to image the various structures within a finger *in vivo*, or to detect early dental decay in teeth [12,50]. An AFA-based ADI system can also be used to image tissue samples *ex vivo* such as surgically resected tissue samples. The surgical treatments of several types of cancer require an excised sample to be examined by a pathologist to determine if there are any cancerous cells along the tumor margins. Positive margins will often necessitate the removal of additional tissue. The tissue examination can be performed days after the surgery using conventional slicing and staining techniques or it can be performed intra-operatively using frozen section analysis [51]. An AFA-based ADI system can potentially be used as a tool in the operating room to complement or even replace frozen section analysis. Such a system can also be used to provide objective analyses of surgically resected tissue samples [39,52]. Outside of the surgery room, an ADI system can potentially aid pathologists by increasing the throughput of conventional tissue analyses. ADI requires minimal manipulation of the sample prior to imaging, and can potentially analyze greater volumes of pathological samples. ADI can also

potentially be used to image structures and stains that are not visible using current pathology techniques, and may provide additional information to a pathologist.

While the limitations of ADI prevent whole body imaging of humans due to size restrictions, it can be utilized to image small animals that fit the size criteria. ADI has previously been used to image the tail of a mouse pup (Carson group) and a zebrafish (Chapman group) [35,53]. Preliminary results in biological imaging suggest that this technology can be developed into a small animal imager that has potential applications in many biological studies. Fluorescent markers that outline disease or anatomy can be studied within a sample. For small animals, the entire animal can be imaged without the need for sacrificing the animal. Consequently, longitudinal studies can be performed. For example, the progression of a disease model can be tracked optically and analyzed. Currently, optical small animal imagers have not been adopted widely for research purposes due to cost and image quality. An AFA-based ADI imaging system can potentially be incorporated into a low cost small animal imaging system that provides the contrast and resolution needed for biological studies.

In addition to biological studies, ADI can be used for other imaging applications. Scatter rejection imaging systems can be employed to image objects obscured by fog, smoke or haze. It can also be used for research purposes to study the flow of fluid through an atomizer [54]. Such a study is relevant to the optimization of fuel combustion. Optical imaging has also been used to develop quality control systems for food products. For example, an optical trans-illumination and reflectance imaging system was used to detect the presence of embedded bones within a chicken breast sample [55]. ADI shows great potential as an imaging modality as it provides the high contrast of optical imaging with minimal cost and instrumentation.

1.10 Thesis objective and scope

Based on the review of the literature in the previous sections, a major limitation of current AFA-based ADI can be identified. A large proportion of the light used to illuminate an AFA is lost due to the small sampling area of the AFA. Consequently, an AFA-based ADI

system is inefficient. In addition, the current AFA can only capture information in one dimension at a time. As a result, a two-dimensional image requires extensive scanning. The extensive scanning is a major hurdle for ADI as image acquisition times are currently too long to be adopted for any clinical applications. A two-dimensional angular filter array can significantly improve AFA-based ADI, and potentially bring AFA-based ADI closer to finding clinical applications. The improved acquisition speed of a 2D AFA will also enable the collection of multispectral images in a clinical setting. The entirety of this work describes our approach to design a two-dimensional AFA. The early work sought to evaluate an initial prototype of a two-dimensional AFA, and to optimize the design parameters to improve image contrast. From there, a more rigorous analysis was conducted on the resolution of the system, and a new optical setup was designed to facilitate the imaging of more complex phantoms and eventually biologically relevant samples.

The focus of Chapter 2 is aimed towards the initial design and prototyping stages of the two-dimensional AFA. The chapter discusses the new fabrication method and its advantages over the previous fabrication methods. Initial experiments regarding contrast were conducted to optimize the acceptance angle for imaging scattering samples.

The work in Chapter 3 introduces a new system design that is capable of imaging biologically relevant samples. The data acquisition was improved to increase the sampling rate of the system. In addition, a rigorous resolution measurement was conducted to evaluate the performance of the system. Biologically relevant samples were imaged and reported.

The goal of this work was to create a biological imaging system that is capable of obtaining projection images of a scattering sample quickly, and at a low cost. Several complex methods of scatter rejection are currently being explored and have been demonstrated to be effective at specific imaging tasks. ADI is a robust imaging technique that can be employed to image a wide range of samples and can have a multitude of applications. In this thesis, a preliminary design of a 2D AFA is presented and the contrast and resolution of the system is evaluated. In the future, the system can be improved to acquire images at a faster rate and with higher contrast and resolution. The system can also

be further developed to image thicker or more scattering samples. Finally, the system can be tailored to perform specific imaging tasks more effectively.

1.11 References

1. J. C. Hebden, S. R. Arridge, and D. T. Delpy, "Optical imaging in medicine: I. Experimental techniques," Phys. Med. Biol. **42,** 825-840 (1997).

2. A. P. Gibson, J. C. Hebden, and S. R. Arridge, "Recent advances in diffuse optical imaging," Phys. Med. Biol. **50,** R1-43 (2005).

3. J. Mobley and T. Vo-Dinh, "Optical Properties of Tissue," in *Biomedical photonics handbook,* T. Vo-Dinh, ed. (CRC Press, 2003).

4. S. L. Jacques, C. A. Alter, and S. A. Prahl, "Angular dependence of HeNe laser light scattering by human dermis," Laser Life Sci **1,** 309 (1987).

5. W. F. Cheong, S. A. Prahl, and A. J. Welch, "A review of the optical properties of biological tissues," Quantum Electronics, IEEE Journal of **26,** 2166-2185 (1990).

6. A. C. Boccara, "Imaging through scattering media," in *Encyclopedia of Modern Optics,* B. D. Guenther, A. Miller, L. Bayvel, and J. E. Midwinter, eds. (Academic Press, 2004), pp. 143.

7. J. G. Fujimoto, "Optical coherence tomography for ultrahigh resolution in vivo imaging," Nature Biotech. **21,** 1361 (2003).

8. A. Dubois, L. Vabre, A. C. Boccara, and E. Beaurepaire, "High-resolution full-field optical coherence tomography with a Linnik microscope," Appl. Opt. **41,** 805-812 (2002).

9. W. Drexler, "Ultrahigh-resolution optical coherence tomography," J. Biomed. Opt. **9,** 47-74 (2004).

10. L. Wang, P. P. Ho, and R. R. Alfano, "Time-resolved Fourier spectrum and imaging in highly scattering media," Appl. Opt. **32,** 5043-5048 (1993).

11. Q. Z. Wang, X. Liang, L. Wang, P. P. Ho, and R. R. Alfano, "Fourier spatial filter acts as a temporal gate for light propagating through a turbid medium," Opt. Lett. **20,** 1498-1500 (1995).

12. S. Andersson-Engels, R. Berg, S. Svanberg, and O. Jarlman, "Time-resolved transillumination for medical diagnostics," Opt. Lett. **15,** 1179-1181 (1990).

13. L. Wang, P. P. Ho, C. Liu, G. Zhang, and R. R. Alfano, "Ballistic 2-d imaging through scattering walls using an ultrafast optical kerr gate," Science **253,** 769-771 (1991).

14. L. V. Wang, "Ultrasound-mediated biophotonic imaging: a review of acousto-optical tomography and photo-acoustic tomography," Dis. Markers **19,** 123-138 (2003).

15. L. V. Wang, "Ultrasonic modulation of scattered light in turbid media and a potential novel tomography in biomedicine," Photochem. Photobiol. **67,** 41-49 (1998).

16. L. Wang, P. P. Ho, X. Liang, H. Dai, and R. R. Alfano, "Kerr - Fourier imaging of hidden objects in thick turbid media," Opt. Lett. **18,** 241 (1993).

17. P. Tsui, G. H. Chapman, R. L. K. Cheng, G. Chiang, N. Pfeiffer, and B. Kaminska,"Spatiofrequency filters for imaging fluorescence in scattering media" in *Proc. SPIE* **7562,** 75620B(2010).

18. P. B. L. Tsui, G. H. Chapman, R. L. K. Cheng, N. Pfeiffer, F. Vasefi, and B. Kaminska,"Spatiofrequency filter in turbid medium enhanced by background scattered light subtraction from a deviated laser source" in *Proc. SPIE* **7175,** 71750A(2009).

19. N. Pfeiffer, P. Chan, G. H. Chapman, F. Vasefi, and B. Kaminska,"Optical imaging of structures within highly scattering material using a lens and aperture to form a spatiofrequency filter" in *Proc. SPIE* **6854,** 68541D(2008).

20. G. Jarry, S. Ghesquiere, J. M. Maarek, F. Fraysse, S. Debray, Bui-Mong-Hung, and D. Laurent, "Imaging mammalian tissues and organs using laser collimated transillumination," J. Biomed. Eng. **6,** 70-74 (1984).

21. V. Prapavat, J. Beuthan, M. Linnarz, O. Minet, J. U. G. Hopf, and G. J. Mueller,"Infrared diaphanoscopy in medicine" in *Proc. SPIE* **2081,** 154-167(1994).

22. G. H. Chapman, M. Trinh, N. Pfeiffer, G. Chu, and D. Lee, "Angular domain imaging of objects within highly scattering media using silicon micromachined collimating arrays," Selected Topics in Quantum Electronics, IEEE Journal of **9,** 257-266 (2003).

23. N. Pfeiffer, "Imaging of turbid media using trajectory filter methods," *PhD Thesis Simon Fraser University* (2009).

24. L. Wang, S. L. Jacques, and L. Zheng, "MCML--Monte Carlo modeling of light transport in multi-layered tissues," Comput. Methods Programs Biomed. **47,** 131-146 (1995).

25. H. J. van Staveren, C. J. Moes, J. van Marie, S. A. Prahl, and M. J. van Gemert, "Light scattering in Intralipid-10% in the wavelength range of 400-1100 nm," Appl. Opt. **30,** 4507-4514 (1991).

26. G. H. Chapman, J. Rao, T. C. K. Liu, P. K. Y. Chan, F. Vasefi, B. Kaminska, and N. Pfeiffer,"Enhanced angular domain imaging in turbid media using Gaussian line illumination" in *Proc. SPIE* **6084,** 60841D(2006).

27. P. Chan, "Angular filters for angular domain imaging optical tomography in highly scattering media," *M. A. Sc Thesis Simon Fraser University* (2005).

28. M. Najiminaini, F. Vasefi, K. M. Tichauer, T. Y. Lee, B. Kaminska, and J. J. L. Carson, "Angular domain fluorescence lifetime imaging: a tissue-like phantom study," Opt. Express **18,** 23247-23257 (2010).

29. E. Ng, F. Vasefi, and J. J. L. Carson,"Multispectral angular domain imaging with a tunable pulsed laser" in *Proc. SPIE* **8225,** 82252C(2012).

30. E. Ng, F. Vasefi, B. Kaminska, G. H. Chapman, and J. J. L. Carson,"Contrast and resolution analysis of angular domain imaging for iterative optical projection tomography reconstruction" in *Proc. SPIE* **7557,** 755714(2010).

31. E. Ng, F. Vasefi, B. Kaminska, G. H. Chapman, and J. J. L. Carson,"Image contrast enhancement during time-angular domain imaging through turbid media by estimation of background scattered light" in *Proc. SPIE* **7182,** 71821C(2009).

32. E. Ng, F. Vasefi, M. Roumeliotis, B. Kaminska, and J. J. L. Carson,"Three-dimensional angular domain optical projection tomography" in *Proc. SPIE* **7897,** 78970V(2011).

33. M. S. Tank and G. H. Chapman, "Micromachined silicon collimating detector array to view objects in a highly scattering medium," Can. J. Elect. & Comp. Eng. **25,** 13 (2000).

34. F. Vasefi, "Advancements in angular domain optical imaging in biological tissues," *PhD Thesis Simon Fraser University* (2010).

35. F. Vasefi, M. Belton, B. Kaminska, G. H. Chapman, and J. J. L. Carson, "Angular domain fluorescence imaging for small animal research," J. Biomed. Opt. **15,** 016023 (2010).

36. F. Vasefi, P. K. Y. Chan, B. Kaminska, G. H. Chapman, and N. Pfeiffer, "An Optical Imaging Technique Using Deep Illumination in the Angular Domain," Selected Topics in Quantum Electronics, IEEE Journal of **13,** 1610-1620 (2007).

37. F. Vasefi, B. Kaminska, P. K. Chan, and G. H. Chapman, "Multi-spectral angular domain optical imaging in biological tissues using diode laser sources," Opt. Express **16,** 14456-14468 (2008).

38. F. Vasefi, B. Kaminska, G. H. Chapman, and J. J. L. Carson, "Image contrast enhancement in angular domain optical imaging of turbid media," Opt. Express **16,** 21492-21504 (2008).

39. F. Vasefi, M. Najiminaini, E. Ng, A. Chamson-Reig, B. Kaminska, M. Brackstone, and J. J. L. Carson, "Transillumination hyperspectral imaging for histopathological examination of excised tissue," J. Biomed. Opt. **16,** 086014 (2011).

40. F. Vasefi, M. Najiminaini, E. Ng, B. Kaminska, G. H. Chapman, and J. J. L. Carson, "Angular domain transillumination imaging optimization with an ultrafast gated camera," J. Biomed. Opt. **15,** 061710 (2010).

41. F. Vasefi, E. Ng, B. Kaminska, G. H. Chapman, K. Jordan, and J. J. L. Carson, "Transmission and fluorescence angular domain optical projection tomography of turbid media," Appl. Opt. **48,** 6448-6457 (2009).

42. F. Vasefi, B. S. L. Hung, B. Kaminska, G. H. Chapman, and J. J. L. Carson,"Angular domain optical imaging of turbid media using enhanced micro-tunnel filter arrays" in *Proc. SPIE* **7369,** 73691N(2009).

43. F. Vasefi, B. Kaminska, G. H. Chapman, and J. J. L. Carson,"Angular distribution of quasi-ballistic light measured through turbid media using angular domain optical imaging" in *Proc. SPIE* **7175,** 717509(2009).

44. A. O. Wist, P. P. Fatouros, and S. L. Herr, "Increased spatial resolution in transillumination using collimated light," IEEE Trans. Med. Imaging **12,** 751-757 (1993).

45. K. Shimizu and M. Kitama, "Fundamental study on near-axis scattered light and its application to optical computed tomography," Optical Review **7 (5),** 383 (2000).

46. K. Takagi, Y. Kato, and K. Shimizu, "Extraction of near-axis scattered light for transillumination imaging," Appl. Opt. **48,** D36-44 (2009).

47. K. Takagi, H. Kakinuma, Y. Kato, and K. Shimizu, "CW transillumination imaging by extracting weakly scattered light from strongly diffused light," Opt. Express **17,** 8332-8342 (2009).

48. J. A. Moon, R. Mahon, M. D. Duncan, and J. Reintjes, "Three-dimensional reflective image reconstruction through a scattering medium based on time-gated Raman amplification," Opt. Lett. **19,** 1234-1236 (1994).

49. J. C. Hebden and K. S. Wong, "Time-resolved optical tomography," Appl. Opt. **32 (4),** 372 (1993).

50. R. Jones, G. Huynh, G. Jones, and D. Fried, "Near-infrared transillumination at 1310-nm for the imaging of early dental decay," Opt.Express **11,** 2259-2265 (2003).

51. T. P. Olson, J. Harter, A. MuÃ±oz, D. M. Mahvi, and T. Breslin, "Frozen Section Analysis for Intraoperative Margin Assessment During Breast-Conserving Surgery Results in Low Rates of Re-excision and Local Recurrence," Annals of Surgical Oncology **14,** 2953-2960 (2007).

52. F. Vasefi, B. Kaminska, M. Brackstone, and J. J. L. Carson, "Hyperspectral angular domain imaging for ex-vivo breast tumor detection," 85870S-85870S (2013).

53. R. L. K. Cheng, P. B. L. Tsui, G. Chiang, and G. H. Chapman, "Optical imaging through non-transparent small aquatic creatures with angular-domain imaging," 78971X-78971X (2011).

54. J. B. Schmidt, Z. D. Schaefer, T. R. Meyer, S. Roy, S. A. Danczyk, and J. R. Gord, "Ultrafast time-gated ballistic-photon imaging and shadowgraphy in optically dense rocket sprays," Appl. Opt. **48,** B137-44 (2009).

55. S. Yoon, K. Lawrence, D. Smith, B. Park, and W. Windham, "Embedded bone fragment detection in chicken fillets using transmittance image enhancement and hyperspectral reflectance imaging," Sensing and Instrumentation for Food Quality and Safety **2,** 197-207 (2008).

Chapter 2

2 Angular domain imaging with a 2D angular filter array

This chapter is based on a research paper in preparation for submission to Applied Optics in 2013.

This chapter includes the fabrication method of a 2D AFA and initial characterization experiments that evaluate the performance of 2D AFAs with varying dimensions. Contrast of an absorbing target embedded in a scattering medium was evaluated with varying lengths of the angular filter.

2.1 Introduction

2.1.1 Optical trans-illumination imaging

In optical trans-illumination imaging, a sample is interrogated with a beam of light, and the transmission through the tissue is recorded. When imaging biological samples, light scattering often represents the most significant contribution to attenuation. Therefore, light transmission through thick biological samples is often limited by the scattering level. Many techniques have been developed to reduce the effect of scattering including, time gating and angular domain filtration [1-7]. Reduction of the contribution from optical scatter improves the estimate of optical absorption within the sample and generates an image that can be more easily interpreted.

In optical trans-illumination imaging, ballistic photons traverse the sample without experiencing scattering events and result in transmission images with the highest optical absorption contrast. However, very few ballistic photons survive after travelling through 1-2 mm of tissue [8]. Quasi-ballistic photons undergo several forward directed scattering events as they traverse the scattering sample. But, due to their non-direct paths, quasi-ballistic photons result in transmission images with a slight degradation in resolution and contrast compared to images resultant from ballistic photons. For thick scattering samples (optical path length between 5-10 reduced mean free paths) there are significantly more quasi-

ballistic photons compared to ballistic photons. As a result, an image produced by quasi-ballistic photons can be collected much faster than an image of comparable signal to noise collected with ballistic photons. The tradeoff in resolution and contrast for acquisition speed is often practical in many biomedical imaging applications.

When imaging through scattering samples, the majority of photons eventually experience at least one large-angle scattering event and certainty about the path travelled by any individual photon is lost. In addition to containing minimal information, these scattered photons may often scatter around an absorbing target resulting in an increase in transmission at the expected target location and a loss in image contrast. Many trans-illumination imaging techniques attempt to distinguish between the contributions from quasi-ballistic and scattered photons to generate projection images that faithfully represent the attenuation due to absorption processes [1-6,9].

2.1.2 Angular Domain Imaging (ADI)

In angular domain imaging quasi-ballistic and scattered photons are distinguished by the angle at which they exit the sample. Quasi-ballistic photons tend to retain their forward trajectory, and can be found near the axis of illumination. Scattered photons can be found travelling at large angles with respect to the axis of illumination. One implementation of ADI utilizes an Angular Filter Array (AFA) which consists of an array of micro-channels [10-15]. The micro-channel array acts as an optical Söller collimator. When the micro-channel array is aligned with the source of illumination, the ballistic and quasi-ballistic photons will pass through the filter, while the scattered photons will strike the walls of the filter and attenuate. The angular selectivity of the micro-channels is dependent on the aspect ratio of the channels.

In previous AFA designs by the Carson group, an array of micro-channels was etched into a silicon wafer, generating channels with an aperture size ranging from 20 μm x 20 μm to 80 μm x 80 μm and a channel length ranging from 1 cm to 2 cm [15]. Assuming perfect attenuation of incident photons by the channel walls, the silicon-based AFAs had acceptance angles ranging from 0.16° for the 20 μm x 20 μm x 1 cm array to 0.43° for the 80 μm x 80

μm x 1.5 cm array. Furthermore, the silicon-based AFAs were 1D, and consequently limited to imaging one line of the sample at a time. Two-dimensional projection images required raster scanning, which typically takes 10-60 minutes to complete depending on the application.

ADI has been shown to be an inexpensive alternative to other imaging modalities that incorporate scatter rejection methods (e.g. time domain systems), while still providing sub-millimeter resolution for samples up to 6 reduced mean free paths. The AFA approach to ADI is believed to be less sensitive to changes in optical wavelength compared to lens-based systems, and more appropriate for multi-wavelength or broadband imaging applications.

2.1.3 Dependence of ADI on illumination geometry

In trans-illumination optical imaging, contrast has been shown to be dependent on the geometry of the illumination and the detection [9]. In a previous ADI study conducted by the Chapman group, a resolution target submerged in a scattering medium was imaged with a silicon-based AFA. Contrast was improved when the illumination was structured with a slit compared to a full field illumination scheme [11]. With the 1D silicon-based AFA, a projection line image was representative of the quasi-ballistic photons within the illumination plane that passed through the sample. It was concluded that light from outside the illumination plane could potentially scatter into the AFA and reduce the contrast of the imaging system. By restricting the illumination to a thin plane of light, out of plane scattered light was significantly reduced.

2.1.4 Dependence of ADI contrast on AFA aspect ratio

Monte Carlo simulations of ADI conducted by the Chapman group have demonstrated that image contrast is dependent on the length of a micro-channel for a given AFA channel aperture size [11]. This simulation result was confirmed experimentally for ADI of scattering samples (4-6 reduced mean free paths) by the Carson group [15]. In both simulations and experiments, contrast improved with increasing AFA length for a given AFA channel aperture size. It was hypothesized that a longer AFA would result in an AFA with a larger aspect ratio. The increased aspect ratio would increase angular selectivity, and improve

contrast by increasing the ratio of quasi-ballistic to scatter photons. However, both studies noted that this relation was not observed when comparing AFAs with a different channel aperture size. For a given length, an AFA with a smaller channel aperture size was expected to have a higher angular selectivity than an AFA with a larger channel aperture size. However, this result was not observed in either experimental (Carson group) or simulation (Chapman group) studies and was attributed to diffraction effects as the channel aperture size was decreased [11,15].

2.1.5 Background scatter estimation in ADI

ADI systems distinguish between quasi-ballistic and scattered photons based on the exit angle from the sample. While this discrimination approach is successful at imaging through low scattering samples (< 5 reduced mean free paths) its performance is limited when imaging through samples of higher scattering. ADI systems are unable to distinguish between quasi-ballistic photons and scattered photons that have undergone multiple large angle scattering events and have scattered back into the acceptance cone of the angular filter. For highly scattering samples, the population of scattered photons is several orders of magnitude higher than the population of quasi-ballistic photons. Eventually, the background signal from scattered photons that scatter into the acceptance angle of the AFA overwhelms the signal from quasi-ballistic photons and image contrast is significantly reduced.

One method to reduce the contrast degradation from scatter contamination is by measuring the background scatter and subtracting the scatter signal [9]. In previous work with silicon-based AFAs conducted by the Carson group, a wedge prism (0.5° or 1°) was introduced in the optical path to deviate the illumination [13]. The image collected with the wedge prism contained little to no quasi-ballistic signal, and was used to estimate the background scatter using a technique called wedge subtraction. This technique improved contrast by 4-5 times. In another quasi-ballistic imaging system, a diffuser was used to reduce the quasi-ballistic signal and to obtain an estimate of the background scatter [16]. In this method, a 12-fold improvement in contrast was observed.

2.1.6 Objective and approach

The first objective of the work described here was to construct an ADI system that extended the conventional one-dimensional ADI systems to a 2D geometry (i.e. 2D AFA) to enable 2D imaging without the need for raster scanning. A 2D AFA can conceivably be constructed by precisely stacking a series of 1D silicon-based AFAs. However, the precise alignment of each AFA in the stack proved to be a significant technical hurdle. Instead, we hypothesized that 3D rapid prototyping may provide a simple and accurate method to fabricate 2D AFAs. The approach was to use a 3D printer to build a 2D AFA by stacking alternating layers of parallel strands of plastic in the *x*- and *y*-directions. In this way the width of each channel of the 2D AFA was controlled by the spacing and width of the parallel strands. The length of the AFA was determined by the number of layers printed.

The second objective of the work was to evaluate the effect of illumination geometry on ADI imaging with a 2D AFA. Based on the structured illumination findings of earlier work with silicon-based AFAs by the Chapman group, we hypothesized that structured illumination (i.e. sparsely structured illumination in 2D) would improve image contrast and resolution compared to full field illumination [11]. The approach was to image an attenuating target embedded in a scattering medium with a sparsely structured illumination pattern (utilizing an additional 2D AFA as a mask) and compare against an image collected with a full-field illumination (no mask). The contrast differences between the resulting images were analyzed to estimate the performance of the two different illumination schemes. A number of 2D AFAs of increasing length were tested as masks to determine whether the length of the illumination mask affected the contrasts of the images.

The third objective of this work was to devise a scatter estimation method based on principles analogous to the wedge prism (subtraction) technique used in silicon-based ADI work and to the diffused light subtraction technique [13,16]. The approach was to estimate the background scatter by moving the mask relative to the 2D AFA so that the illumination pattern due to the mask was coincident with the walls of the 2D AFA. We collected one image with the illumination pattern aligned with the apertures of the 2D AFA. A second image was collected with the illumination pattern aligned with the walls of the 2D AFA. This

image was used to provide an estimate of the background scatter. The background scatter estimate was then subtracted from the initial image collected with the channels aligned and the resulting change in contrast was measured.

2.2 Methods

2.2.1 Fabrication of the 2D AFA

A 2D AFA was constructed using 3D printing technology (Bits From Bytes BFB3000). The 3D printer consisted of a heated extruder mounted on a motorized *xy* positioner. An Acrylonitrile Butadiene Styrene (ABS) plastic filament was heated and applied on a layer by layer basis to build up the 2D AFA. The 2D AFA consisted of a series of micro-channels each with an aperture approximately 500 μm x 500 μm. The channels ranged in length from 1 cm to 15 cm. The designs resulted in an angular acceptance of 4.0° for the 1 cm long 2D AFA to 0.27° for the 15 cm long 2D AFA. The walls of the 2D AFA were designed to be approximately 500 μm wide. Each AFA contained 19 x 19 micro-channels and the total active area was 1.95 cm x 1.95 cm. Figure 2-1a shows a 3D exploded view of a 2D AFA during fabrication. Figure 2-1b shows a photograph (top view) of the 2D AFA, with the normal to the image parallel to axes of the micro-channels. The 3D printer applied ABS at a layer height of 0.25 mm. Each layer consisted of a series of parallel lines which formed the walls of the channels in one direction. Subsequent layers of parallel lines were applied in alternating directions, perpendicular to the previous layer to form the walls of the square channels in both directions. Each wall consisted of repeating layers of 0.25 mm ABS separated by 0.25 mm voids of air (Figure 2-1a). The discontinuous nature of the walls was expected to reduce the number of internal reflections within the channel by reducing the angle of incidence between photons and the walls of the channel. The effect of the wall patterning in the 2D AFA was expected to be similar to the ridge patterning in the reflection-trapped silicon-based AFAs used in previous work conducted by the Carson group [15].

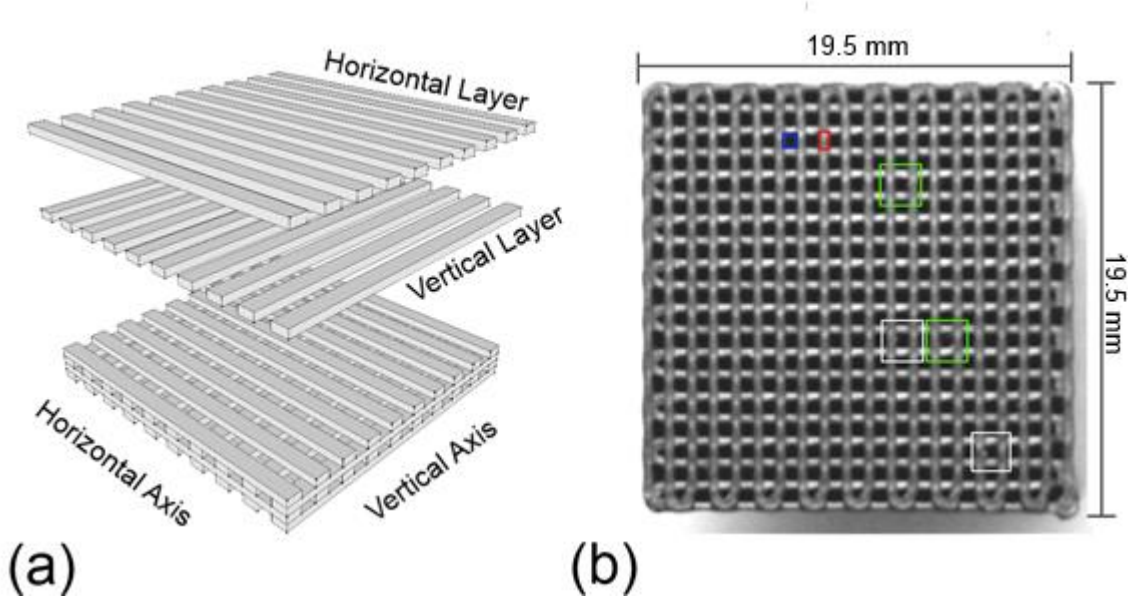

Figure 2-1: Two-dimensional angular filter array made from 3D prototyping. (a) 3D rendering of the AFA construction process with alternating horizontal and vertical parallel walls. Rendering not to scale. (b) Top view photograph of the AFA. Blue outline: channel aperture, red outline: channel wall. White outline, defective channels due to imperfections in plastic deposition. Green outline, channels with rounded edges.

2.2.2 Illumination and detection

Figure 2-2 displays a schematic of the AFA-based ADI setup. A 780 nm pulsed diode laser (PicoTA, PicoQuant) was filtered with a spectral filter (Comar 780 IL). The light was then focused with an f = 50 mm lens, and then spatially filtered with a 50 µm pinhole. The light emerging from the pinhole was then diverged with an f = -100 mm lens and then collimated with an f = 200 mm lens. The resulting collimated light was then directed at an illumination mask. The average power of the light illuminating the mask was 150 mW. The patterned light then passed through a 1 cm path length cuvette (Starna Cells 93/G/10) and the light emerging from the cuvette was collected through the 2D AFA. Detection was performed with a telecentric lens (Edmund Optics, 1.0 x NT55-350) mounted on a CCD camera (Photometrics Cascade 1K). The field of view was approximately 8 mm x 8 mm. The AFA was mounted on a 5 degree of freedom jig to align the AFA with the illumination beam. The illumination mask was mounted on a jig that provided 3 degrees of manual positioning as

well as motorized positioning in the *x* and *y* axes (using two Zaber T-LLS 260 linear slides). The motorized slides allowed for repeatable positioning to conduct the scatter estimation experiment.

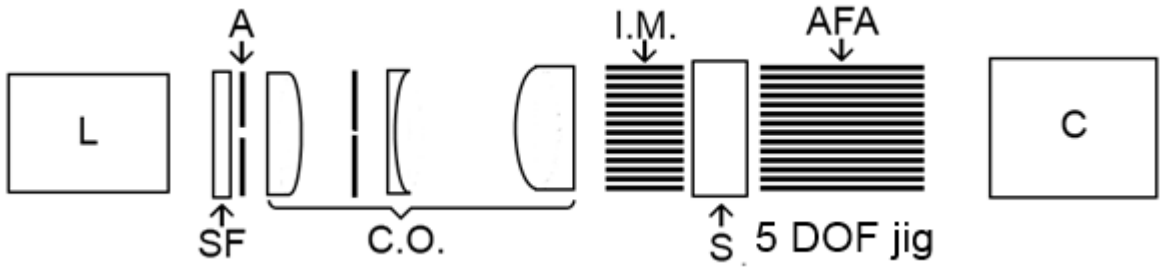

Figure 2-2: Schematic of the AFA-based ADI setup. Pulsed illumination at 780 nm from a laser (L) was spectrally filtered with a 780 ± 5 nm bandpass filter (SF), restricted with a 1 mm aperture (A) and collimated, expanded, and spatially filtered with collimating optics (C.O.). The collimated light passed through an illumination mask (I.M.), then through the sample (S) and the 2D AFA (AFA). The light was then detected with a CCD camera (C).

2.2.3 Imaging Target

A cylindrical absorbing target (0.9 mm diameter graphite rod) was used to generate image contrast. The absorbing target was positioned at the middle depth position (i.e. target center was 5 mm from the front surface) in a 1 x 5 x 5 cm (1 cm path length) glass cuvette filled with one of several Intralipid® solutions ranging from 0.5% to 0.7% diluted from a 20% Intralipid® stock solution. Intralipid® is a lipid emulsion that serves as a convenient uniform scattering medium for optical imaging experiments [17].

2.2.4 Image collection

Images were captured via Micromanager, a third party ImageJ plugin compatible with the Photometrics camera [18]. One image was captured for each set of experimental parameters. Exposure time was adjusted for each scattering level and 2D AFA length to

obtain the highest signal without saturating the detector. All images collected for normalization and scatter estimation were acquired with the same exposure time.

2.2.5 Analysis of fabricated 2D AFAs

The size of the AFA was measured experimentally by obtaining a trans-illumination image of a highly scattering homogenous sample (0.8% Intralipid® at 1 cm path length) with a 12 cm 2D AFA. The homogenous sample evenly illuminated each channel. The resulting image was thresholded to distinguish between the channels and the walls of the 2D AFA. The average size and standard deviation of the channels were computed from the thresholded image.

2.2.6 Contrast with sparsely structured illumination

To evaluate the effect of structured illumination on image contrast, the imaging target was imaged with an illumination mask and without an illumination mask. The mask was constructed using the same 3D printing technique as the 2D AFA. Five illumination masks, with different lengths (1 cm, 3 cm, 6 cm, 9 cm, and 12 cm) were placed in the optical setup and aligned with the 2D AFA (12 cm). Two images were collected with each of the five illumination masks, and without the illumination mask in place. The first image was collected with the absorbing target embedded in the scattering medium (0.5% Intralipid®), and a second image was collected without the absorbing target in place.

2.2.7 Contrast with varying aspect ratio

An experiment was performed to evaluate the effect of 2D AFA length on image contrast. A 3 cm long illumination mask was used to structure the illumination. Five 2D AFAs with different lengths (1 cm, 3 cm, 6 cm, 9 cm, and 12 cm) were placed after the sample and aligned with the illumination mask. For each of the five 2D AFAs one image was collected with the absorbing target in the scattering medium (0.5% Intralipid®) and one without the absorbing target.

2.2.8 Background scatter correction

An experiment was conducted to test the scatter estimation method. An absorbing target was imaged through each of three different scattering solutions (0.5%, 0.6%, 0.7% Intralipid®) with a 15 cm long 2D AFA and a 3 cm long illumination mask. Four images were collected for each scattering solution. Two images were collected with the absorbing target positioned at the center of the cuvette. The first image was collected with the illumination mask aligned to the 2D AFA. A second image was collected with the illumination mask shifted 500 μm in the y-direction (vertically). Two subsequent images were collected with an aligned and misaligned illumination mask without the absorbing target.

2.2.9 Image Analysis

All collected images were pre-processed before analysis. The 1004 x 1002 pixel images captured by the camera were down sampled to 7 x 7 or 8 x 8 pixel images by summing the signal representative of each channel output aperture. In some cases, each down-sampled 2D image was summed across each column to generate a 1D line profile. From these 1D line profiles, transmission profiles were calculated by normalizing the 1D line profile collected with the target in place to the respective 1D line profiles collected without target. Contrast (Eq. 2-1) was calculated as the normalized difference between the transmission observed at the pixel corresponding to an object (I_{object}) and the background transmission intensity ($I_{background}$). The background transmission intensity was measured by averaging the transmission signal at the two pixels neighboring the object.

$$Contrast = \frac{I_{object} - I_{background}}{I_{object} + I_{background}} \qquad \text{Eq. 2-1}$$

For the background estimation images, the misaligned (scatter weighted) raw image was subtracted from the aligned (scatter & quasi-ballistic weighted) raw image before proceeding with down-sampling, normalization and contrast analysis.

2.3 Results

2.3.1 Fabrication of the 2D AFA

Figure 2-1b shows a top view photograph of a typical 2D AFA. The image is a reflection image showing the last printed surface. The channel walls appear to be parallel, and the AFA is free from any large defects. Small defects can be seen in two channels. The defects are a result of excess plastic and can be found on the 8th channel from the right, 8th channel from the bottom and on the 4th channel from the right, 3rd channel from the bottom (Figure 2-1b, white). A few of the channels have rounded corners instead of square corners. The rounded corners can be seen in the 8th channel from the right, 5th channel from the top, and in the 6th channel from the right, 8th channel from the bottom (Figure 2-1b, green). Deviations from the square-shaped design are observable in Figure 2-3. The outlines of the channels are observable by the shapes of the low intensity signals in the images. The channel sizes are not constant across the entire AFA. In addition, the width and height varies within each channel due to the imperfect shape. The average width of each channel in both directions (width and height) was measured to be 485 ± 73 μm.

2.3.2 Contrast with sparsely structured illumination

Figure 2-3a shows an image of the 0.9 mm attenuating rod positioned parallel to the *y*-axis, submerged in 0.5% Intralipid® collected with no illumination mask. Figure 2-3b displays an image of the same target collected with the addition of a 3 cm long illumination mask to the imaging apparatus. The images contained horizontal and vertical shadows which resulted from the effects of the walls of the 2D AFA. Contrast was higher when the target was imaged with the illumination mask. Within each individual channel in Figure 2-3, there appeared to be two separate distributions of light. The first signal corresponded to a bright region near the center of the channel. The second signal appeared to have a uniform intensity across the entire channel area, and had a lower intensity than the first central signal. The absorbing target was positioned to block the channels within the 4th column from the left parallel to the *y*-axis. The bright signal central to each channel was not apparent in the channels that corresponded to the location of the absorbing target. The lower intensity second signal encompassing the entire area of the channel was observable in all of the channels in

the image. This second signal was less prominent for the image collected with the illumination mask in place.

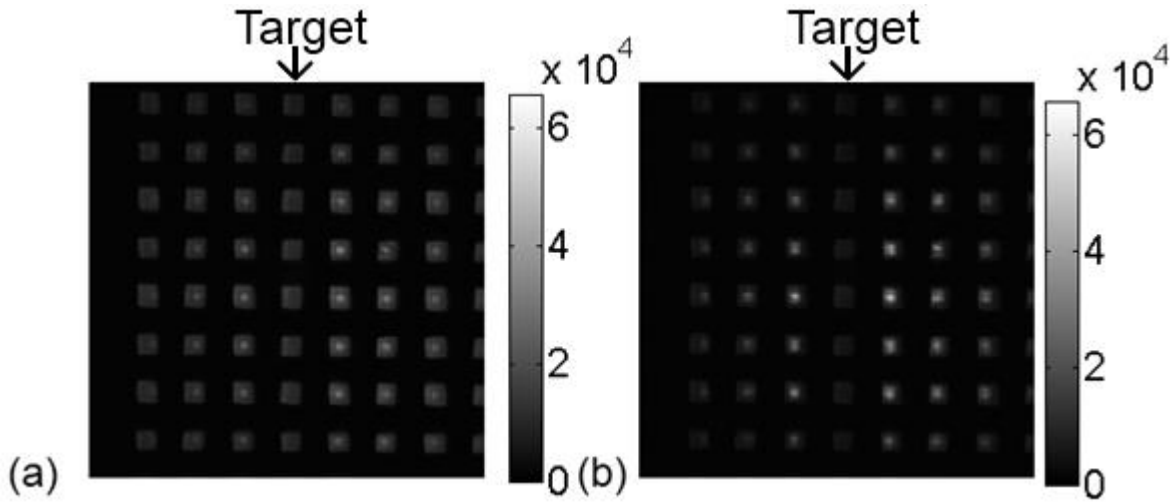

Figure 2-3: Raw AFA images of a 0.9 mm attenuating target in 0.5% Intralipid® dilution at 1 cm path length collected with a 2D AFA 12 cm in length. (a) No illumination mask, (b) 3 cm illumination mask. Field of view was 8 mm x 8 mm.

Figure 2-4a displays the normalized 1D line profiles of the target that were obtained with illumination masks of various lengths. The expected location of the absorbing target was at the 4th column of channels. In each of the 1D line profiles (Figure 2-4a), the transmission at the expected target location was lower than the transmission on either side of the target location. Without an illumination mask (Figure 2-4a, blue), the transmission at the 4th channel column was higher (0.72) compared to images collected with illumination masks (0.61-0.63) (Figure 2-4a, dark green, red, teal, purple, olive green). The average transmission on either side of the target location was lower for the image collected with no illumination mask (0.84) compared to the images collected with illumination masks (0.91). The contrast of the target was higher (0.18-0.2) when the image was acquired with an illumination mask compared to an image acquired with no illumination mask (0.08). Contrast was insensitive to the varying lengths of the illumination masks. Figure 2-4b displays contrast as a function of the length of the illumination mask.

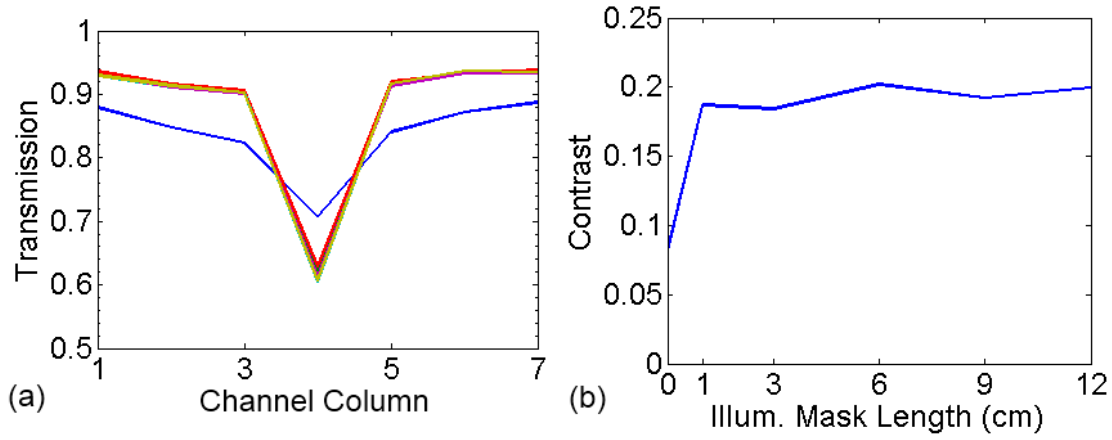

Figure 2-4: Transmission (a) and contrast (b) of a 0.9 mm attenuating target in 0.5% Intralipid® dilution at 1 cm path length with a 12 cm 2D AFA and varying illumination mask length. Target was located at the 4th channel column. (a) blue: no mask, dark green: 1 cm mask, red: 3 cm mask, teal: 6 cm mask, purple: 9 cm mask, olive green: 12 cm mask.

2.3.3 Dependence of contrast on aspect ratio

Figure 2-5a displays normalized 1D line profiles of the target that were obtained with 2D AFAs of different lengths. The expected location of the absorbing target was at the 5th column of channels. Normalized transmission at the target location ranged from 0.45 when imaged with a 12 cm 2D AFA (Figure 2-5a, yellow) to 0.82 when imaged without a 2D AFA (Figure 2-5a, blue). Normalized transmission on either side of the target location ranged from 0.80 when imaged with a 1 cm 2D AFA (Fig. 2-5a, green) to 0.90 when imaged with a 12 cm 2D AFA (Figure 2-5a, yellow). Generally, transmission at the target location decreased and transmission on either side of the target location increased as the length of the 2D AFA increased.

Figure 2-5b displays the contrast of the attenuating target as a function of the length of the 2D AFA. Contrast ranged from 0.01 when the target was imaged without a 2D AFA to 0.34 when the target was imaged with a 2D AFA 12 cm in length. Generally, contrast increased as the length of the 2D AFA increased. The trend was more pronounced for shorter

2D AFA lengths (0 - 6 cm). The contrast plateaued at approximately 0.3 for 2D AFAs 6 cm and longer.

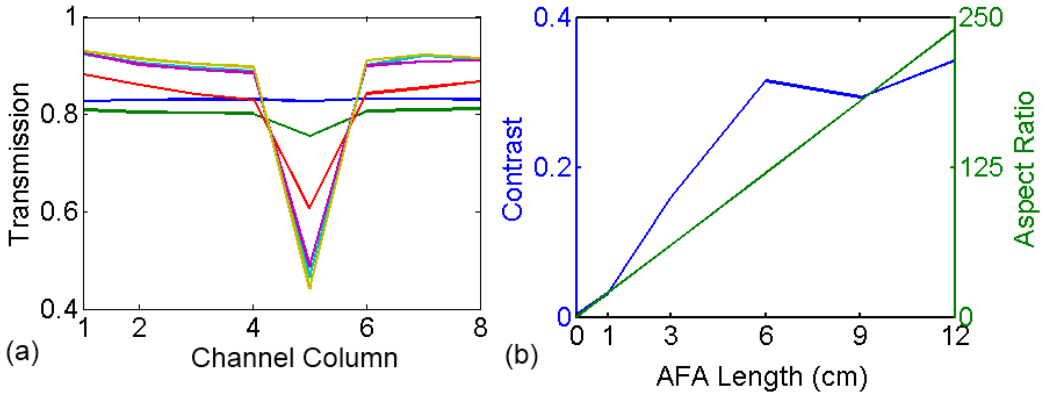

Figure 2-5: Transmission (a) and contrast (b) of a 0.9 mm attenuating target in 0.5% Intralipid® dilution at 1 cm path length with a 3 cm illumination mask and varying 2D AFA lengths. (a) blue: no AFA, green: 1 cm AFA, red: 3 cm AFA, teal: 6 cm AFA, purple: 9 cm AFA, yellow: 12 cm AFA.

2.3.4 Background scatter estimation

Figure 2-6(a-c) shows the performance of the background scatter subtraction method for images collected at three scattering levels: 0.5%, 0.6% and 0.7% Intralipid® at 1 cm path length respectively. The images were collected by subtracting the background estimation image from the original image. In the background scatter estimation images, the target was expected to be located at the 4th column of channels (parallel to the *y*-axis). In each of the subtraction images, little to no signal was observed at the target location. When imaging through 0.5% and 0.6% Intralipid® (Figure 2-6 a&b), the background corrected signal was <0.05 at the target location. When imaging through 0.7% Intralipid® (Figure 2-6c), the background corrected signal was 0.47 at the target location. A large signal was observed in the columns of channels where no target was present. The signal beside the target location was approximately 5 times larger when imaging through lower Intralipid® concentrations (0.5%, 0.6%) compared to the image collected at a higher Intralipid® concentration (0.7%).

Figure 2-6d shows the normalized transmission profiles of the absorbing target at the three different scattering levels. Transmission at the target location ranged from 0.04 for images collected at 0.5% and 0.6% Intralipid® to 0.5 for the image collected at 0.7% Intralipid®. Transmission beside the target location ranged from 0.95 to 1.05. Contrast was similar for the images collected at 0.5% and 0.6% Intralipid®, while contrast was lower when imaging through 0.7% Intralipid®.

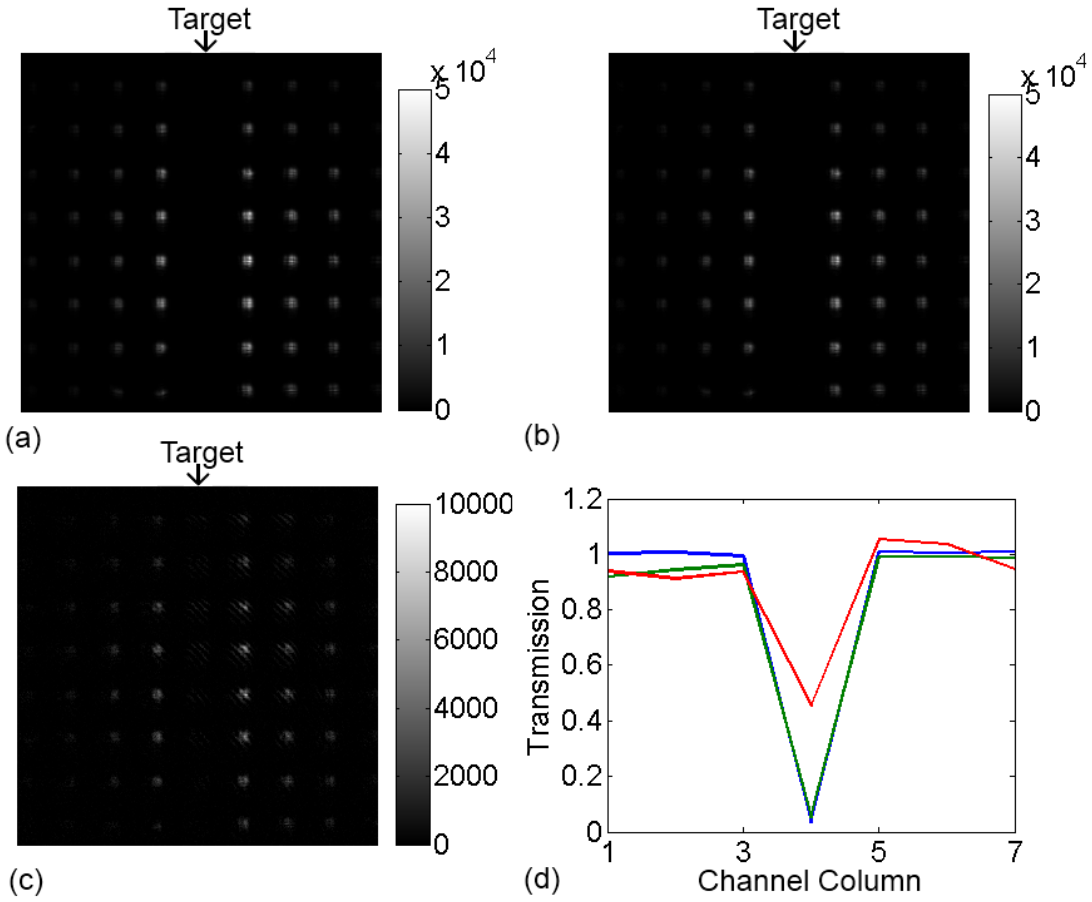

Figure 2-6: (a-c) AFA images of a 0.9 mm attenuating target in Intralipid® dilution at 1 cm path length collected with a 15 cm 2D AFA and 3 cm illumination mask after background subtraction. (a) 0.5% Intralipid®, (b) 0.6% Intralipid®, (c) 0.7% Intralipid® d) Transmission at varying Intralipid® concentrations at 1 cm path length, blue: 0.5% green: 0.6%, red: 0.7%.

2.4 Discussion

2.4.1 General

2D AFAs were successfully fabricated using commercially available 3D rapid prototyping. The fabrication process produced observable flaws which resulted in small defects in the resulting AFAs. The 2D AFAs were successfully employed to acquire two-dimensional images of an absorbing target embedded in a scattering material. Image contrast was found to be dependent on the length of the 2D AFA. Image contrast was also found to improve more than two fold when an absorbing target was imaged with a sparsely structured illumination. Finally, a background scatter estimation method was devised and demonstrated to improve contrast.

2.4.2 Fabrication of the 2D AFA

The 2D AFA fabricated with the 3D printer enabled angular domain imaging of targets embedded in a scattering medium. The 2D AFAs represent a significant improvement over previous 1D silicon-based AFAs as they allow for the imaging of two dimensions simultaneously. Even though 3D printing technology was ideal for constructing a 2D AFA, the resultant AFAs had several observable imperfections. As mentioned previously, a few of the channels had rounded corners instead of square corners. The rounded corners appear to be an artifact form the fabrication process. The 3D printer applied a 2D layer of a heated plastic filament directly onto a previously printed layer. In order to obtain a strong bond between the two layers, the plastic filament must be hot enough to adhere to the previous layer. The high temperatures and the subsequent cooling processes can potentially alter the shape of the channels from the original square design. A second fabrication defect consisted of excess plastic that was found in the channels. The excess plastic found on the printed object was a result of leftover residue on the heated extruder. Excess plastic can adhere to the extruder during the printing process, and can be easily deposited elsewhere as the extruder moves across the printed object. The excess plastic was a source of several imperfections in the 2D AFA.

Figure 2-1b shows a reflective photograph of the 2D AFA that highlights the last printed surface on the AFA. Figure 2-3 displays a transmission image through the AFA. The image collected in Figure 2-3 represents a combination of the imperfections of approximately 480 printed layers, whereas the imperfections observed in Figure 2-1a display only the imperfections on the top two printed layers. The standard deviation in the channel sizes amounted to approximately 15% of the linear size of the channels. In comparison to the MEMS-based fabrication method used for silicon-based AFA designs, FDM based 3D printing was significantly less precise and generated more significant variations in channel aperture size.

2.4.3 Contrast with structured illumination

Figure 2-3 shows that the signal output from the 2D AFA consisted of a bright concentration of light in the center of the channel and a low intensity background signal that was relatively constant across the entire channel. In previous trans-illumination ADI studies conducted by the author, a quasi-ballistic signal and a scatter signal was often observed [14]. The bright concentration of light at the center of the channel was consistent with the quasi-ballistic signal, as it was apparent in every channel without an absorbing target, and it was not apparent in channels corresponding to the attenuating target. The lower intensity signal surrounding the centrally located signal was consistent with the background scatter signal as it was detected in all channels, including the channels corresponding to the attenuating target. Figure 2-3b shows a reduced background scatter signal compared to Figure 2-3a. The signal difference suggested that the illumination mask reduced the background scatter signal in comparison to the apparatus without the illumination mask

The contrast improvement resulting from the use of an illumination mask was apparent again in Figure 2-4a. Due to their tortuous nature, scatter photons can potentially scatter around an absorbing target, reducing the attenuating signal at the expected target location. In addition to reducing the attenuation signal at a target location, scattered photons can also increase the attenuation signal in areas not obscured by a target by smearing the attenuation signal. The illumination mask increased image contrast by reducing the transmission through channels corresponding to the attenuating target, and increasing the

transmission through channels representative of the background area. The results suggest that the illumination mask improved contrast by reducing the scatter signal in the image.

The illumination mask reduced much of the excess illumination that was not used for quasi-ballistic imaging. By reducing the excess illumination, the illumination mask affected the quasi-ballistic signal minimally, while significantly reducing the scatter signal. Consequently, the images with an illumination mask were subject to less scatter contamination, and most of the attenuation signal observed was attributed to the attenuation of quasi-ballistic photons instead of scatter photons.

To match the shape of the illumination mask with the 2D AFA, the mask was constructed using the same fabrication process. One consequence of this approach was that the mask placed in front of the sample could potentially serve as both an illumination mask, and a source collimator. A collimated light source has been shown to improve the spatial resolution and contrast of trans-illumination imaging systems [19]. Referring now to the experiments presented in Figure 2-3 and Figure 2-4, if the illumination mask acted to collimate the light source, then image contrast would be expected to improve with the length of the illumination mask. Conversely, constant contrast with respect to length of the illumination mask would be indicative that the improvement to the collimation of the light had not occurred. We observed that contrast varied minimally with the length of the illumination mask, but the presence of the mask (for any length tested) improved the contrast from 0.08 to ~0.2. The insensitivity of contrast to mask length suggested that the mask was selectively blocking light, and not acting as an illumination collimator. This result was expected as the illumination source was a collimated laser. Potentially, an illumination mask can be used with a non-collimated light source, such as an LED or lamp, thereby resulting in structured illumination that is collimated and suitable for angular domain imaging.

2.4.4 Contrast with varying acceptance angle

Generally, contrast improved when images were collected with a longer 2D AFA (see Figure 2-5). The contrast improved with longer 2D AFAs because the longer 2D AFAs were more successful at rejecting scattered photons. The contrast improvement with respect to

longer AFA length was consistent with previous ADI studies utilizing silicon-based angular filters [11,15]. Silicon-based AFAs typically have channel sizes ranging from 20-100 μm wide. In the previous studies, diffraction effects were observable in some situations. In this current study, the AFA channel aperture size was 500 μm and diffraction effects were not expected to be observed with the 2D printed AFAs.

Contrast improved significantly as the length of the 2D AFA increased for lengths 6 cm and shorter (see Figure 2-5). Contrast improved minimally for 2D AFA lengths 6 cm and longer. The finding suggested that when imaging through 0.5% Intralipid® at 1 cm, the majority of the scattered photons can be rejected with a 6 cm long 2D AFA. The length at which the contrast improvement plateaued was expected to be dependent on the scattering medium as well as the absorbing target. Based on the results of this study, one can conclude that longer AFAs have better imaging capabilities (contrast and scattering level). Other than reducing the overall system length, a shorter AFA did not appear to have any advantages over a longer AFA with the same channel aperture size.

The images collected to perform the contrast measurements were challenging to obtain. Typically, in an AFA imaging setup, the distance between the AFA and the camera must be controlled to reduce out of focus effects. When imaging AFAs with different lengths, the distance between the exit face of the AFA and the camera was not fixed. To partially overcome this limitation, the system was designed with a telecentric lens to minimize the potential artifacts related to small differences in depth of field due to the positioning of each 2D AFA. Since the telecentric lens introduced a level of angular filtration, the aperture of the lens system was kept in the full open position during contrast experiments to ensure the angular filtration of the 2D AFA dominated the lens angular filtration. In the AFA images, the signal between channels were well spaced apart. The 1D profiles were obtained by summating the signal within each channel. The different distances between the AFA and the camera may introduce some blurring effects due to focusing issues. However, the image analysis was robust against blurring effects as the signal for each channel was summated individually before analysis.

2.4.5 Background scatter estimation

The background estimation method was successful at estimating the background signal for the lower scattering levels (i.e. 0.5% and 0.6% Intralipid®). The signal obtained at the position of the attenuating target with the mask misaligned corresponded to the signal obtained at the same position when the mask was aligned with the AFA. After the subtraction of the scatter signal, the resultant image showed a transmission value near 0 at the target location. This significant reduction in signal at the target position resulted in a large increase in contrast. The background estimation method was not as successful when imaging through highest scattering level (0.7% Intralipid®). At the highest scattering level, the method failed to accurately measure the amount of scattered light. As a result, there was considerable signal remaining at the target position after the background subtraction step. In addition, the intensity of the subtracted image was significantly lower for the 0.7% Intralipid® image compared to the 0.5% and 0.6% Intralipid® image. This result was expected as the quasi-ballistic signal was expected to decrease with a more scattering sample.

The background scatter estimation method significantly improved all of the images collected compared to non-corrected images. The contrast of the images collected at 0.5% and 0.6% Intralipid® was close to 1 after the background scatter was removed. The contrast of the target collected at 0.7% Intralipid® was also improved with this scatter estimation method. While a comprehensive contrast and depth analysis was not performed in this paper, the results suggested that for lower scattering levels ($\leq$ 0.6% Intralipid® at 1 cm), the background scatter estimation method could be used to obtain image contrast that was insensitive to scatter. In addition, the results suggested that at higher scattering levels, $\geq$0.7% Intralipid® at 1 cm, there were still a sufficient number of quasi-ballistic photons to form an image. The main difficulty at higher scattering levels was distinction between signal contributions from quasi-ballistic photons and scattered photons, which have leaked through the system. Given that target was observed even at the highest scattering level (0.7%), ADI with the 2D AFA may be capable of imaging at even higher scattering levels if the scattered photons leaking through the system can be measured more precisely. A higher dynamic range detector is one possibility for adapting the system to imaging at higher scattering levels.

2.5 Conclusions and future work

A 2D AFA was constructed for ADI using 3D printing technology. The printed angular filters were successfully used to image a 0.9 mm diameter attenuating rod submerged in a 0.5% Intralipid® dilution at 1 cm path length. The contrast of the image was improved twofold with the placement of a 2D AFA in front of the sample as an illumination mask. An experiment conducted with illumination masks of varying lengths suggested that the illumination mask in front of the sample did not improve the collimation of the illumination. A second experiment conducted with 2D AFAs of different lengths showed that contrast increased significantly for 2D AFAs up to 6 cm long. Contrast improvements were minimal for 2D AFAs longer than 6 cm. A background subtraction estimation method based on misalignment of the illumination mask was developed. A significant improvement in contrast was seen for three concentrations of Intralipid® (0.5%, 0.6% and 0.7%). The subtraction method was most successful at estimating the background scatter for lower scattering levels (0.5% and 0.6%). The 2D AFA represents a significant improvement over the previous 1D silicon-based AFA as it could acquire 2D projections with a single camera exposure. However, the resolution of the 2D AFA was dependent on the printing technology. The 2D AFA was limited to a channel periodicity of 1 mm due to a limitation in the thickness of the printed walls between channels, and the precision of the positioning stages in the printer. More precise 3D prototyping methods could be used to fabricate 2D AFAs with greater numbers of channels of smaller aperture size and periodicity.

2.6 Acknowledgements

This project was funded by a Natural Sciences and Engineering Research Council of Canada (NSERC) Discovery Grant to JJLC. EN was funded by a NSERC award (CGS-M), a joint Translational Breast Cancer Research Unit (TBCRU) and Canadian Institute of Health Research (CIHR) Strategic Training Program in Cancer Research and Technology Transfer award, and a SPIE student scholarship. The authors would like to acknowledge Dr. Fartash Vasefi for his insight in AFA based ADI imaging.

2.7 References

1. J. C. Hebden, R. A. Kruger, and K. S. Wong, "Time resolved imaging through a highly scattering medium," Appl. Opt. **30,** 788-794 (1991).

2. L. Wang, P. P. Ho, and R. R. Alfano, "Time-resolved Fourier spectrum and imaging in highly scattering media," Appl. Opt. **32,** 5043-5048 (1993).

3. L. Wang, P. P. Ho, C. Liu, G. Zhang, and R. R. Alfano, "Ballistic 2-d imaging through scattering walls using an ultrafast optical kerr gate," Science **253,** 769-771 (1991).

4. S. P. Schilders, X. S. Gan, and M. Gu, "Microscopic imaging through a turbid medium by use of annular objectives for angle gating," Appl. Opt. **37,** 5320-5326 (1998).

5. V. Prapavat, J. Beuthan, M. Linnarz, O. Minet, J. U. G. Hopf, and G. J. Mueller,"Infrared diaphanoscopy in medicine" in *Proc. SPIE* **2081,** 154-167(1994).

6. K. Shimizu and M. Kitama, "Fundamental study on near-axis scattered light and its application to optical computed tomography," Optical Review **7 (5),** 383 (2000).

7. L. Wang, P. P. Ho, X. Liang, H. Dai, and R. R. Alfano, "Kerr - Fourier imaging of hidden objects in thick turbid media," Opt. Lett. **18,** 241 (1993).

8. A. C. Boccara, "Imaging through scattering media," in *Encyclopedia of Modern Optics*, B. D. Guenther, A. Miller, L. Bayvel, and J. E. Midwinter, eds. (Academic Press, 2004), pp. 143.

9. K. Takagi, Y. Kato, and K. Shimizu, "Extraction of near-axis scattered light for transillumination imaging," Appl. Opt. **48,** D36-44 (2009).

10. M. S. Tank and G. H. Chapman, "Micromachined silicon collimating detector array to view objects in a highly scattering medium," Can. J. Elect. & Comp. Eng. **25,** 13 (2000).

11. G. H. Chapman, M. Trinh, N. Pfeiffer, G. Chu, and D. Lee, "Angular domain imaging of objects within highly scattering media using silicon micromachined collimating arrays," Selected Topics in Quantum Electronics, IEEE Journal of **9,** 257-266 (2003).

12. F. Vasefi, B. Kaminska, P. K. Chan, and G. H. Chapman, "Multi-spectral angular domain optical imaging in biological tissues using diode laser sources," Opt. Express **16,** 14456-14468 (2008).

13. F. Vasefi, B. Kaminska, G. H. Chapman, and J. J. L. Carson, "Image contrast enhancement in angular domain optical imaging of turbid media," Opt. Express **16,** 21492-21504 (2008).

14. E. Ng, F. Vasefi, B. Kaminska, G. H. Chapman, and J. J. L. Carson, "Contrast and resolution analysis of iterative angular domain optical projection tomography," Opt.Express **18,** 19444-19455 (2010).

15. F. Vasefi, M. Najiminaini, E. Ng, B. Kaminska, G. H. Chapman, and J. J. L. Carson, "Angular domain transillumination imaging optimization with an ultrafast gated camera," J. Biomed. Opt. **15,** 061710 (2010).

16. K. Takagi, H. Kakinuma, Y. Kato, and K. Shimizu, "CW transillumination imaging by extracting weakly scattered light from strongly diffused light," Opt. Express **17,** 8332-8342 (2009).

17. H. J. van Staveren, C. J. Moes, J. van Marie, S. A. Prahl, and M. J. van Gemert, "Light scattering in Intralipid-10% in the wavelength range of 400-1100 nm," Appl. Opt. **30,** 4507-4514 (1991).

18. A. Edelstein, N. Amodaj, K. Hoover, R. Vale, and N. Stuurman, "Computer Control of Microscopes Using μManager," *Curr. protocols in Mol. Biol.* **14,** 1 (2010).

19. A. O. Wist, P. P. Fatouros, and S. L. Herr, "Increased spatial resolution in transillumination using collimated light," IEEE Trans. Med. Imaging **12,** 751-757 (1993).

Chapter 3

3 Two-dimensional angular domain imaging with a 3D printed angular filter array

This chapter is based on a research paper that is in preparation for submission to Applied Optics in 2013.

This chapter includes the resolution analysis of a 2D AFA and presents images of various targets embedded in a homogenous scattering sample as well as a heterogeneous scattering sample. Attenuating targets embedded in a biological tissue sample were imaged using a 2D AFA. A raster scanning system was implemented to acquire an image devoid of shadow artifacts created by the walls of the AFA.

3.1 Introduction

3.1.1 Optical trans-illumination imaging

Optical trans-illumination imaging measures the attenuation of light as it traverses through a sample. Optical attenuation of collimated light in biological tissues is due to either scattering or absorption processes. In biological tissues, light penetration peaks in the near infrared (NIR) region where optical absorption is minimal, i.e. the tissue optical diagnostic window. Several optical trans-illumination imaging systems such as time gating [1-3] and angular domain [4-6] attempt to image the optical absorption of a target by filtering out the optical scatter.

In optical trans-illumination imaging, the photons collected by the detector can be grouped into three different types based on the path the photon travelled through the sample. Ballistic photons are those which have travelled through the sample without experiencing a scattering event. These photons are not corrupted by scatter events, and as a result, they generate images with the highest fidelity. However, when imaging through tissue samples thicker than 1-2 mm of tissue, very few ballistic photons survive [7]. Consequently, an image

of an optically thick sample generated from only ballistic photons will require a long acquisition time.

Optical scattering in tissue is often not isotropic and tends to be forward directed. Consequently, a small proportion of the photons travelling through a tissue sample undergo only a few small angle scattering events. These photons are termed quasi-ballistic or snake photons. As quasi-ballistic photons do not travel straight paths, an image generated from quasi-ballistic photons will often suffer from a slight decrease in contrast and resolution compared to an image generated from ballistic photons. However when imaging through thicker samples (5-10 reduced mean free paths), there are significantly more quasi-ballistic photons compared to ballistic photons. As a result, an image generated from quasi-ballistic photons can be obtained significantly faster than an image generated from purely ballistic photons. In many imaging applications, the tradeoff in contrast and resolution for increased acquisition speed is desirable.

When imaging through thicker tissue samples, a large proportion of the photons will undergo many large-angle scattering events. These photons contain little information regarding the imaging target, and often reduce the contrast and the resolution of the image. By removing the scattered photons prior to detection, the resulting image will more closely approximate the optical absorption of the sample [8,9].

3.1.2 Angular Domain Imaging (ADI)

In angular domain imaging, the different photon paths are determined by the angle at which a photon exits the sample. Since ballistic photons do not undergo any scattering events, they can be found exiting the sample at the same angle at which they entered. Quasi-ballistic photons are expected to undergo several forward directed scattering events. Consequently, quasi-ballistic photons are expected to exit the imaging sample at a small angle with respect to the axis of illumination. Scattered photons are expected to undergo many large angle scattering events, and they can be found exiting the sample over a large range of angles. In angular domain imaging, an angular filter is placed between the sample

and the detector to reject a large portion of the scattered photons, while transmitting most of the quasi-ballistic and ballistic photons.

One method of executing ADI utilizes an Angular Filter Array (AFA). An AFA is an array of micro-channels [5,6,10-13] which acts as an optical Söller collimator. As with a Söller collimator, the angular acceptance of the AFA is determined by the aspect ratio of the channels. When the collimator is aligned with the axis of illumination, quasi-ballistic and ballistic photons are expected to pass freely through the filter, while a large proportion of the scattered photons are expected to strike the walls of the angular filter and attenuate. ADI has been previously demonstrated by the Chapman and Carson labs as an inexpensive alternative to other trans-illumination imaging systems (e.g. time domain), while maintaining sub-millimeter resolution when imaging through samples up to 6 reduced mean free path lengths [11]. AFA-based ADI is a lens-less alternative to a conventional Fourier-based lens and pinhole filter [4,14-16]. A lens-less angular filtration method is not sensitive to lens aberrations during the filtration process, and is expected to be advantageous for multi-spectral or hyper-spectral imaging.

3.1.3 Two-Dimensional AFA

Previously MEMS-based technologies were used to create angular filter arrays. MEMS-based technologies were ideal for building angular filter arrays because of their high feature resolutions and the potential of inexpensive mass production. The first generation of angular filters consisted of micro-channels that were etched into a silicon wafer. The high feature resolutions of MEMS technology enabled the construction of Angular Filter Arrays with small cross sectional areas, ranging from 20 μm x 20 μm to 80 μm x 80 μm and lengths ranging from 1 cm to 2 cm [17]. Based on the aspect ratio, the angular acceptance of these channels ranged from 0.16° to 0.43°, assuming that the photons do not reflect off the walls of the channels. One limitation of the MEMS-based AFAs was the complicated prototyping stage. When constructing AFAs in low quantities, the fabrication process was relatively expensive. In addition, the AFAs were limited to one-dimensional arrays. With the one-dimensional array, a two-dimensional image was constructed by raster scanning. A two-dimensional AFA would conceivably be more efficient at acquiring images by requiring

minimal scanning compared to a one-dimensional AFA design. Scaling up to a two-dimensional array using MEMS technologies is inefficient since it requires stacks of 1D AFAs to be assembled and precisely aligned. To simplify the 2D AFA fabrication process, we recently introduced a technique to fabricate a two-dimensional AFA using additive 3D printing [18]. The new fabrication process greatly improved the prototyping speed as different AFA designs could be printed quickly without the need to design a lithography mask, which facilitated rapid optimization of the 2D AFA design.

3.1.4 AFA Scanning

In previous work conducted by the author, the images obtained by the 2D ADI system suffered from large artifacts due to the walls of the channels [18]. Each 500 μm channel was separated by a 500 μm wall. Due to the low fill factor of the printed AFA design, the walls of the AFA obstructed a large portion of the sample. Consequently, the images greatly under-sampled the imaging target. Images were sampled at a rate of 1 sample / mm^2. When imaging with a low sampling rate, the effective resolution of the imaging system was relatively large (1 mm). Previous resolution studies on silicon-based AFAs conducted by the author, show that an AFA with an aspect ratio of 250 can image at a resolution of 230 μm [19]. Therefore, we hypothesized that a higher sampling rate with the 2D AFA would improve the resolution of the 2D ADI system to a level comparable to the silicon-based 1D AFAs.

In the previous study of printed AFAs conducted by the author, a detailed contrast analysis was performed. A 0.9 mm diameter graphite rod was positioned in a glass cuvette filled with varying scattering solutions, and the contrast of the target was measured. However, due to limitations in the setup, the resolution of the system was never measured. Therefore, a more extensive resolution analysis on the 2D ADI system was required.

3.1.5 Structured illumination

In the previous 2D AFA study, the contrast of ADI images was shown to improve when the illumination source was patterned to match that of the 2D AFA [18]. The 2D printed AFA had a low fill factor (~25%) compared to the MEMS-based AFA design (~80%) [17]. When the illumination was patterned to match the AFA, the ratio of quasi-ballistic to

scattered photons was found to be dependent on the alignment of the illumination and the angular filter. When the illumination was aligned with the AFA, a large proportion of quasi-ballistic photons were observed. However, when the illumination was displaced and aligned to illuminate only the walls of the angular filter, few quasi-ballistic photons were observed. The results suggested that a full field illumination strategy was inefficient when imaging with the printed 2D AFAs and was consistent with previous studies on restricted illumination for trans-illumination imaging [20]. The results also suggested that a displaced mask could be used to estimate the amount of scattered light leaking through the AFA when imaging through high scattering levels. Contrast was found to improve when the image with the mask misaligned was subtracted from the image collected when the mask was aligned to the AFA. This method of contrast enhancement via scattered light estimation has been demonstrated previously with other trans-illumination imaging setups [8,9,13,21].

3.1.6 AFA channel crosstalk

In the previous study, quasi-ballistic photons were observed to be localized to one channel, i.e. the quasi-ballistic light detected in each channel originated from the light source illuminating that same channel. There was minimal crosstalk observed between channels for quasi-ballistic light. The distribution of the scattered light from illuminating one channel was not previously studied. When imaging through a sample with a more forward directed scattering such as tissue [22], the distribution of quasi-ballistic photons and scatter photons was not expected to be the same as the liquid phantoms. Quasi-ballistic crosstalk will introduce various artifacts in the acquired image, and must be accounted for in the acquisition protocol or during the image processing steps.

3.1.7 Objective and approach

The main objective of the work was to first construct a two-dimensional imaging system using a 2D AFA. Our approach was to utilize a two axis motorized positioning stage to shift the AFA in two axes reliably. The scanning allowed for the imaging of areas normally obstructed by the walls of the AFA to create an image devoid of shadow artifacts. The second objective of this work was to mimic the patterned illumination system presented

in the previous work and to synchronize the illumination patterns with the scanning AFA. Our approach was to incorporate a digital light processor (DLP) into the illumination path to create a highly customizable pattern of illumination (i.e. a structured light source). The programmable structured light source allowed the evaluation of varying illumination schemes and their effect on contrast and resolution of the ADI setup. The third objective of the work was to conduct a thorough resolution analysis of the imaging setup. The approach was to image a knife edge submerged in various scattering samples. The analysis of the edge response function generated by the knife edge provided an estimate of the system resolution. The resolution measurement was then confirmed by imaging attenuating targets of varying sizes while submerged in a scattering medium. The final objective of this paper was to image a biological tissue sample. Fresh domestic chicken breast was sliced into 1 cm thick samples and imaged with various attenuating targets positioned within the tissue sample.

3.2 Methods

3.2.1 AFA fabrication

The two-dimensional AFAs were printed with a commercial three-dimensional printer (Bits From Bytes, BFB3000). The 3D printer utilized a heated extruder that melted a plastic filament (Acrylonitrile Butadiene Styrene, ABS) at a controllable rate. The heated extruder was mounted on a motorized x-y positioner, which moved in controlled manner to print a two-dimensional cross section of the object. After the completion of a cross section, the print bed was lowered and the next cross section was printed until the 3D object was completed. The z-resolution of the printer was 0.125 mm while the x-y resolution of the printer was 0.2 mm.

The AFAs printed with the 3D printer had larger channels compared to previous generation of AFAs. The aperture of each channel was approximately 500 µm x 500 µm. The large channels were a result of the low resolution of the 3D printer and not a limitation of the fabrication process. Several high-resolution three-dimensional printers can achieve much finer resolutions [23].

To achieve a similar aspect ratio as the previous generation of AFAs, the channels of the 2D AFA were 12 cm long, significantly longer than the 2 cm channels in the previous design. Each AFA contained 29 x 29 channels for a total active area of approximately 3 cm x 3 cm. Figure 3-1a shows a three-dimensional rendering of an AFA being constructed, while Figure 3-1b shows a top view of the AFA. Due to the fabrication process, the walls of the channels were discontinuous. The discontinuous walls were expected to help trap the large angle photons by reducing the angle of incidence between the photon and the wall. The discontinuous walls were expected to behave similarly to the pattered walls in a previous AFA design proposed by the Carson group [11].

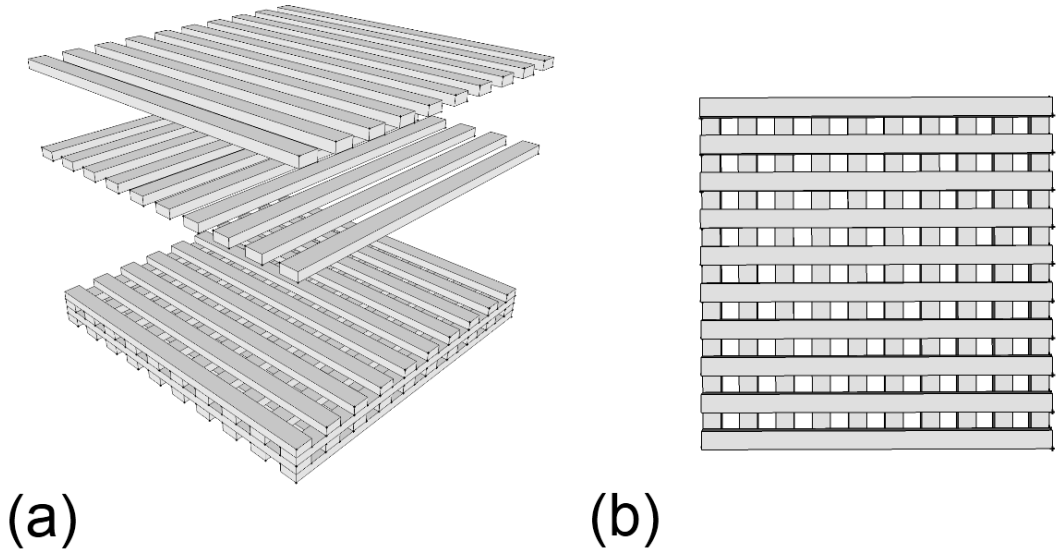

Figure 3-1: Two-dimensional angular filter array fabricated with 3D printing. (a) Exploded 3D rendering of the 2D AFA fabrication details with alternating horizontal and vertical parallel walls. (b) Top view of the AFA.

3.2.2 Illumination and detection

Figure 3.2 displays a schematic of the ADI setup. The illumination source was a 780 nm pulsed diode laser (PicoTA, Picoquant) emitting an average power of 150 mW. The laser beam then passed through the combination of a beam expander and spatial filter, which consisted of an f = 40 mm lens, a 50 µm pinhole, and an f = 200 mm lens. The resulting

collimated light was then directed to a spatial light modulator (Light Crafter, Texas Instruments). The Light Crafter consists of an LED light engine, a DLP chip, and a lens assembly. The DLP was extracted from the module for use with the laser source and external projection optics. The DLP chip contained an array of 608 x 684 pixels, and was controlled by displaying computer generated images through HDMI. The light reflected from the DLP chip was then expanded with a second beam expander (f = 50 mm, f = 200 mm). The patterned light then passed through an imaging sample. The liquid phantom studies were performed with a 1 cm path length cuvette (Starna Cells 93/G/10), while the biological tissue samples were contained in a custom designed cuvette with a 1 cm path length. The light emerging from trans-illumination of the imaging sample was then collected with a 2D printed AFA. The AFA consisted of 12 cm long channels each with an aperture of 500 µm x 500 µm. The AFA was mounted on a jig that provided 3 degrees of manual positioning as well as motorized positioning in the x and y axes (with two Zaber T-LLS 260 linear slides). The jig enabled the precise alignment of the AFA with the illumination source. The motorized positioning was used to raster scan the AFA. Detection was performed with a telecentric lens (Edmund Optics, 0.30x NT58-428) mounted on a CCD camera (Photometrics Cascade 1K). The field of view was approximately 15 mm x 8 mm. The internal aperture on the telecentric lens was positioned in the fully open position to minimize any angular filtration from the lens assembly. In this system, the field of view was limited by the size of the DLP chip and the beam expander used to project the patterned light.

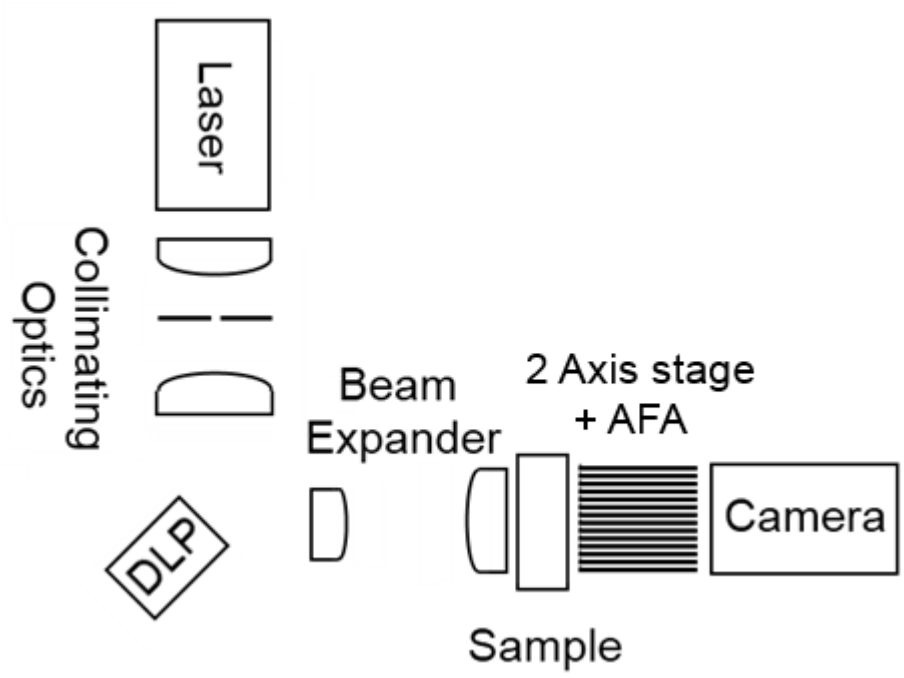

Figure 3-2: Schematic of the ADI setup. Laser: 780 nm pulsed diode laser, Collimating Optics: Lens-pinhole spatial filter, beam expander and collimator, DLP: 608 x 684 pixel DLP chip (Texas Instruments), Beam Expander: 4x beam expander, Sample: Cuvette filled with a scattering medium, AFA: 2D Angular filter array, Camera: CCD Camera with telecentric lens

3.2.3 Imaging Targets

Three imaging targets were used to evaluate the performance of the ADI system. The first target consisted of a razor blade positioned in the center of the glass cuvette. The glass cuvette was then filled with various scattering solutions. The scattering solutions were created by diluting a 20% Intralipid® stock solution to varying concentrations ranging from 0.40% to 0.75% at 0.05% increments. Intralipid® is a clinically approved lipid emulsion that can also be used as a convenient uniform scattering medium for optical imaging experiments [24]. The second target consisted of 4 rods of varying sizes positioned in the center of a 1 x 5 x 5 cm (1 cm path length) glass cuvette. The 4 rods were composed of one 200 µm diameter metal wire and three graphite rods with diameters of 500, 700 and 900µm. The rods were submerged in a cuvette filled with the same scattering solutions as the previous experiment

with the razor blade. The third imaging target consisted of a 1 cm thick sample of chicken breast placed between two parallel glass slides. The same four rods used in the previous experiment were positioned at varying depths in the chicken breast sample.

3.2.4 System resolution experiments

The resolution of the imaging system was measured via a knife edge experiment using a protocol similar to one described by Hebden [25]. A razor blade was positioned parallel to the front face of a 1 cm path length cuvette at the central depth position so that approximately half of the illumination beam was obstructed. The cuvette was then filled with one of several Intralipid® dilutions. For each Intralipid® dilution, two types of composite images were collected. The first composite image was collected with the illumination structured to match the apertures of the 2D AFA. The composite image was acquired by stitching together 64 separate image acquisitions designed to sample the all areas of the sample. For each image acquisition, both the AFA and the illumination pattern were translated to one of 8 x 8 grid points spaced 125 μm apart in both the *x*- and *y*-directions. A second composite image was acquired in a similar manner to the first composite image, except for the intentional misalignment of the illumination pattern and the AFA to obtain a background estimation image. A total of 128 images (i.e. 2 composite images) were collected for each razor blade experiment at each scattering level.

The resolution of the imaging system was then verified with a second experiment where four attenuating rods of different diameters (0.2 mm, 0.5 mm, 0.7 mm, 0.9 mm) were imaged through varying scattering levels. The four rods were positioned at the central depth of the 1 cm path length cuvette. The rods were mounted on a kinematic stage allowing the rods to be removed and replaced repeatedly. For each scattering level, two composite images were collected as described above.

3.2.5 Channel crosstalk experiments

AFA channel crosstalk was evaluated by imaging a point source through a scattering sample. A point source was generated by illuminating a single channel on the AFA. The resultant image indicated the degree of crosstalk between the illuminated channel and the

neighboring channels. Channel crosstalk was evaluated with a homogenous scattering sample and a heterogeneous scattering sample. The homogenous scattering sample consisted of a 1 cm path length cuvette filled with Intralipid® diluted to a series of concentrations ranging from 0.4% to 0.75%. The heterogeneous scattering sample consisted of three slabs of chicken breast tissue 6 mm, 8 mm and 10 mm thick.

3.2.6 Tissue imaging experiments

Two sets of tissue imaging experiments were performed with chicken breast. In the first set of experiments, a pair of attenuating rods (0.2 mm & 0.5 mm, 0.7 mm & 0.9 mm) was affixed to the outer surface of the imaging cuvette. The sample was then positioned in the ADI system such that the attenuating rods were positioned on the illumination side of the cuvette. Two composite images were then collected. The first composite image was collected with the attenuating rods in place, and a second composite image was collected with the attenuating rods removed. Both composite images were collected with the illumination pattern aligned to the apertures of the AFA. A second experiment was conducted with a single attenuating rod (0.5 mm) positioned in the central position of the cuvette, within the chicken breast. In this case, only one composite image was acquired.

When imaging through 1 cm thick chicken breast samples, the majority of the signal was found to be spread across a radius of approximately two or three channels. Consequently, the chicken breast samples were imaged with a sparse illumination pattern to minimize the effect of illumination and detection channel crosstalk. The pattern consisted of illuminating only every second or third channel aperture in each of the *x*- and *y*-directions (i.e. one of 4 channel apertures in a 2 x 2 grid or one of 9 channel apertures in a 3 x 3 grid). Each composite chicken breast image was composed of 64 image acquisitions collected at each of the 2 x 2 or 3 x 3 illumination grid patterns for a total of 256 or 576 image acquisitions per composite image. Each individual image acquisition required approximately 3 seconds whether imaging through 0.5% Intralipid® or 1 cm thick chicken breast. A 2D image collected with an 8 x 8 grid to remove the channel walls required approximately 3 minutes. A reduced illumination using a 2 x 2 grid or a 3 x 3 grid would require approximately 12 or 27 minutes respectively. In addition to the imaging performed with the ADI system, the samples

were also imaged with an SLR camera (Nikon D50, Micro Nikkor f = 55 mm lens) in trans-illumination mode with an LED white light source. Fiducial markers were drawn on both sides of the glass cuvette to provide a rough mapping between the ADI images and the SLR camera images.

3.2.7 Image processing and analysis

Prior to image analysis, the images were first stitched together to form a composite image. For each image, 64 separate images were collected representing the different positions of the angular filter and the illumination pattern. To obtain a composite image, the maximum value across all 64 images was obtained for each pixel and set as the pixel intensity in the corresponding pixel location of the composite image. The same process was used to obtain the composite background image. The composite background image was subtracted from the composite image. The image subtraction procedure generated a final image that was weighted toward detection of quasi-ballistic photons.

When imaging the chicken samples, a composite image was created for each of the 4 or 9 illumination patterns. A binary mask was obtained in the absence of a scattering medium to determine the location of the detection channels that were illuminated for each illumination pattern. The binary masks were then multiplied on a pixel by pixel basis with the composite image for each illumination pattern, and the resulting images were summed to obtain a final composite image.

For the resolution experiment, a central portion of each composite image (0.5 mm x 15 mm) was preselected and averaged on a column by column basis. Each composite image was obtained by scanning the AFA and the illumination source across 64 positions to reduce the artifacts due to shadows cast from the walls of the AFA. The increased sampling rate significantly reduced the shadow artifacts, however, upon close examination, the resulting image still contained several small fluctuations in signal. The fluctuations in signal were likely due to the uneven localization of signal to the center of each channel. This effect did not significantly degrade the quality of the image, but it was greatly amplified when computing the numerical derivative of the edge response function. As a result, the edge

response function obtained from the knife edge experiment was fitted to a logistic function (Eq. 3-1). The range of this function was [*A*, *B*]. *C* represented the growth rate, and *D* represented the position of the inflection point.

$$f(x) = A + \frac{B - A}{1 + e^{-C(x-D)}} \qquad \text{Eq. 3-1}$$

In typical ADI experiments, when a target was imaged, a sharp edge was detected where the wall of the target was expected to be. However, the attenuation due to the object was often not localized completely to the position of the target. Instead, at higher scattering levels, the attenuation signal was blurred [19]. Consequently, at higher scattering levels, a single logistic curve did not model the edge response function well. Instead the edge response function was better modeled using a sum of two logistic curves, one curve describing the edge generated from quasi-ballistic photons, and one curve modeling the background scatter signal. Both of the logistic curves were fitted with the fminsearch function (Matlab). When the knife edge was submerged in 0.4% Intralipid® to 0.55% Intralipid®, a single logistic function was sufficient at describing the edge response function as there was minimal background scatter. When the knife edge was submerged in 0.6% to 0.7% Intralipid®, a dual edge response function was used to fit the edge due to quasi-ballistic photons and the edge due to scattered photons. When the knife was submerged in higher scattering solutions (0.75% Intralipid®), the edge due to quasi-ballistic photons was no longer apparent. As a result a single logistic curve was sufficient at describing the scatter signal.

For each edge generated from quasi-ballistic photons, the center of the logistic curve was fixed during the fitting process to minimize the errors in the fitting process. The parameters A, and B were initially set to the minimum and the maximum of the function respectively and the value D was set to 0.8 as an initial guess. When a single logistic function was fitted to an edge generated at lower scattering levels, the entire field of view of the image was used in the fitting process. When the scatter level was higher and two logistic curves were required to fit the edge spread function, a two-step fitting process was performed. In the first step, the edge related to the quasi-ballistic photon component was fit using a reduced field of view (~3 mm) with prior knowledge of the location of the edge. The fitted result was

then extrapolated to include the entire field of view of the image (15 mm) and the difference between the measured edge response and the fitted result was computed to find the edge response function related to leakage of scattered photons. In the second step, the edge response function related to scattered photons was fit with a logistic curve. However, the parameter related to the center position of the curve was permitted to vary since in the scatter regime, the position of the edge does not normally coincide with the expected position of the knife edge [25]. Also, the initial guess for the growth rate, *C*, was set to 0.04 to reflect the change in slope for an edge related to scattered photons. In the case of the highest scatter cases, where no sharp edge was discernible, the first fitting step was omitted, and only the second fitting step was used.

The theoretical resolution of the system was calculated by computing the line spread function from the fitted edge response function [25]. The line spread function was computed as the derivative of the edge response function (Eq. 3-2). Resolution was computed as the FWHM of the line spread function (Eq. 3-3).

$$f'(x) = \frac{C(B-A)}{1+e^{-C(x-D)}}\left(1-\frac{1}{1+e^{-C(x-D)}}\right) \qquad \text{Eq. 3-2}$$

$$FWHM = \ln\left(\frac{3+\sqrt{8}}{3-\sqrt{8}}\right)/C \qquad \text{Eq. 3-3}$$

When imaging the 4 rods submerged in Intralipid®, two composite images were created in the same manner described above. The first composite image was obtained by illuminating the sample at locations coinciding with the channel apertures, which provided an image weighted by both quasi-ballistic and scattered photons. The second composite image was obtained by illuminating the walls of the AFA, which provided an image weighted toward scattered photons. The two images were subtracted to obtain an estimate of an image related to the quasi-ballistic photon component.

When imaging the chicken breast samples, no further image processing was completed beyond the computation of the composite images.

3.3 Results

3.3.1 Channel crosstalk

Figure 3-3 displays the channel crosstalk for a point source when imaging through chicken breast (Figure 3-3 a&b) and Intralipid® (Figure 3-3 c&d). Figure 3-3a displays an ADI image of a 10 mm chicken breast slab collected when only a single channel was illuminated. Figure 3-3b displays one-dimensional normalized projection profiles of a point source imaged through 6 mm (blue), 8 mm (green), 10 mm (red) chicken. The measured FWHM of the point source was 0.68 mm, 2.1 mm, 3.6 mm for the 6 mm, 8 mm, and 10 mm thick chicken breast samples, respectively. Figure 3-3c displays an ADI image of a point source image through a 0.65% Intralipid®, 1 cm thick sample. Figure 3-3d displays one-dimensional normalized projection profiles of a point sourced imaged through 0.45% (blue), 0.55% (green), 0.65% (red), 0.75% (teal) Intralipid®. The measured FWHM of the point source was constant at approximately 0.35 mm for scattering levels at or below 0.70% Intralipid®. The FWHM of the point source was approximately 0.90 mm for 0.75% Intralipid. The FWHM was measured from the brightest peak of the projection profiles.

The normalized projection profiles displayed in Figure 3-3 b&d were obtained by summing the signal along a 0.2 mm height across the image. The profile was then smoothed with a 0.2 mm wide mean filter and normalized to the maximum intensity.

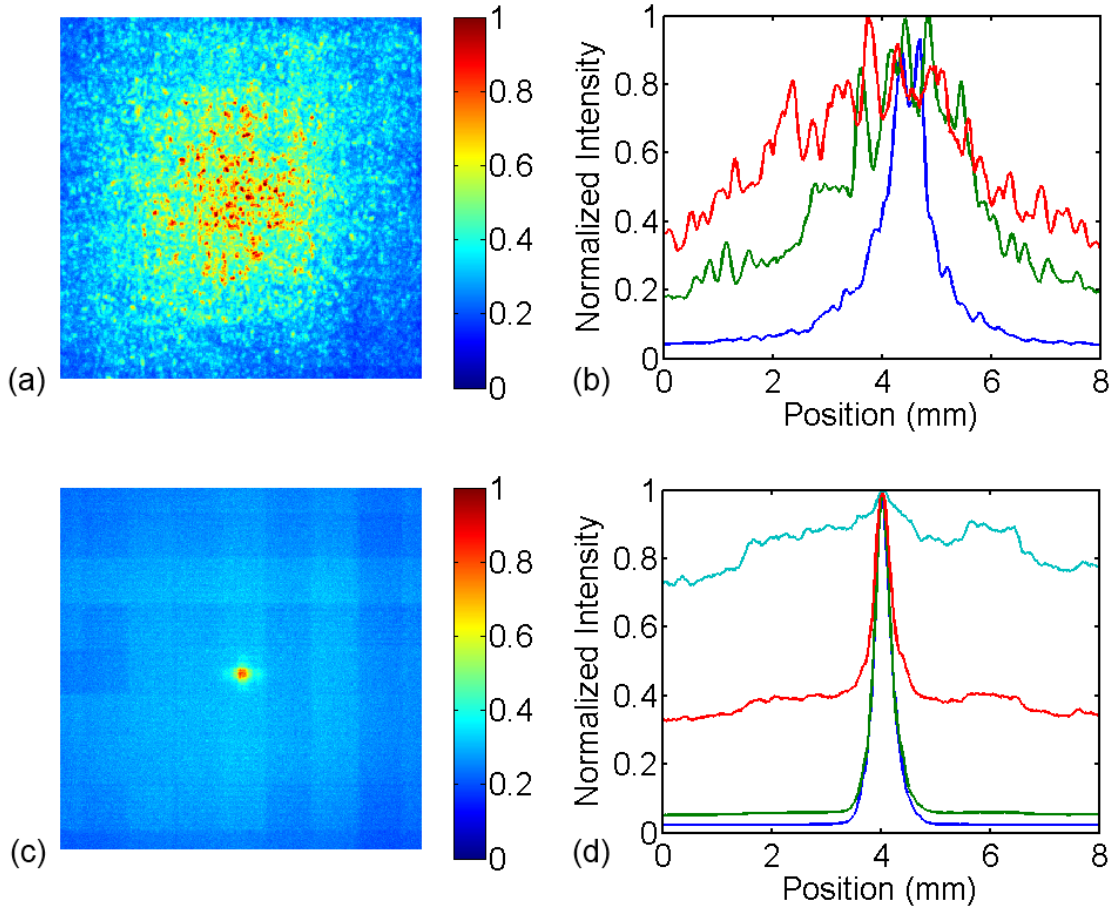

Figure 3-3: Images (a, c) and point spread functions (b, d) of a single illuminated channel in chicken (a, b) and Intralipid® (c, d). (a) Image of a point illumination through 10 mm chicken tissue. FOV = 8 mm x 8 mm (b) Normalized projections of a point illumination through 6 mm (blue), 8 mm (green), 10 mm (red). (c) Image of a point illumination through 0.65% Intralipid®. FOV = 8 mm x 8 mm (d) Normalized projections of a point illumination through 0.45% (blue), 0.55% (green), 0.65% (red), 0.75% (teal) Intralipid®.

3.3.2 Knife edge resolution

Figure 3-4a shows a profile of a typical edge spread function (blue) and the result of the fitting algorithm (red). The edge response function was obtained by averaging a central region (0.5 mm x 15 mm) of the image obtained with a knife edge positioned in a cuvette

filled with 0.65% Intralipid® on a column by column basis. The fitting algorithm (Figure 3-4a red) provided a good approximation of the function that was smooth enough to obtain a derivative, while retaining the shape of the edge response function. Figure 3-4b shows the fitted edge response functions for four Intralipid® concentrations, 0.45% (blue), 0.55% (green), 0.65% (red), 0.75% (teal). In Figure 3-4b the fitted function was plotted with *A* set to 0, and *B* set to 1 to normalize the data across all four Intralipid® concentrations and to remove any offset to the data. The theoretical resolution of the system ranged from 110 µm to 180 µm when the edge due to quasi-ballistic photons was still visible (0.4 – 0.7% Intralipid®). The resolution was insensitive to scatter in this regime. The theoretical resolution of the system was 1.8 mm when the knife was submerged in 0.75% Intralipid®, where the edge due to quasi-ballistic photons was not visible.

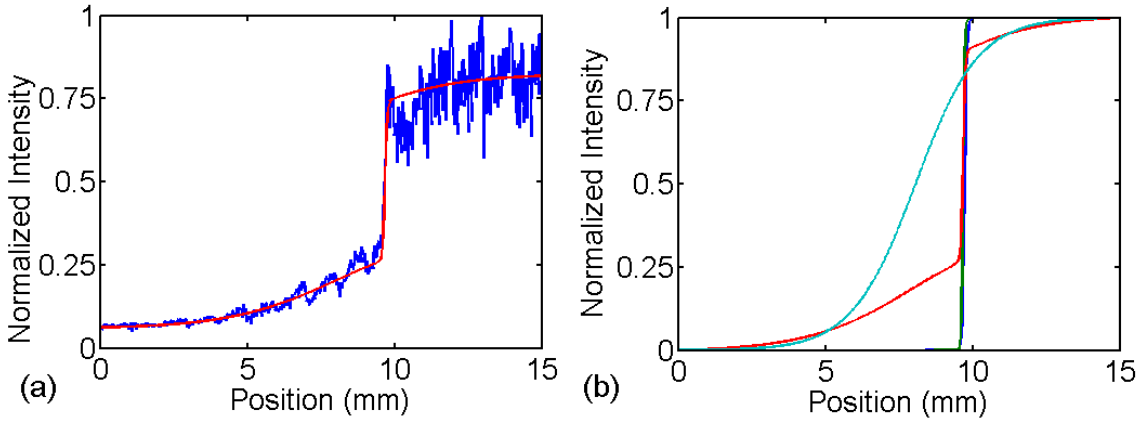

Figure 3-4: Knife edge submerged in Intralipid® (a) 0.65% Intralipid® blue: quasi-ballistic subtraction profile of knife edge averaged from 0.5 mm x 15 mm central region in the image, red: fitted profile using dual logistic function. (b) Fitted edge spread functions for the knife edge submerged in 0.45% (blue), 0.55% (green), 0.65% (red), 0.75% (teal) Intralipid®.

3.3.3 4 rods absorption target

Figure 3-5 shows the attenuation of light from the four absorbing targets positioned in the central position of a 1 cm path length cuvette filled with different scattering media. Figure 3-5 a-c shows the images of the four rods generated from quasi-ballistic photons,

obtained by subtracting the scatter estimation image from the initial image. Figure 3-5 a-c shows the degradation of contrast when the system is imaging below the detection limit (0.6% Intralipid®: Figure 3-5a, Figure 3-5d blue), at the detection limit (0.7% Intralipid®: Figure 3-5, Figure 3-5d red), and beyond the detection limit, (0.75% Intralipid®: Figure 3-5c, Figure 3-5d black). Figure 3-5d displays a one-dimensional profile of the four absorbing targets across the entire field of view of the system. Figure 3-5d was obtained by averaging profiles of a 1 mm height section within the image on a column by column basis. The profiles were further smoothed with a mean filter (130 μm) to improve clarity. As can be seen in the images and the profile plot, the four targets were visible when the targets were submerged in scattering levels at or below the detection limit of 0.70% Intralipid®. The four targets were not visible when submerged in a scattering level beyond the detection limit of 0.70% Intralipid®. The widths of each of the targets were estimated by measuring the FWHM of the absorption peaks in the column by column average of the image. When imaging at 0.6% Intralipid®, the four targets were measured to be 0.35 mm, 0.66 mm, 0.80 mm, 1.0 mm from smallest to largest. When imaging at 0.7% Intralipid®, the four targets were measured to be 0.32 mm, 0.62 mm, 0.84 mm, 1.0 mm from smallest to largest. The targets were not observed at 0.75% Intralipid® and consequently, the widths of the targets were unable to be measured. When imaging at 0.7% Intralipid® or higher, the resulting images displayed both horizontal and vertical banding artifacts.

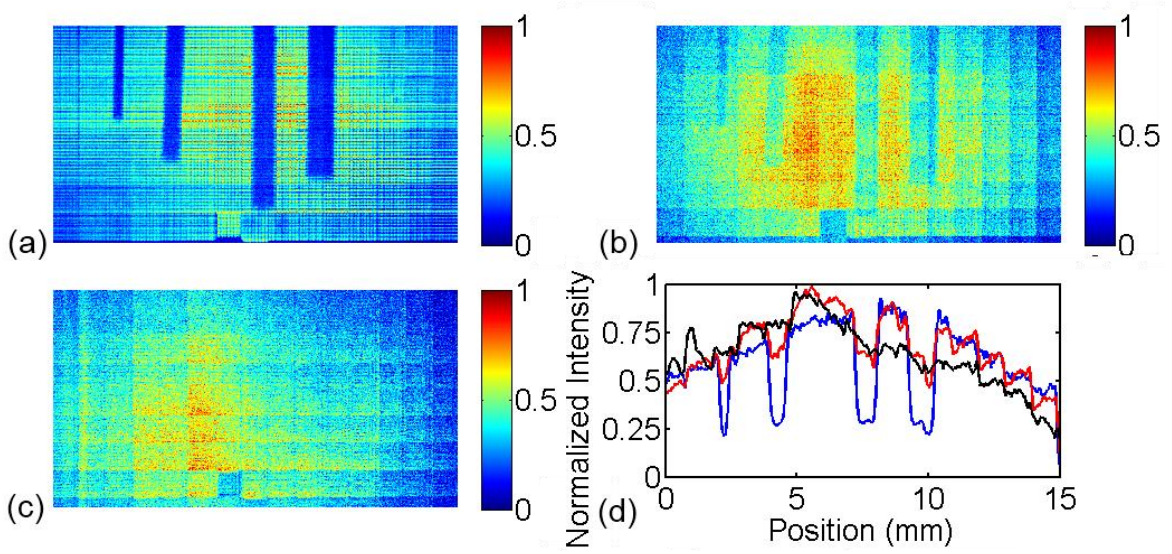

Figure 3-5: 4 rods (0.2, 0.5, 0.7, 0.9 mm) submerged in (a) 0.6%, (b) 0.7%, (c) 0.75% Intralipid®. Images are quasi-ballistic images obtained by subtracting the background estimation image from the original image. (d) One-dimensional profiles obtained by averaging across 1 mm height, blue (0.6%), red (0.7%), black (0.75%). The field of view was 15 mm x 8 mm.

3.3.4 Chicken breast target

Figure 3-6 a&b display ADI images of a series of attenuating rods (0.2 mm & 0.5 mm, 0.9 mm & 0.7 mm diameters respectively, l-r) positioned at the illumination side of a cuvette holding a 1 cm chicken breast slab. Figure 3-6c blue & d blue display the column by column averages of Figure 3-6 a&b respectively. The red line in Figure 3-6 c&d corresponds to the column by column average of the same chicken breast slab, but without the attenuating targets in place. Figure 3-6 e&f show a trans-illumination image of the imaging target collected by illuminating the target with a white LED array and imaging with a SLR camera with the attenuating rods positioned on the detection side of the setup. Figure 3-6 g&h show SLR trans-illumination images with the targets positioned on the illumination side of the target. The 0.5 mm to 0.9 mm targets were clearly visible in the AFA images. The 0.2 mm target was difficult to discern visually in the image (Figure 3-6a left), but was apparent in the column by column average of the image (Figure 3-6c blue). The widths of the rods were estimated by measuring the FWHM of the absorption peaks in the column by column average. The 0.2 mm, 0.5 mm, 0.7 mm, 0.9 mm rods were measured to be 0.42 mm, 0.61 mm, 0.705 mm, and 0.84 mm, respectively.

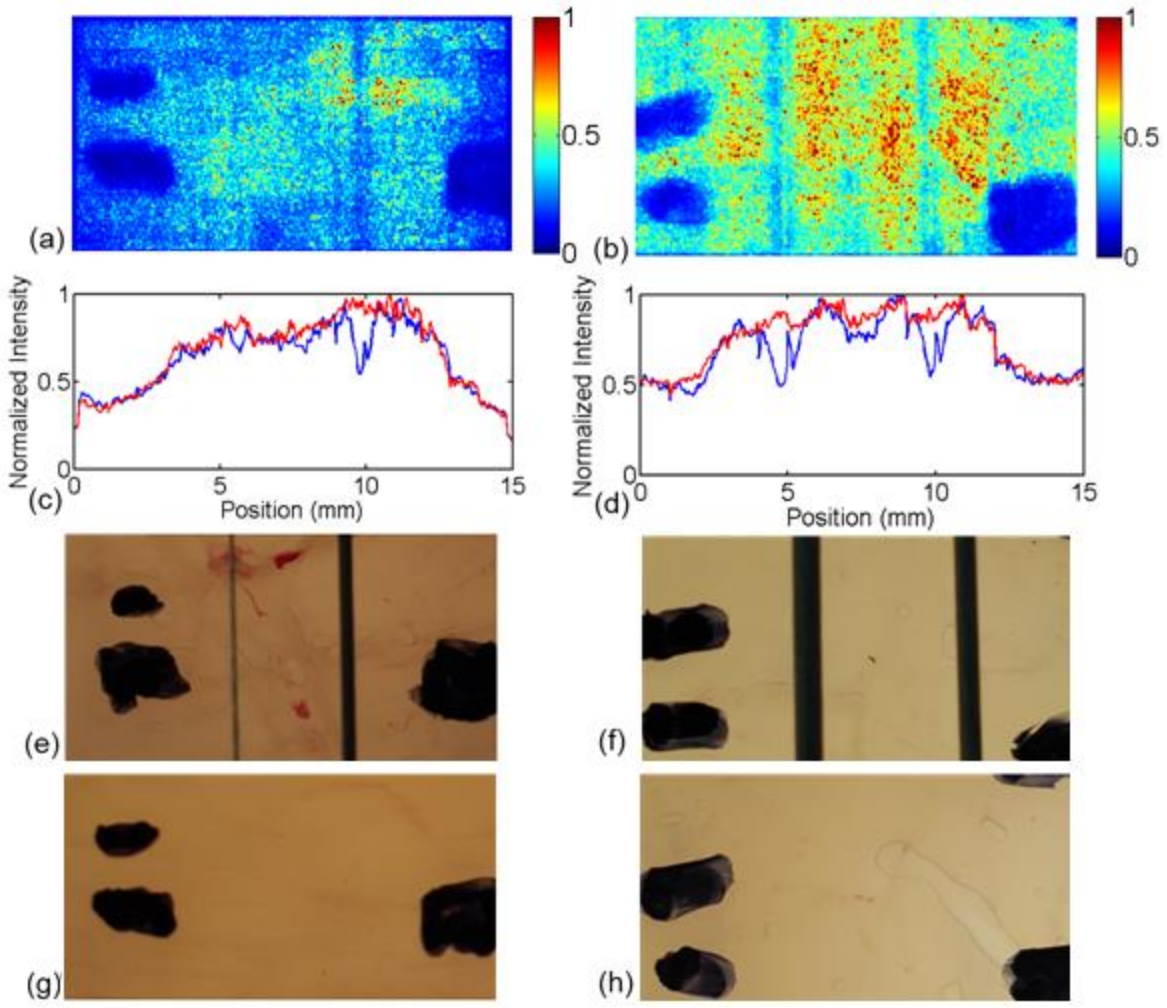

Figure 3-6: 4 rods ((a, c, e, g):0.2, 0.5, (b, d, f, h):0.9, 0.7 mm) positioned at the illumination side of a 1 cm cuvette containing a chicken breast slab. Images (a, b) are quasi-ballistic images obtained by raster scanning a structured illumination pattern. The column by column average (c:blue, d:blue) of (a, b) respectively, and the column by column average of the corresponding breast tissue with the rods removed (c:red, d:red). Trans-illuminated photographs of the imaging target collected from the illumination side (e, f) and from the detection (g, h) side of the target. The field of view was approximately 15 mm x 8 mm.

Figure 3-7a displays an AFA image collected with a 0.5 mm rod positioned in the central depth of a 1 cm chicken breast slab. Figure 3-7c displays a column by column

average of Figure 3-7a. Figure 3-7 b&d show trans-illumination images of the target collected with an SLR camera with the illumination side and the detection side facing the SLR camera, respectively. The 0.5 mm rod was measured to be 0.71 mm wide using the ADI system.

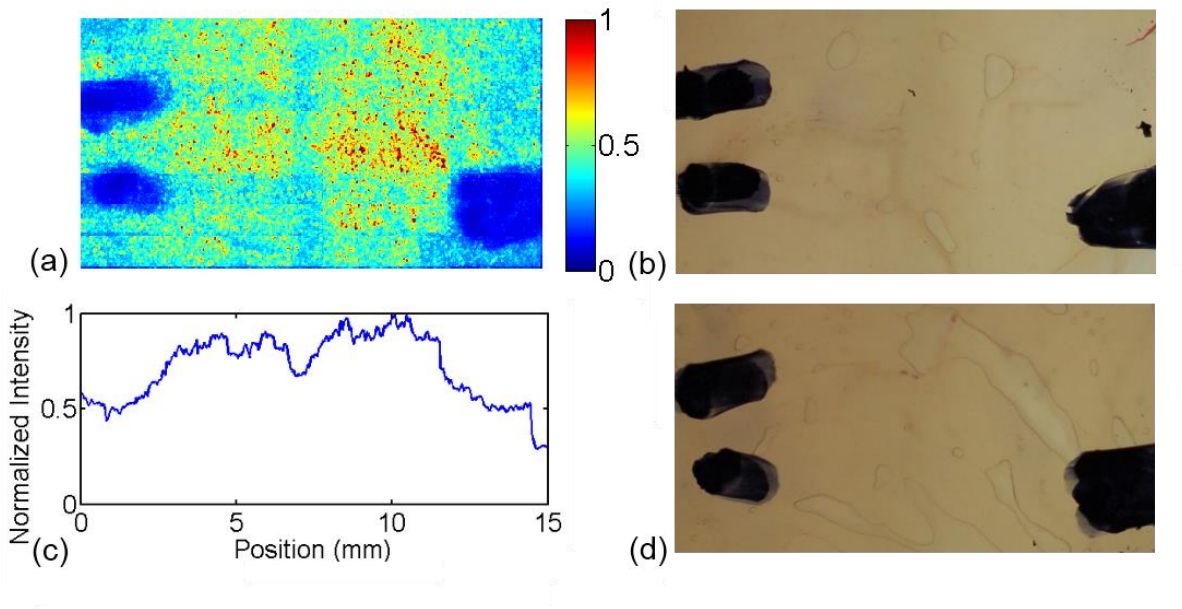

Figure 3-7: 0.5 mm rod positioned at the central depth position of a 1 cm cuvette containing a chicken breast slab. Image (a) is a quasi-ballistic image obtained by raster scanning a structured illumination pattern. (c) Column by column average of (a). Trans-illuminated photographs of the imaging target collected from the illumination side (b) and from the detection (d) side of the target. The field of view was approximately 15 mm x 8 mm.

The AFA images collected (Figure 3-6 a&b, Figure 3-7a) show significant speckle patterns. In addition, a horizontal banding artifact is apparent in Figure 3-7a, and to a lesser extent in Figure 3-6b. The banding artifact consists of two rows of the image approximately 1 mm in height at 2 mm from the bottom and the top of the image. These areas have a lower transmission compared to the surrounding areas.

3.4 Discussion

3.4.1 Channel crosstalk

In AFA-based ADI, two major signal contributions were observed. The first component corresponded to the quasi-ballistic signal, and the second component corresponded to the background scatter. While imaging through Intralipid®, when one channel was illuminated, the majority of the quasi-ballistic signal was localized to the channel which was illuminated (Figure 3-3 c&d). The background scatter signal was found to be relatively uniform in nature. When imaging through chicken breast (Figure 3-3 a&b), the quasi-ballistic signal was found to be spread across a number of channels, while the background scatter signal was not as prominent.

Due to the localization of the quasi-ballistic signal to one channel, an ADI image of an Intralipid® sample can be collected effectively by illuminating all of the channels simultaneously. However, when imaging through a chicken breast sample, the spreading of quasi-ballistic signal suggests that the crosstalk between illumination and detection channels will degrade the image quality. Therefore, when imaging chicken breast samples, a sparse illumination detection scheme may help reduce the crosstalk between channels.

3.4.2 Knife edge resolution

Figure 4a shows the typical edge response for the ADI system when imaging at or near the detection limit of the system. In this regime, the edge response can be described by a combination of two separate edge response functions. The first edge response function is well defined, and confined to a region spanning 100 - 200 μm. The second edge response function is much wider, on the order of 1-2 mm. The dual edge response function observed with the knife edge experiment is consistent with previous contrast and resolution analyses of similar ADI setups. The results support the hypothesis that at scattering levels near the detection limit of the ADI system, two different types of signals can be observed. The first type of signal is from quasi-ballistic light. The quasi-ballistic light has a sharp edge response function that is centered on the expected edge of the knife. The second type of signal is a result of scattered light leaking through the system. The scattered signal has a much wider

edge response function compared to the quasi-ballistic signal. In addition, the center of the scatter edge response function is not located in the same position as the true edge.

The measured theoretical resolution of the system was 110 μm to 180 μm when quasi-ballistic light was still observable (≤ 0.70% Intralipid®). However, this measurement was conducted with the experimental procedure described above, where an 8 x 8 raster scanning system was used to sample the image in areas that would normally be blocked by the channel walls. The raster step size was 125 μm in each direction. As a result, the difference between the finest resolution (110 μm) and the coarsest resolution (180 μm) was not significant. The results suggest that the resolution measurement was limited by the data acquisition protocol. The resolution estimation can be improved by sampling the image at a finer spacing. The resolution estimate agrees to an extent with a previous resolution measurement conducted by the Carson group (230 μm) conducted with a silicon wafer based AFA with a similar acceptance angle [19].

One limitation to the resolution measurement was the lack of an image normalization method to account for the intrinsic differences in signal across the image. One source of position dependent signal intensity is a non-uniform illumination pattern. While the beam was filtered with a spatial filter, and expanded extensively, there was still a gradual change in signal across the entire field of view. A second source of illumination error was present due to edge effects from the illumination pattern. The illumination source was not an extended light source. As a result, the background scatter signal at each channel was position dependent. Channels near the center of the image were exposed to more background scatter signal compared to channels near the edge of the image. The increase in signal near the center of the image will result in an underestimation in the absorption near the center of the image, and an overestimation in the absorption near the edges of the image. While this was not expected to affect the measurement of the quasi-ballistic edge due to its narrow footprint, it was expected to affect the edge due to the background scatter signal, by influencing the position of the edge, as well as the slope of the edge. Both of these effects were observed in the images collected.

3.4.3 4 rods absorption target

At higher scattering levels, the contrast of the rods degraded. This was in part due to the background scatter signal increasing the transmittance where the rods were expected to be positioned. The detection limit of the system as observed in this experiment corresponded to the presence of a quasi-ballistic signal in the knife edge experiments. In the knife edge experiments, a quasi-ballistic edge was observable for the knife edge when the target was placed in scattering levels at or below 0.70% Intralipid®. This limitation corresponded to the highest scattering level at which a 0.2 mm to 0.9 mm diameter attenuating rods could be detected.

The measured widths of the various targets were consistently greater than the actual widths. There was minimal difference in the measured width when imaging at 0.6% and 0.7% Intralipid®, suggesting that resolution may be independent of scattering level for a uniform scattering sample. The width of the smallest target (0.2 mm) was overestimated by 0.2 mm, while the other three targets (0.5 mm, 0.7 mm, 0.9 mm) were all overestimated by 0.1 mm.

In Figure 3-5a, the individual sampling points in the image are observable. At lower scattering levels, much of the signal exiting the AFA is located at the center of the channel. Consequently, each individual sampling point is clearly observable when generating a composite image. When the scattering level is higher, the signal exiting the AFA is more evenly spread across the entire channel. Figure 3-5b and Figure 3-5c do not exhibit the same artifact from the discrete sampling nature of the AFA.

In Figure 3-5 a-c, a defect in the AFA can be observed at the bottom row of the image near the center. This defect was caused by a partial blockage of the channel, and resulted in a discontinuous intensity when compared with the neighboring channels.

A significant horizontal and vertical banding pattern can be observed in the images. When examining the signal generated from one channel (1 mm x 1 mm square within the final image), an uneven distribution of signal was sometimes apparent. In Figure 3-5c, much of the signal is localized to the bottom of each 1 mm x 1 mm block, while in Figure 3-5b

much of the signal was localized to the right of each 1 mm x 1 mm block. This banding pattern was a result of the background subtraction process, and suggested that there may have been a slight misalignment between the DLP shifting and the AFA scanning. This misalignment may have been caused by a mismatch between the resolution of the structured illumination (DLP pixel size with magnification ~40 μm) and the sampling rate of the experiment (125 μm).

3.4.4 Chicken breast target

The smallest attenuation rod (0.2 mm diameter) was difficult to detect visually from the ADI image (Figure 3-6a). The 0.2 mm diameter rod produced the least contrast compared to the other targets. This was evident in the column by column average in Figure 3-6c. The 0.2 mm diameter target may have been obscured by other attenuating structures in the chicken breast. Near the top of the tissue sample (Figure 3-6e, Figure 3-6a), a blood filled structure was visible. At the illumination wavelength (780 nm), some attenuation was expected from blood.

When the attenuating targets were positioned on the illumination side of the cuvette, the resulting ADI images were expected to represent an idealized situation. In a typical imaging situation, a particular target of interest will most likely be embedded deep within the imaging sample. For a deep target, the collimated illumination has scattered before reaching the target. Figure 3-6 shows the contrast of the targets in the idealized case where the attenuating target was illuminated with unscattered light. Figure 3-7 shows a typical imaging case where the light was partially scattered before reaching the contrasting target. Positioning the targets at the illumination side of the cuvette allowed for the easy removal of the target between experiments to acquire a separate image with no target in place. This allowed for a pixel by pixel comparison of the contrast due solely to the target. A second imaging experiment was performed with the 0.5 mm rod embedded in the central depth of the tissue sample to allow comparison between the two target depths. The 0.5 mm target was visible at both depth positions. A small decrease in contrast was observable when the target was positioned in the center of the chicken breast slab. A previous study conducted by the author on ADI contrast and resolution with respect to target depth revealed that resolution and

contrast were both depth independent when the target was not positioned within 2 mm of the detection side of the cuvette [19]. However, this current study differs from the previous study as the illumination pattern and scattering medium are different. A more rigorous analysis will be necessary to obtain a more conclusive relationship between depth and contrast and resolution for a real tissue sample.

When imaging through chicken breast, the measured widths of the smaller targets (0.2 mm and 0.5 mm wide) were overestimated. The measured width of the 0.7 mm target reflected the actual width, while the measured width of the 0.9 mm target was in fact smaller than the actual width. This result disagreed with the previous observation where the widths of the targets were consistently overestimated when imaging through a uniform scattering material. The authors were unable to explain this difference.

The horizontal banding artifacts present in Figure 3-6b and Figure 3-7a are due to the illumination pattern. The field of view of the system is 15 mm x 8 mm. When illuminating with a 3 x 3 scheme, some illumination patterns illuminate 10 (5 x 2) channels at a time, while other illumination patterns illuminate 15 (5 x 3) channels at a time. When illuminating with more channels, the background scatter signal will be higher, and will consequently result in areas of higher intensity in the resulting image.

When the 0.7 mm and 0.9 mm targets were imaged, a small area of attenuation was observable in the area between the two rods. This area of attenuation is characterized by the difference in signal between the target (Figure 3-6d blue) and the blank (Figure 3-6d red) images. This difference in signal is located in the region that was imaged at the same time as the rods, and suggests that there is still a small degree of quasi-ballistic crosstalk between channels even when illuminating with a 3 x 3 scheme. This artifact can potentially be characterized and removed digitally, or prevented by illuminating the sample with a sparser illumination pattern.

In the experiments involving Intralipid® dilutions, a background estimation method was employed to improve the contrast of the images. A second image was acquired with the illumination misaligned with the AFA. This background estimation method was reliant on

the localization of the quasi-ballistic signal to a small area on the AFA (1 channel). When imaging through chicken breast, the quasi-ballistic signal was spread across a number of channels. A background estimation method using a misaligned illumination was not effective for a chicken breast sample as the background image would still contain significant quasi-ballistic signal. Consequently, this step was omitted from the image acquisition protocol.

A 780 nm pulsed light source was utilized for the experiments outlined in this paper. This light source can be replaced with a continuous wave laser with no expected appreciable differences in image quality.

3.5 Conclusions and future work

A two-dimensional angular filter array was constructed for angular domain imaging using three-dimensional printing. A DLP was utilized to generate various illumination patterns for the two-dimensional AFA. The AFA was successfully mounted on a two axis stage to allow for scanning to acquire signal in areas that would normally be obscured by the walls of the channels. The theoretical resolution of the system was measured with varying uniform scattering solutions and a knife edge. The resolution was found to be between 110 µm – 180 µm when imaging within the quasi-ballistic regime of the system (0.70% Intralipid® or below at 1 cm path length). Four attenuating rods of varying sizes from 0.2 mm to 0.9 mm in diameter were detectable when submerged in the central depth position of a 1 cm cuvette filled with Intralipid® dilutions at or below 0.70%. The four attenuating rods were also detectable when positioned at the illumination surface of a 1 cm cuvette containing a 1cm thick chicken breast slab. A 0.5 mm rod was also detectable when positioned in the central depth position of a 1 cm thick chicken breast slab.

The system design can be improved in several ways. The field of view for the system was limited by the area of the DLP chip. A larger DLP chip will provide more flexibility to generate more complex illumination patterns, and allow the imaging of larger tissue samples. The illumination source can be replaced with a multispectral light source to allow for imaging at multiple wavelengths. The DLP chip can also potentially be replaced with a pair of mechanical scanning mirrors to improve the illumination efficiency.

In the future, more rigorous experiments can be conducted to evaluate the performance of the system. A more precise resolution experiment can be conducted with a finer scanning step size. A resolution experiment can be conducted with various non-uniform scattering samples (e.g. breast tissue samples). Also, a more rigorous study can be performed to determine the optimal illumination patterns for various samples.

3.6 Acknowledgements

This project was funded by a Natural Sciences and Engineering Research Council of Canada (NSERC) Discovery Grant to JJLC. EN was funded by a NSERC award (CGS-M), a joint Translational Breast Cancer Research Unit (TBCRU) and Canadian Institute of Health Research (CIHR) Strategic Training Program in Cancer Research and Technology Transfer award, and an SPIE student scholarship. The authors would like to acknowledge Dr. Fartash Vasefi for helpful discussion related to ADI imaging.

3.7 References

1. L. Wang, P. P. Ho, C. Liu, G. Zhang, and R. R. Alfano, "Ballistic 2-d imaging through scattering walls using an ultrafast optical kerr gate," Science **253,** 769-771 (1991).

2. L. Wang, P. P. Ho, and R. R. Alfano, "Time-resolved Fourier spectrum and imaging in highly scattering media," Appl. Opt. **32,** 5043-5048 (1993).

3. L. Wang, P. P. Ho, X. Liang, H. Dai, and R. R. Alfano, "Kerr - Fourier imaging of hidden objects in thick turbid media," Opt. Lett. **18,** 241 (1993).

4. Q. Z. Wang, X. Liang, L. Wang, P. P. Ho, and R. R. Alfano, "Fourier spatial filter acts as a temporal gate for light propagating through a turbid medium," Opt. Lett. **20,** 1498-1500 (1995).

5. V. Prapavat, J. Beuthan, M. Linnarz, O. Minet, J. U. G. Hopf, and G. J. Mueller,"Infrared diaphanoscopy in medicine" in *Proc. SPIE* **2081,** 154-167(1994).

6. G. H. Chapman, M. Trinh, N. Pfeiffer, G. Chu, and D. Lee, "Angular domain imaging of objects within highly scattering media using silicon micromachined collimating arrays," Selected Topics in Quantum Electronics, IEEE Journal of **9,** 257-266 (2003).

7. A. C. Boccara, "Imaging through scattering media," in *Encyclopedia of Modern Optics*, B. D. Guenther, A. Miller, L. Bayvel, and J. E. Midwinter, eds. (Academic Press, 2004), pp. 143.

8. K. Takagi, H. Kakinuma, Y. Kato, and K. Shimizu, "CW transillumination imaging by extracting weakly scattered light from strongly diffused light," Opt. Express **17,** 8332-8342 (2009).

9. K. Takagi, Y. Kato, and K. Shimizu, "Extraction of near-axis scattered light for transillumination imaging," Appl. Opt. **48,** D36-44 (2009).

10. M. S. Tank and G. H. Chapman, "Micromachined silicon collimating detector array to view objects in a highly scattering medium," Can. J. Elect. & Comp. Eng. **25,** 13 (2000).

11. F. Vasefi, M. Najiminaini, E. Ng, B. Kaminska, G. H. Chapman, and J. J. L. Carson, "Angular domain transillumination imaging optimization with an ultrafast gated camera," J. Biomed. Opt. **15,** 061710 (2010).

12. F. Vasefi, M. Najiminaini, E. Ng, A. Chamson-Reig, B. Kaminska, M. Brackstone, and J. J. L. Carson, "Transillumination hyperspectral imaging for histopathological examination of excised tissue," J. Biomed. Opt. **16,** 086014 (2011).

13. F. Vasefi, B. Kaminska, G. H. Chapman, and J. J. L. Carson, "Image contrast enhancement in angular domain optical imaging of turbid media," Opt. Express **16,** 21492-21504 (2008).

14. P. Tsui, G. H. Chapman, R. L. K. Cheng, G. Chiang, N. Pfeiffer, and B. Kaminska,"Spatiofrequency filters for imaging fluorescence in scattering media" in *Proc. SPIE* **7562,** 75620B(2010).

15. P. B. L. Tsui, G. H. Chapman, R. L. K. Cheng, N. Pfeiffer, F. Vasefi, and B. Kaminska,"Spatiofrequency filter in turbid medium enhanced by background scattered light subtraction from a deviated laser source" in *Proc. SPIE* **7175,** 71750A(2009).

16. G. Jarry, S. Ghesquiere, J. M. Maarek, F. Fraysse, S. Debray, Bui-Mong-Hung, and D. Laurent, "Imaging mammalian tissues and organs using laser collimated transillumination," J. Biomed. Eng. **6,** 70-74 (1984).

17. F. Vasefi, B. Kaminska, G. H. Chapman, and J. J. L. Carson,"Angular distribution of quasi-ballistic light measured through turbid media using angular domain optical imaging" in *Proc. SPIE* **7175,** 717509(2009).

18. E. Ng and J. J. L. Carson, "Two dimensional angular domain imaging with 3D printed angular filters," *Appl. Opt.* (2012).

19. E. Ng, F. Vasefi, B. Kaminska, G. H. Chapman, and J. J. L. Carson,"Contrast and resolution analysis of angular domain imaging for iterative optical projection tomography reconstruction" in *Proc. SPIE* **7557,** 755714(2010).

20. G. H. Chapman, J. Rao, T. C. K. Liu, P. K. Y. Chan, F. Vasefi, B. Kaminska, and N. Pfeiffer,"Enhanced angular domain imaging in turbid media using Gaussian line illumination" in *Proc. SPIE* **6084,** 60841D(2006).

21. K. Shimizu and M. Kitama, "Fundamental study on near-axis scattered light and its application to optical computed tomography," Optical Review **7 (5),** 383 (2000).

22. W. F. Cheong, S. A. Prahl, and A. J. Welch, "A review of the optical properties of biological tissues," Quantum Electronics, IEEE Journal of **26,** 2166-2185 (1990).

23. C. K. Chua, K. F. Leong, and C. S. Lim, *Rapid Prototyping: Principles and Applications* (World Scientific, 2010).

24. H. J. van Staveren, C. J. Moes, J. van Marie, S. A. Prahl, and M. J. van Gemert, "Light scattering in Intralipid-10% in the wavelength range of 400-1100 nm," Appl. Opt. **30,** 4507-4514 (1991).

25. J. C. Hebden, "Evaluating the spatial resolution performance of a time-resolved optical imaging system," Med. Phys. **19,** 1081-1087 (1992).

Chapter 4

4 Discussion and future work

This chapter summarizes the dissertation based on the results from the studies that have been described in Chapters 2 and 3. The summary is categorized into two sections: 1) system design and 2) experimental studies. The improvements and limitations of this work are highlighted. Finally, the chapter ends with suggestions for future improvements and a conclusion.

4.1 Summary of work

4.1.1 System design

The ADI systems presented in this thesis represent a significant improvement over previous ADI systems. The first major improvement involves a departure from the previous fabrication technique. MEMS technology is capable of generating highly customizable patterns on silicon wafers. While it is highly proficient at generating two-dimensional structures, it is not ideally suited to generate the three-dimensional structures required to build a two-dimensional angular filter array. 3D printing is an emerging technology that allows for the creation of highly customizable three-dimensional structures in a wide range of materials. Compared to MEMS technology, 3D printing allows for a significantly less expensive prototyping stage as it does not require the construction of lithography masks.

The use of a structured light source represents an improvement over the previous full field illumination setups used in other AFA-based ADI systems. The structured light source allowed for imaging with a restricted light source, which improved image contrast. The structured light source was also easily programmable to allow for imaging over a large area with minimal sample movement. The structured light source can also be used to project various patterns onto the sample and can potentially lower image acquisition times [1]. With a structured light source, the 2D array detector can be replaced with a single pixel detector. A single pixel camera setup reduces the cost of the detector for the system, and may enable

imaging at multiple wavelengths in the near and far infrared that are otherwise inaccessible due to the cost of a 2D detector array at those wavelengths.

4.1.2 Experimental studies

The two studies presented in Chapters 2 and 3 utilize image analysis methods that are widely accepted and highly reproducible. In addition, the analysis allows for the comparison of the AFA-based ADI images with other ADI systems and even other trans-illumination based imaging systems. Chapter 2 utilizes a contrast analysis that builds off a previous study [2]. The use of *a priori* information to determine target and background regions allows for a highly reproducible measurement of contrast. The knife-edge resolution measurement described in Chapter 3 represents a significant improvement over previous attempts to quantify the resolution of an ADI system. Previous ADI resolution studies were based on the detection of small resolution targets [3,4]. This resolution measurement provided a simple estimate of the smallest detectable object. This method of measuring resolution did not fully describe the true resolution for an ADI system.

A typical ADI system captures two sets of photons, one set representative of the quasi-ballistic component, and another set representative of the scattered light. The two groups of photons both contribute to the overall resolution of the system. In the regime where quasi-ballistic photons dominate, the resolution of the system was approximately 150 μm. The resolution of the system was much poorer (1-2 mm) when no quasi-ballistic photons were detected.

4.2 Improvements and limitations

4.2.1 Benefits

The main advantage of the two-dimensional AFA over the one-dimensional AFA is the ability to collect images with minimal scanning. For example, to collect a 2 cm x 2 cm image with a one-dimensional AFA, 200 separate images must be acquired. A two-dimensional AFA with similar dimensions (aperture size 80 μm x 80 μm, 20 μm wall thickness) can collect the same image with a single acquisition. This greatly reduces image

acquisition time, and eliminates the need for raster scanning which can introduce errors due to imperfect positioning and movement artifacts. The 2D AFAs presented in Chapters 2 and 3 do not have the same dimensions as the one-dimensional AFA due to manufacturing equipment availability. However, 3D printing technology capable of feature sizes of <100 µm exist currently, and can be used to create 2D AFAs with comparable aperture size and wall thicknesses as the one-dimensional MEMS-based AFA. The 2D AFA setup presented in Chapters 3 was able to acquire a 15 mm x 8 mm image with 64 image acquisitions. Conceivably, the imaging area can be easily expanded to fill the entire 3 cm x 3 cm AFA by expanding the illumination beam further, and by incorporating a larger CCD. With the previous generation of AFAs, the same 15 mm x 8 mm image would require a minimum of 80 acquisitions. However, the 2D AFA system can easily be improved to acquire larger images conceivably with just 64 acquisitions, while the silicon-based AFA would require even more acquisitions to image a larger sample. The 64 acquisitions needed to obtain a 2D image with the 2D AFA can also be reduced in the future by fabricating AFAs with smaller channel apertures. For example by reducing the channel size and wall size by half, an image can be constructed with 16 acquisitions.

The printing method of the 2D AFA also introduced ridges in the walls in all four channel walls. Patterned walls were only feasible on two of the four walls of each channel in the silicon-based AFA due to manufacturing limitations. A direct comparison for image quality with ridges on four walls compared to two walls was never performed. However one can expect that the improvement will be similar to the improvement observed with two patterned walls compared to smooth walls.

4.2.2 Limitations

One of the major limitations with the two-dimensional angular filters presented in this work was the large dimensions. The aperture size was 500 µm x 500 µm with a wall thickness of 500 µm. The large wall thickness significantly decreased the fill factor of the AFA. Consequently, the AFA was scanned in an 8 x 8 pattern to acquire one image. By decreasing the wall thickness, the number of scanning steps can be reduced. The aperture size is intimately related to the acceptance angle for the AFA. The 2D AFAs presented in this

paper were significantly longer compared to the one-dimensional AFAs in order to maintain the same aspect ratio. By reducing the aperture size, the AFA length can be reduced accordingly. In some applications, a compact and highly portable optical setup is desirable. A shorter AFA length will reduce the overall size of the system.

4.3 Illumination and detection improvements

The angular domain imaging system presented in this dissertation represents a significant advance over previous ADI systems. However, further advancements can be made to improve the system and to optimize the data acquisition process for use as a clinical or commercially available tissue sample imager. This section discusses potential areas of improvement for the ADI system.

4.3.1 Illumination source

The illumination source used in Chapters 2 and 3 consisted of a high powered pulsed diode laser. The pulsed laser source was not optimal for ADI as a pulsed laser source is not required for continuous wave ADI. A comparable CW source such as a fiber coupled diode laser can be obtained at a significantly lower cost, and with improved beam quality and efficiency.

The illumination source was limited to a single wavelength. By imaging a sample with multiple wavelengths, the system will be more sensitive to various endogenous and exogenous sources of contrast. Also, multispectral measurements can be utilized to quantify the concentrations of various local absorbers.

A simple inexpensive multispectral light source can be conceivably constructed by combining several fiber coupled diode lasers. The various lasers can be modulated in intensity to image at different wavelengths, or the image acquisition can be multiplexed to collect multiple images simultaneously. A second approach for multispectral imaging can be performed with the use of a hyperspectral imaging source. A lamp or an LED array can be used as an illumination source. Wavelength discrimination can be performed with various interference filters, or an imaging spectrometer.

The acquisition time of an ADI imaging system is directly related to the power of the illumination source. Acquisition times can be significantly reduced by using a more powerful laser. The highest admissible power for an ADI system is limited to ANSI limits (e.g. skin exposure >0.2W/cm^2 for 400-1400 nm with an exposure time of 10-30000 s) for *in vivo* applications, or limited by tissue damage thresholds for a tissue sample.

4.3.2 Structured light

In Chapter 2, the contrast enhancement obtained by using structured light was first described. The method involved utilizing a matching angular filter positioned in front of the sample to mask out scattered light. In Chapter 3, the method was improved to use a digital light processor to create highly customizable illumination patterns. While the DLP illumination method significantly improved the flexibility of the illumination patterns, it was limited by its resolution. The pixel pitch of the DLP was approximately 10 μm wide. The pattern emitted from the DLP was expanded with a 4x beam expander to increase the imaging area. This resulted in an effective pixel pitch of 40 μm. The AFA was translated in 125 μm increments. As a result, the images acquired suffered from various artifacts due to the mismatch between the DLP illumination patterns and the AFA shifting. This can be improved by utilizing a high resolution DLP chip to improve the effective resolution of the system without sacrificing the total illumination area.

A DLP light source represents a single example of a structured light source. Conceivably various other spatial light modulators can be utilized to improve the imaging capabilities of an ADI system. For example, a liquid crystal spatial light modulator can be used to modify both the phase and the amplitude of a beam of light. A phase modulator can be used to improve the collimation of the light source through wavefront correction, while a liquid crystal amplitude modulator can be used in place of a DLP. Each light structuring method provides its own advantages and disadvantages. With respect to ADI, five characteristics of a spatial light modulator are of interest. These include the spectral response, efficiency, refresh rate, dynamic range and resolution.

A structured light source can also be replaced with a scanning mirror. A galvanometer scanner or a MEMS scanning micromirror can be used to quickly redirect a laser beam. By scanning a collimated light source quickly and modulating the intensity of the light source, a two-dimensional light source can be constructed. A scanning laser can potentially be more efficient compared with a spatial light modulator.

4.3.3 Detection

In Chapters 2 and 3, an electron multiplying charged coupled device (EMCCD) was used to acquire images. The EMCCD allowed for the collection of images in low light situations. The electron multiplying technology allowed for a reliable gain mechanism to create a camera with high sensitivity and low noise. While a high powered laser was utilized as a light source, the AFA significantly reduced the amount of light reaching the detector by rejecting the majority of the scattered photons.

The studies outlined in Chapters 2 and 3 utilized a telecentric lens to image the exit face of the angular filter array. Conceivably, a camera can be bonded to or positioned against the exit face of the AFA and acquire comparable images. In this imaging arrangement, the size of the detection assembly is significantly reduced, allowing for a more compact system. In addition, the reduction of optical components reduces the cost and improves efficiency. Finally, the proposed system will be less sensitive to alignment errors.

4.4 AFA design improvements

The angular filter array discussed in the previous chapters represents an initial prototype of a 2D AFA. Several improvements can be made to optimize the design of the AFA. These improvements are discussed here.

4.4.1 Discontinuous Walls

Due to the layer by layer grid design of the AFA, the walls of the channels were discontinuous. This construction design was chosen as it was highly reproducible and generated AFAs with minimal defects. Defects were characterized by blocked channels, uneven channels, or any other abnormalities. The design was also superior as it mimicked the

patterned walls on the MEMS-based AFA design. The discontinuous walls created lower angles of incidence for glancing photons. It was hypothesized that these discontinuous walls improved the attenuation of low angle photons. However, due to the design, the individual channels within the AFA were not fully enclosed. Thus there was a possibility of channel crosstalk within the AFA itself. For example, a large angle scattered photon could potentially enter the AFA in one channel, and travel through a gap in the channel wall and exit the AFA in a separate channel. Such an event occurring was believed to be unlikely due to the high aspect ratio of the channels, however this effect was never evaluated experimentally or simulated.

An improved AFA design would retain the patterned walls of the current AFA design, while including a full barrier between channels to minimize the possibility of channel crosstalk within the AFA. This design was not feasible with the current FDM printing process as the printer could only produce repeatable results when printing long continuous patterns. Consequently, a series of parallel lines could be printed reliably due to its continuous nature, while a full two-dimensional grid represents a highly discontinuous pattern and would not print successfully. Other rapid prototyping techniques may be more suited to constructing AFAs with complete and patterned walls such as Selective Laser Sintering (SLS) or stereolithography.

4.4.2 AFA size & resolution

Commercially available 3D printers limit the print resolution to maximize print speed, minimize system cost and to maximize the potential build volume. Some 3D printers based on SLS or stereolithography offer the option of a high resolution print mode, where the optical source can be focused further to achieve a smaller area of exposure on the build plane and consequently a higher resolution print. Typically, higher resolution modes either require more time to print or sacrifice the potential build volume. For a FDM-based 3D printer, the resolution of the print is limited by the resolution of the print head positioners and the extruding mechanism. A higher resolution print head positioner will permit the repeatable positioning required for a high resolution print. The resolution of the print head positioners used in the works described in Chapters 2 and 3 was limited to approximately 100 μm. The

second factor affecting resolution for the printer was the extruding mechanism. The thickness of the extruded filament was affected by the speed of the print head and the speed of the extrusion motor. A faster print head speed will stretch out the filament as it is being applied, resulting in a thinner object. A slower extrusion speed will also achieve the same effect. However, at slow extrusion speeds, the extrusion rate is often sensitive to other external factors. Consequently, the extruder was unstable when operating at slow extrusion-speeds. A high resolution print requires a slow extrusion speed and a high positioner speed. The printer used to create the AFAs was unable to produce a high resolution print due to the unreliable printing at slow extrusion speeds. One additional factor affecting resolution was the print head nozzle. The nozzle on the printer was 0.5 mm. The large nozzle size prohibited the reliable printing of objects thinner than 200 μm.

The aspect ratio of an AFA can be altered by changing the size of the channels and by changing the length of the channels. The print volume of the printer used was limited to a build volume of 18 x 27 x 20 cm. Due to the design of the print pattern, the length of the AFA was limited by the height of the build volume, which corresponded to 20 cm. Thus, the aspect ratio of the AFAs described in the previous chapters can be easily increased by printing an AFA up to 20 cm long.

Due to the limitations in the printable patterns and the limitations due to the thinnest printable feature, an FDM printer is not the ideal printer for printing angular filter arrays. A higher aspect ratio AFA can be constructed using stereolithography or SLS. However, photopolymer resins are typically partially translucent to allow for the penetration of the light source through a layer of photopolymer and ultimately bond the new layer to the previous surface. As a result, an appropriate photopolymer must be chosen to ensure absorption at the imaging wavelength. An SLS machine provides the same flexibility in the build geometry as a stereolithography machine. However, like stereolithography, care must be taken to use materials which are absorbing at the wavelength of interest. In addition, care must be taken to select materials which do not create reflective surfaces in order to minimize the internal reflections within the AFA.

4.5 Experimental design improvements

The objective of Chapters 2 and 3 was to characterize the new ADI setup by conducting preliminary experiments to evaluate basic imaging metrics, i.e. contrast and resolution. The approach was to design simple and repeatable experiments which can be used to obtain a direct comparison between the imaging properties of the 2D AFA and the silicon-based AFA. One weakness of the experimental design was the difference between the controlled experiment and a real life imaging application.

4.5.1 Tissue samples

The main application for the ADI system described in this thesis is an optical imager for biological targets. Targets may consist of a slab of excised tissue or a small animal. Compared to the Intralipid®-based phantom imaging experiments presented in the previous chapters, the behavior of a real biological sample is significantly different.

Firstly, a liquid-based Intralipid® sample is primarily homogenous while a biological tissue is a heterogeneous sample. A homogenous sample creates a predictable scattering medium, which can be used to draw various conclusions by conducting a series of experiments at different scattering levels. A heterogeneous sample may have local regions of high scattering and low scattering. As contrast has been shown to be dependent on the level of scattering, the local scattering properties of a heterogeneous tissue must be accounted for in order to obtain quantifiable absorption measurements. Also, scattering level affects optical transmission in ADI. A region of lower scattering may have higher transmission compared to a region of higher scattering. As a result, a system with a higher dynamic range is required to obtain images of a heterogeneous sample without saturating the detector.

In addition, a tissue sample scatters light differently compared to an Intralipid® solution. As outlined in Chapter 3, the degree of scattering anisotropy is different with the two scattering samples and consequently, the scatter rejection of an AFA behaves differently with the two scattering samples. The scattering of a tissue sample can also be affected by the orientation of the tissue, when imaged with polarized light sources, such as the one employed

in the current setup. Periodic structures such as aligned muscle fibers create different optical properties for different polarization orientations due to birefringence [5].

One final complication of a biological tissue sample is the surface of the sample. A liquid phantom conforms to the shape of the container. When an optical cuvette is used to hold the liquid, the container/sample interface is flat. However, when a tissue sample is imaged, this is often not the case. In Chapter 3, a chicken breast slab was positioned within a custom designed cuvette and imaged with the ADI setup. In the optical trans-illumination images obtained by illuminating with an LED light source and imaging with an SLR camera, it was evident that even with a small compression in the tissue sample, the surface of the tissue did not completely conform to the shape of the cuvette. Instead, small air pockets were visible. An uneven surface will contribute to various artifacts in an image. Refraction at the tissue surface will change the trajectory of the photon. This effect would be more apparent with a small animal, as a small animal is expected to have a more uneven surface. The artifacts due to an uneven surface can be mitigated to an extent by submerging the sample in an index matching fluid that mimics the optical properties of the biological sample. The scattering and absorption of the index matching fluid can be adjusted to prevent saturation in the image due to varying object thicknesses.

4.5.2 Attenuating targets

Another weakness to the experimental imaging targets presented in this thesis was the sources of contrast in the images. In Chapter 2, the ADI images were obtained with a graphite rod as a source of contrast. Chapter 3 utilized a series of graphite rods and a metal rod as sources of contrast. The motivation of utilizing graphite and metal rods was the attenuating properties of the targets. The targets were expected to be completely attenuating at the imaging wavelength. The targets represented the best case imaging scenario as the contrast of a completely attenuating target was expected to be the highest obtainable contrast. However, biological imaging targets rarely have completely attenuating structures embedded within the sample. In most cases, the sources of contrast in a biological sample will be partially attenuating. As a result, the contrast measurements conducted in this thesis represent idealized situations, and do not reflect contrasts attainable in a biological sample. One

method of testing a partially absorbing target is to use a tube filled with a partially attenuating target (e.g. India Ink, fluorescent targets) as a source of contrast. The attenuation of the target can be varied by changing the concentration of the liquid. Alternatively, a solid phantom can be constructed with several inclusions with different optical properties [6].

4.6 Applications

The main advantage of the ADI system described in this thesis is its inexpensive cost compared to other imaging methods. The system is also simple and requires minimal adjustments during operation. The system is also stable and robust, enabling heavy usage. The nature of the system allows for the low cost imaging of various biological samples that were previously not feasible with other optical imaging methods. Therefore, the system has the potential to be used for a variety of applications. The two most common applications, small animal imaging and tissue sample imaging will be discussed here.

4.6.1 Small animal imaging

Small animal imaging is an important application for optical imaging that is currently being explored. Many biological studies rely on optical biomarkers to track disease models or biological activity within a small animal. Current commercially available optical small animal imagers often do not account for tissue scatter. Consequently, the resulting images often suffer from poor resolution, and are often qualitative in nature. An AFA-based ADI imaging system has the potential to improve resolution, and potentially provide quantitative images. The non-destructive nature of ADI also permits for longitudinal studies, an advantage compared to other optical scatter reduction methods such as optical clearing. ADI has also been demonstrated by the author to successfully reconstruct 3D tomographic images, allowing for more comprehensive imaging of small animals less than 6 mm thick [7].

4.6.2 Tissue sample imaging

Several attempts are currently being made to develop a fast optical imaging system for tissue samples. In breast conserving surgery, a surgeon’s objective is to remove tumorous tissue, while leaving the healthy tissue intact. Currently, a histopathological analysis is

conducted on resected tissue samples to determine if a surgery is successful, or if a second surgery is required to remove more tissue. The time scale of the analysis is longer than the surgery, and is conducted after the initial surgery is completed. An ADI system has the potential to evaluate tissue margins quickly during the surgery. The objective of a tissue sample ADI system is to provide a thorough and objective analysis of a resected tissue sample while the surgery is still in progress. This will provide the surgeon with enough information to decide if another resection is required or if the surgery is successful. This will reduce the need for subsequent surgeries and the associated risks and complications.

4.7 Conclusions

Through the duration of this dissertation, a novel approach to angular filter array based angular domain imaging was developed. The technique implemented a two-dimensional angular filter array, which permitted the acquisition of two-dimensional optical projections of scattering samples with minimal scanning.

In Chapter 2, an initial contrast study was conducted to select the optimal angular filter dimensions for imaging. A second study was conducted to improve the image contrast through the use of a structured illumination. The structured illumination was then used to obtain a scatter estimation of the system by illuminating the sample with a misaligned patterned illumination. The scatter estimation image was used to improve the contrast of the ADI images.

In Chapter 3, the imaging system was improved to obtain images devoid of AFA wall shadows through the use of scanning. In addition, an improved structured illumination system (Digital Light Processor) was included to increase the flexibility in the illumination patterns. A rigorous resolution analysis was then conducted to measure the resolution of the system when imaging various scattering samples. The resolution analysis was then confirmed by imaging objects of varying sizes. Finally, a biological sample was imaged and an absorbing target was resolved.

This technology can potentially be used for a variety of applications. Its low cost and simplicity make it accessible. The most obvious applications currently involve small animal imaging and tissue sample imaging.

4.8 References

1. M. F. Duarte, M. A. Davenport, D. Takhar, J. N. Laska, Ting Sun, K. F. Kelly, and R. G. Baraniuk, "Single-Pixel Imaging via Compressive Sampling," Signal Processing Magazine, IEEE **25,** 83-91 (2008).

2. E. Ng, F. Vasefi, B. Kaminska, G. H. Chapman, and J. J. L. Carson, "Contrast and resolution analysis of iterative angular domain optical projection tomography," Opt.Express **18,** 19444-19455 (2010).

3. F. Vasefi, B. Kaminska, G. H. Chapman, and J. J. L. Carson, "Image contrast enhancement in angular domain optical imaging of turbid media," Opt. Express **16,** 21492-21504 (2008).

4. F. Vasefi, B. Kaminska, P. K. Chan, and G. H. Chapman, "Multi-spectral angular domain optical imaging in biological tissues using diode laser sources," Opt. Express **16,** 14456-14468 (2008).

5. V. Tuchin, *Tissue Optics: Light Scattering Methods and Instruments for Medical Diagnosis* (SPIE, 2007).

6. F. Vasefi, M. Najiminaini, E. Ng, A. Chamson-Reig, B. Kaminska, M. Brackstone, and J. J. L. Carson, "Transillumination hyperspectral imaging for histopathological examination of excised tissue," J. Biomed. Opt. **16,** 086014 (2011).

7. E. Ng, F. Vasefi, M. Roumeliotis, B. Kaminska, and J. J. L. Carson,"Three-dimensional angular domain optical projection tomography" in *Proc. SPIE* **7897,** 78970V(2011).

Appendix A

A Three dimensional angular domain optical projection tomography

This appendix contains the manuscript that was published in March 2011, according to the conference standards established for Photonics West, organized by SPIE in San Francisco, USA. Brief citation as follows: Ng, E., Vasefi, F., Kaminska, B., Carson, J. J. L., "Three dimensional angular domain optical projection tomography," SPIE Annual Meeting, Symposium on Biomedical Optics (BiOS) 7897-0V, 2011.

Appendix A describes the instrumentation of a three-dimensional angular domain imaging scanner. Here a one-dimensional angular filter array is used to collect a multitude of projections at different projection angles in order to reconstruct a tomographic slice of the target. The object was then scanned to collect a three-dimensional rendering of the object via stacking two-dimensional slices. A custom three-dimensional resolution target was constructed and submerged in a scattering medium. Results suggested that the system was capable of resolving the target at a scattering level of 0.5% Intralipid® at 1 cm optical path length.

A.1 INTRODUCTION

A.1.1 Trans-illumination imaging

In optical trans-illumination imaging, there are several types of photons, which can be collected to generate an image. Ballistic photons traverse an imaging target with straight trajectories and are either transmitted or attenuated. Ballistic photons are the most informative, generating images with high contrast. However, very few photons maintain their ballistic trajectory in tissue samples greater than 1-2 mm in thickness [1]. Quasi-ballistic photons undergo several scattering events when traversing a sample, but they retain their forward trajectory. Quasi-ballistic photons are less informative than ballistic photons as their trajectories are less direct. Yet, as quasi-ballistic photons maintain their forward trajectory, they are still able to generate projection images representative of the imaging target.

Scattered photons have undergone several scattering events and have a near isotropic angular distribution. These photons contain minimal information regarding the imaging target. For thick samples (>2 mm tissue), the high population of quasi-ballistic photons compared to ballistic photons enables decreased image acquisition time, at the expense of a slight degradation in image quality. Several imaging methods attempt to distinguish between quasi-ballistic and scattered photons, e.g. time domain, frequency domain and angular domain, but system cost, speed and efficiency remain significant hurdles to overcome.

A.1.2 Angular domain imaging

Angular domain imaging distinguishes between (quasi-) ballistic, and scattered photons by the direction of the photon exiting an imaging target. Ballistic photons have not undergone any scattering events and lie on the axis of illumination. Quasi-ballistic photons have undergone few scattering events and exit the imaging target with a slight deviation in their trajectory compared to the axis of illumination. Scattered photons tend to experience large deviations in trajectory and exit the imaging target at large angles with respect to the axis of illumination. In angular domain imaging, an angular filter is employed to distinguish between the informative ballistic and quasi-ballistic photons and the non-informative scattered photons. In addition to being non-informative, scattered photons are often image degrading as they decrease image contrast.

One method of angular domain imaging utilizes an Angular Filter Array (AFA) (Figure A-1a), an array of micro-channels (typical channel size 80 μm x 80 μm x 2 cm, 200 channels / array) bulk micro-machined from silicon, precisely aligned to a collimated source of illumination [2, 3]. Ballistic and quasi-ballistic photons pass freely through the channels, while scattered photons collide with the walls of the channels and are attenuated. In the literature, AFAs are characterized by their approximate acceptance angles, which are calculated directly from their geometry, under the assumption that the channel walls are perfect attenuators [4]. For a channel with dimensions of 80 μm x 80 μm x 2 cm, the acceptance angle is approximately < 0.32º, for a photon travelling between opposite corners. For a channel with smooth walls, the effective acceptance angle of the channels is expected to be higher than the geometric calculation as the photons may undergo up to three reflection

events [5]. These reflections have been minimized in a newer reflection-trapped AFA design (Figure A-1), which incorporates periodic ridges on the walls with an amplitude of 2.5 μm. Ridge patterns minimize internal reflections within the micro-channels and constrain the effective acceptance angle to the geometrical limit. The ridge pattern is only present on the side walls of the channel and not on the top and bottom surfaces of each channel due to limitations during fabrication [5].

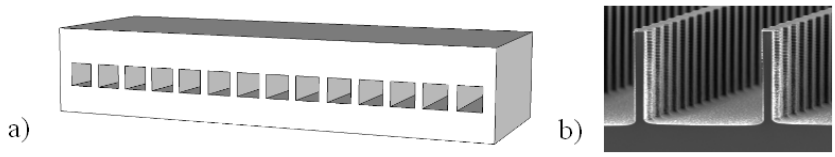

Figure A-1 a) Cartoon of AFA: 80 μm x 80 μm x 2 cm, 200 elements. Channel count and dimensions are not to scale. b) SEM image (top removed) of a reflection-trapped AFA.

A.1.3 Angular domain optical projection tomography

Angular domain imaging collects projection images of a target. Each channel in the image approximates a line integral of optical attenuation for the ray path normal to the channel location. It has been previously demonstrated that by collecting angular domain images at regular angular intervals, a two-dimensional transverse slice can be reconstructed with either filtered back-projection or iterative reconstruction algorithms [6,7]. A comprehensive analysis of the spatial dependence of contrast and resolution revealed that contrast was dependent on the depth of the object, while resolution was generally position independent. Large changes in resolution were observed when the target was positioned behind a defective channel.

A.2 Experimental Setup and methods

A.2.4 Illumination and detection

Figure A-2 displays a schematic of the setup used for experiments. A CW diode laser (Thorlabs 808 nm) was used as an illumination source. The beam was collimated vertically with an aspheric lens, which also focused the beam in the horizontal direction. The beam

passed through a 1-mm pinhole to restrict the vertical size of the beam and to improve collimation. The beam was then expanded and collimated with a pair of cylindrical lenses (f = -6 mm, f = 100 mm). The collimated line of light was then passed through a cuvette (Starnacells 93/G/10, 1 cm path length) holding an imaging target. Detection was performed with an AFA with 200 parallel channels, each 80 µm x 80 µm x 2 cm, positioned in front of a linear 16-bit CCD camera (Mightex TCE-1304-U). The AFA was positioned on a 6 degree of freedom jig to ensure proper alignment with the incident beam and the camera.

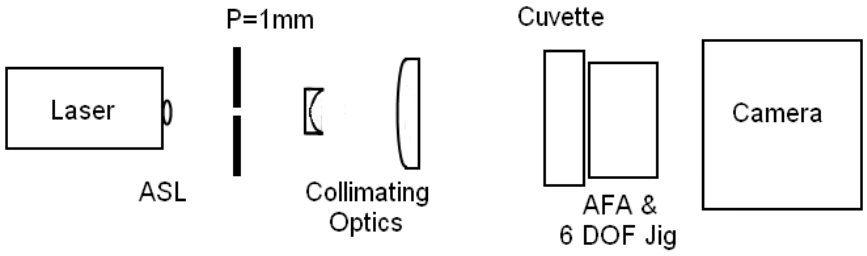

Figure A-2: Experimental Setup. Laser: Thorlabs 808 nm diode laser, ASL: Aspheric Lens, P: Pinhole, Collimating Optics: f = -6 mm, f = 100 mm cylindrical lens, Cuvette: 1 cm path length, AFA: element size 80 µm x 80 µm x 2 cm, 200 elements, Camera: Mightex TCE-1304-U.

A.2.5 Imaging target

A custom three dimensional imaging target (Figure A-3) was designed to test the system's ability to reconstruct circular objects of varying size. The target consisted of four truncated cones suspended from four cylinders. The cylinders had a diameter of 2 mm and a height of 3 mm, while the truncated cones varied from a diameter of 200 µm to 2 mm over a height of 13.5 mm (Figure A-3b). The cone/cylinder structures were evenly spaced around a circle of diameter 5 mm (Figure A-3a). The structure was constructed with PolyJet™ (Objet Geometries Ltd.) three dimensional printing, which builds a three dimensional object by successively layering and curing a UV curing photopolymer with a layer thickness of 28 µm. The imaging target was suspended from a SCARA robot (Epson E2C351), which translated the target to the center of the cuvette, rotated the target to collect projections at varying

angles for tomographic imaging, and translated the object vertically to obtain tomographic projections at different vertical positions.

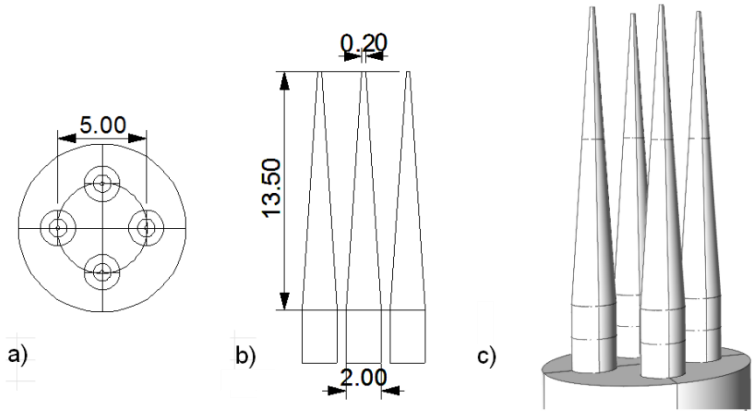

Figure A-3: Imaging target, 4 truncated cones & cylinders. a) top view, b) side view, c) three dimensional rendering. All measurements are in millimeters.

The imaging target was suspended in a cuvette filled with a 0.5% Intralipid® solution, diluted from 20% Intralipid® stock solution with deionized water. Intralipid® is a fat emulsion commonly used as a uniform scattering medium for optical imaging experiments [8,9]. One hundred and fifty (150) slices were collected at a slice thickness of 80 μm corresponding to the height of the AFA. For each slice, 60 projections at 6° intervals covering 360° were collected. Image acquisition started ~1 mm below the tips of the cones and extended ~11 mm toward the cylinders.

A.2.6 Image pre-processing

The walls of the AFA cast shadows on the camera, resulting in an image with large periodic drops in signal (Figure A-4a: red). The amount of quasi-ballistic and ballistic light passing through each channel was approximated to be proportional to the signal from the central 7 pixels (56 μm @ 8 μm pixel width) of each channel (Figure A-4a: blue). This pre-processing step reduced the size of each one dimensional projection from 1250 pixels to 95 pixels, greatly reducing the computation time for the following reconstructions. In addition to reducing the size of the dataset, each projection was corrected for defective channels. Defective channels were individually identified before the experiment and removed digitally

by replacing the signal in each defective channel (Figure A-4a: blue, dashed) with the mean signal from the two adjacent channels. Finally, a blank image was collected with the scattering medium and no attenuation target in the field of view. The blank image was first pre-processed with the same procedure as the three-dimensional tomographic projection data. The projection data was then normalized to the blank image by using a pixel by pixel division to convert the projections to transmission values. The negative of the natural logarithm of the transmission values were then calculated to obtain absorption values. Figure A-4a displays the raw signal and pre-processing steps for a 0.5 mm graphite rod suspended in a 1 cm path length cuvette filled with a 0.5% Intralipid® dilution positioned 5 mm from the AFA side of the cuvette (reduced field of view, ~2 mm). Figure A-4b displays an absorption profile for Figure A-4a, with the field of view expanded to cover the entire imaging area (~1 cm). Figure A-4c displays an absorption profile for the imaging target at slice #25, corresponding to a slice ~1.2 mm from the cone tips. The expected diameter for a target at this height was ~360 µm.

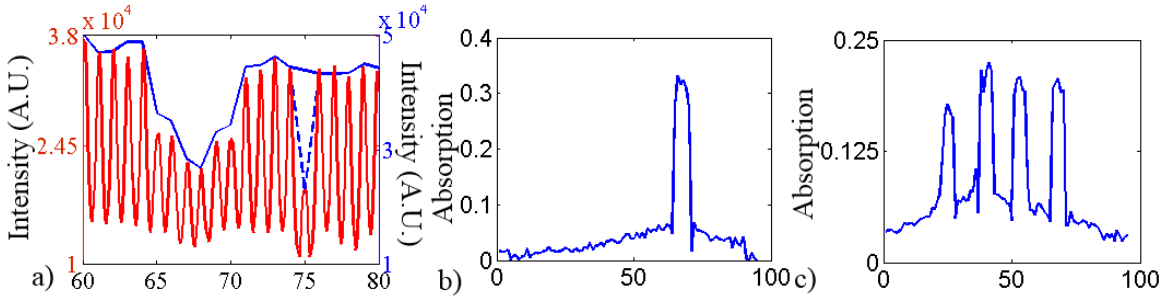

Figure A-4: a) Projection of a 0.5 mm graphite rod placed in the center of a 1 cm path length cuvette, submerged in 0.5% Intralipid®. Red: raw camera signal. Blue dashed: Signal re-binning. Blue: Defective channel removed by averaging signal from neighboring channels. FOV ~2 mm. b) Projection of graphite rod in (a) displayed in absorption units. FOV ~1 cm. c) Sample projection of imaging target, slice #25, ~1.2 mm from cone tips. Target diameter ~360 µm.

A.2.7 Tomographic reconstruction

Tomographic reconstruction was performed with two different reconstruction algorithms. The first algorithm was a filtered backprojection method (Ram-Lak filter), while

the second algorithm was an iterative truncated pseudoinverse method. The iterative method incorporated both a forward model and a backward model into the reconstruction.

The forward model was generated by measuring the system response of a point attenuator positioned within every position in the imaging plane while suspended in a 0.5% Intralipid® dilution at 1 cm path length. A 0.5 mm diameter graphite rod was used as an approximate point attenuator, and imaged at 100 μm steps to measure the system response at 91 x 91 positions within the 1 cm x 1 cm imaging plane. The system response was then pre-processed using the method described above. This system response matrix would then be used as a lookup table for generating sinograms.

For every position (Cartesian grid, 100 μm spacing) in the reconstruction field of view (circle, 1 cm diameter), a sinogram was compiled. For a given starting position (x, y) in the system response grid, a rotation transformation was applied to find the new position of the point attenuator (x', y') after a rotation step (6°, 60 steps). The system response matrix was then used to find an experimental projection, which most closely corresponded to a projection of a point attenuator at the new rotated position (x', y'). Successive projections were stacked to build up a sinogram. This resulted in a tomographic system matrix.

In the backward model, the truncated pseudoinverse of the tomographic system matrix was computed. In the absence of noise, our reconstruction problem can be represented by Eq. A-1, where *g* represents the measured information, *H* represents the tomographic system matrix, and *f* is the unknown object being measured.

$$g = Hf \qquad \text{Eq. A-1}$$

Given *g*, one method of solving for *f*, involves inverting the system matrix, *H*. The tomographic system matrix was used to compute the truncated pseudoinverse. First, the singular value decomposition (Eq. A-2) was computed to reveal the left, *U*, and right, V^T singular vectors and their corresponding singular values, *S*. *S* has the form **diag**($\sigma_1, \ldots, \sigma_n$).

$$H = USV^T \qquad \text{Eq. A-2}$$

From this decomposition, the truncated pseudoinverse was calculated (Eq. A-3). In a typical imaging system, noise is often represented in the singular vectors corresponding to the smallest singular values. In an effort to suppress reconstruction noise, the singular vectors corresponding to noise were omitted from the inversion process by regularization [10]. The pseudoinverse was approximated using the first k (100) singular vectors in *S* from a total of 5700 singular vectors. The rank of the pseudoinverse, *k*, was selected to maximize noise suppression, while maintaining image reconstruction fidelity.

$$H_k^{+} \cong V S_k^{+} U^T \text{ where } S_k^{+} = diag(\sigma_1^{-1},...,\sigma_k^{-1},0,...,0) \qquad \text{Eq. A-3}$$

The iterative algorithm was implemented as follows. (i) The initial estimate of *f* was set to zero attenuation. (ii) The estimate of *f* was forward projected with *H* to obtain an estimate of *g*. (iii) The difference between the estimate of *g* and the experimental projection data was computed. (iv) The difference was backprojected with the truncated pseudoinverse H_k^{+} and added to the image estimate *f*. (v) The updated image estimate was thresholded to limit the absorption values to positive values as it was assumed that no light sources were present in the reconstruction plane. Steps ii to v were then repeated 10 times. Reconstructions were performed on a slice by slice basis and the reconstructed slices were stacked to obtain a three dimensional representation of the embedded target. All data processing and image reconstruction was performed in Matlab®.

A.3 Results and discussion

A.3.8 Projection data

Figure A-5 displays the sinograms collected for two separate slices of the imaging target. Figure A-5a corresponds to a slice ~1.2 mm from the cone tips, where the cross sectional diameter was approximately 360 μm. Figure A-5b corresponds to a slice ~9.2 mm from the cone tips, where the cross sectional diameter was approximately 1.4 mm. The sinogram collected with the smaller target has much greater contrast than the sinogram collected with larger targets. With larger targets, a significant amount of attenuation was observed in regions that were not expected to contain an absorbing target, thereby decreasing image contrast. The presence of the background signal suggested that the method for

background normalization and the attenuation calculation may not have been fully appropriate for large or highly attenuating targets.

The sinograms displayed in Figure A-5 reveal one potential source of image reconstruction artifacts. During the tomographic image acquisition process, the four cones were rotated. At several projection angles, the attenuating targets were expected to overlap, and the attenuation measured by the detector was expected to be a summation of the attenuations of each target. However, in both sinograms displayed in Figure A-5, it was evident that the measured attenuation was not additive for overlapping targets. This effect was due to the highly attenuating nature of the target. The attenuation for one cone was already beyond the dynamic range of the system, and as a result, the system was unable to detect the presence of overlapping cones.

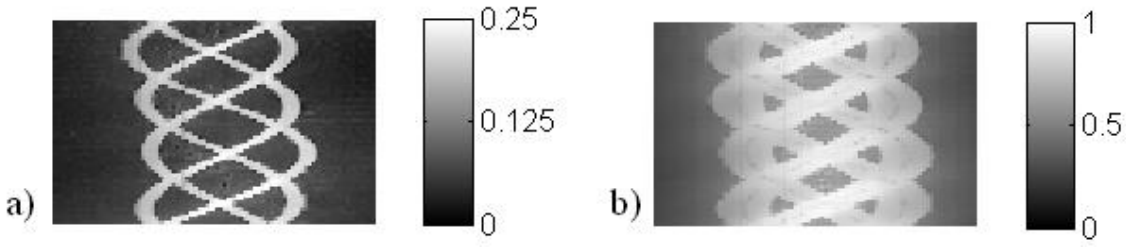

Figure A-5: Sinograms of the imaging target suspended in 0.5% Intralipid® dilution, 60 projections. Field of view is ~1 cm. a) Slice #25 ~1.2 mm from cone tips, target diameter: ~360 μm b) slice #125 ~9.2 mm from cone tips, target diameter: ~1.4 mm.

A.3.9 Slice reconstructions

Figure A-6 displays image reconstructions for the two sinograms displayed in Figure A-5. Figure A-6a displays a reconstruction of the cones where the cross sectional diameter was expected to be ~360 μm using the filtered backprojection reconstruction method, while Figure A-6b displays the reconstruction of the same data using the iterative technique. Figure A-6c and Figure A-6d display the reconstruction of the cones where the cross sectional diameter was expected to be 1.4 mm using filtered backprojection and iterative reconstruction methods, respectively. The iterative reconstruction method reconstructed the smaller targets with minimal background signal, while the filtered backprojection

reconstruction image suffered from streaking artifacts. When reconstructing larger targets, the filtered backprojection method yielded similar streaking artifacts. The iterative method reconstructed an image with a smoother background signal. This signal was expected during the reconstruction as the sinogram displayed a similar background attenuation. Figure A-6c also displays a significant attenuation signal in the shape of a ring located in the center of the reconstructed image. This ring was not observed in the smaller attenuation target (Figure A-6a), and was not expected to be present in the reconstruction.

In general, the shape of the targets in the filtered backprojection reconstruction method appeared to be more consistent with the expected circular shape. However, the distribution of attenuation was irregular for different sized objects. With the smaller targets, the majority of the attenuation signal appeared to lie within the central pixel in the target, while with larger targets, the majority of the attenuation signal was present around the edges of the target. The iterative method reconstructed irregularly shaped objects with a more homogeneous distribution of signal across each object. The irregular shape may have been a result of the regularization procedure, where singular vectors with correspondingly small singular values were omitted during reconstruction. Compared to a single pseudoinverse multiplication, the iterative method was more successful at reconstructing smaller objects (data not shown). In addition, the iterative algorithm provided a means to incorporate *a priori* information via the inclusion of specific constraints on the intermediate reconstruction images e.g. image thresholding. The iterative reconstructions were limited to 10 iterations. This limit was chosen as it represented a good compromise between image quality improvement and reconstruction speed.

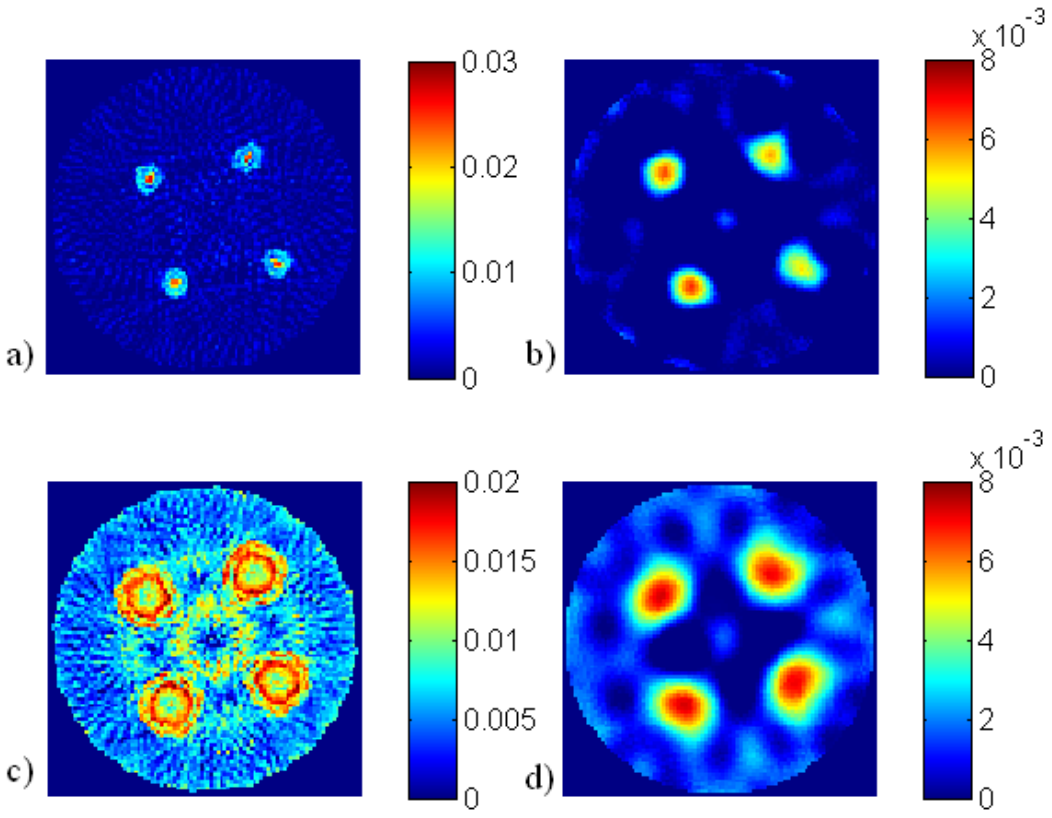

Figure A-6: 2D reconstructions of the 4 cone imaging target suspended in 0.5% Intralipid® dilution at 2 axial slices. a & b) Slice #25 ~1.2 mm from cone tips with filtered backprojection and iterative reconstruction methods, respectively. c & d) slice #125 ~9.2 mm from cone tips, reconstructed with filtered backprojection and iterative reconstruction methods, respectively.

A.3.10 3D image representation

Figure A-7 displays a three dimensional representation of the cone targets using filtered back projection (Figure A-7a) and iterative reconstruction (Figure A-7b). The figure depicts three slices, one axial (z) slice through all four attenuating targets, and two slices each intersecting two cone targets over the length of the cone. The filtered backprojection method was able to reconstruct signals from the smaller targets more successfully compared to the iterative method. The iterative method overestimated the size of the attenuating targets

when the targets were small. For larger targets, ~1 mm, there was little difference between the size of the reconstructed objects with different reconstruction algorithms.

The inability of the iterative method to reconstruct smaller targets with good fidelity may be a result of the choice of point attenuator used to collect the system matrix. As the system matrix was measured with a 0.5 mm diameter absorption target, the signal from the absorption target extended beyond several pixels. Consequently, the pseudoinverse was expected to cause blurring. This effect may potentially be mitigated in the iterative algorithm by introducing a sharpening filter between iterations or using a smaller attenuator to perform the calibration scan.

In general, the iterative reconstructions yielded smoother images with less background noise compared to the reconstructions with filtered backprojection. Also, the reconstructed attenuation signal was more evenly distributed across the entire absorption target when reconstructed with the iterative method, compared to the irregular distributions in the filtered backprojection reconstructions. As a result, 3D ADI images of sparse targets reconstructed with iterative methods are likely easier to segment compared to the filtered backprojection reconstructed images.

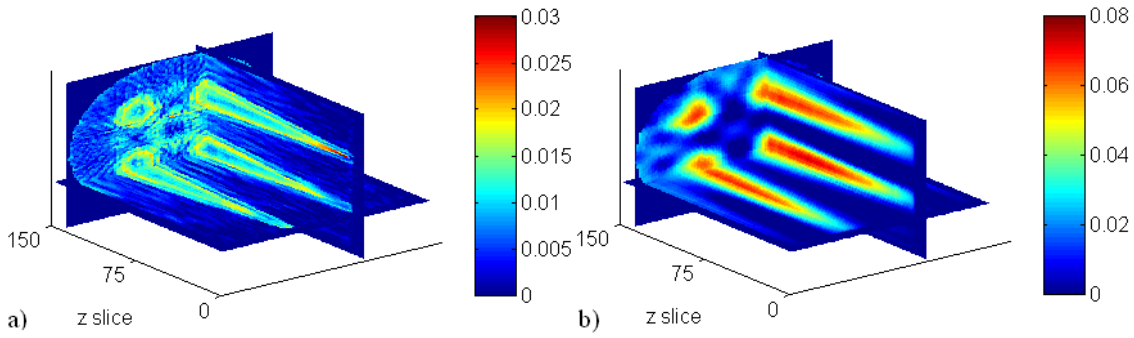

Figure A-7: 3D reconstruction of the 4 cones imaging target using a) filtered backprojection and b) iterative reconstruction. The field of view for each slice is ~1 cm x 1 cm.

A.4 Conclusions and future work

Three dimensional ADI images were collected of a custom designed resolution target submerged in a 0.5% Intralipid® dilution at 1 cm optical path length. The resolution target consisted of four truncated cones and was used to evaluate the ability of the imaging system and reconstruction algorithm to reconstruct objects of different cross sectional sizes. Images were reconstructed with a filtered backprojection method and an iterative reconstruction method. The iterative reconstruction method used a calibration scan conducted with a 0.5 mm diameter graphite rod for the forward model, while the backward model was constructed by using a truncated pseudoinverse of the forward model. The truncated pseudoinverse minimized reconstruction noise, while maintaining reconstruction fidelity.

The filtered backprojection method was more successful at reconstructing the shape of the circular cross section of the cones. However, the filtered backprojection reconstructions suffered from a noisy background caused by streaking artifacts, and the reconstructed attenuation signal was irregularly distributed around the reconstructed object. The iterative reconstruction method yielded reconstructions with a smooth background, with the attenuation signal evenly distributed across the reconstructed object. However, the iterative method was unable to reconstruct the circular cross section of the cones, likely due to the loss of information in the pseudoinverse from regularization. Also, the iterative method was unable to localize the attenuation signal from the smaller targets, resulting in an overestimation in the size of the reconstructed objects.

In the future, the iterative algorithm could be easily extended to incorporate reconstruction constraints to improve the quality of the reconstructed images and the rate of convergence. In addition, 3D images can be collected at several wavelengths to incorporate spectral information.

A.5 Acknowledgements

This project was funded by grants from the Natural Sciences and Engineering Research Council (NSERC) and the Canadian Foundation for Innovation (CFI) to J. J. L. Carson and B. Kaminska. E. Ng was supported by a Natural Sciences and Engineering Research Council of Canada CGS-M scholarship. F. Vasefi and M. Roumeliotis were supported by a scholarship from the Translational Breast Cancer Research Unit at the London Health Sciences Centre. M. Roumeliotis was also supported by a Canadian Institutes for Health Research (CIHR) Strategic Training Program in cancer research in technology transfer scholarship.

A.6 References

[1] Boccara, A. C., "Imaging through scattering media," (2004). [Encyclopedia of modern optics], (Academic Press, 2004)

[2] Chapman, G. H., Trinh, M., Pfeiffer, N., Chu, G. and Lee, D., "Angular domain imaging of objects within highly scattering media using silicon micromachined collimating arrays," Selected Topics in Quantum Electronics, IEEE Journal of 9(2), 257-266 (2003).

[3] Vasefi, F., Kaminska, B., Chapman, G. H. and Carson, J. J. L., "Angular distribution of quasi-ballistic light measured through turbid media using angular domain optical imaging," Proc. SPIE 717509 (2009).

[4] Vasefi, F., Hung, B. S. L., Kaminska, B., Chapman, G. H. and Carson, J. J. L., "Angular domain optical imaging of turbid media using enhanced micro-tunnel filter arrays," Proc. SPIE 73691N (2009).

[5] Vasefi, F., Najiminaini, M., Ng, E., Kaminska, B., Chapman, G. H. and Carson, J. J. L., "Angular domain transillumination imaging optimization with an ultrafast gated camera," J. Biomed. Opt. 15(6), 061710 (2010).

[6] Ng, E., Vasefi, F., Kaminska, B., Chapman, G. H. and Carson, J. J. L., "Contrast and resolution analysis of iterative angular domain optical projection tomography," Opt. Express 18(19), 19444-19455 (2010).

[7] Vasefi, F., Ng, E., Kaminska, B., Chapman, G. H., Jordan, K. and Carson, J. J. L., "Transmission and fluorescence angular domain optical projection tomography of turbid media," Appl. Opt. 48(33), 6448-6457 (2009).

[8] Michels, R., Foschum, F. and Kienle, A., "Optical properties of fat emulsions," Opt. Express 16(8), 5907-5925 (2008).

[9] Flock, S. T., Jacques, S. L., Wilson, B. C., Star, W. M. and van Gemert, M. J., "Optical properties of Intralipid: a phantom medium for light propagation studies," Lasers Surg. Med. 12(5), 510-519 (1992).

[10] Hansen, P. C., "The truncated *SVD* as a method for regularization," BIT Numerical Mathematics 27(4), 534-553 (1987).

Appendix B

B Multispectral angular domain imaging with a tunable pulsed laser

This appendix contains the manuscript that was published in March 2012, according to the conference standards established for Photonics West, organized by SPIE in San Francisco, USA. Brief citation as follows: Ng, E., Vasefi, F., Carson, J. J. L., "Multispectral angular domain imaging with a tunable pulsed laser," SPIE Annual Meeting, Symposium on Biomedical Optics (BiOS) 8225-2C, 2012.

Appendix B describes the instrumentation and the analysis of a multispectral angular domain imaging system constructed with a tunable pulsed laser light source. Here a one dimensional angular filter array is used to collect multiple one dimensional projection images at different wavelengths of an attenuating target submerged in a scattering medium. The contrast and resolution was measured as a function of imaging wavelength. Results suggested that a tunable pulsed laser light source was a suitable source for multispectral angular domain imaging.

B.1 INTRODUCTION

B.1.1 Trans-illumination optical imaging

In optical trans-illumination imaging, a sample is imaged with a beam of light, and the transmission through the sample is measured. When light traverses a biological sample, it is subject to scattering and absorption events. Scattering processes degrade image quality by reducing the contrast and resolution of an absorbing target. As a result, trans-illumination images of biological samples are often limited by the thickness and the scattering level of the sample. In trans-illumination imaging, the paths of the photons are used to categorize the photon type. Ballistic photons traverse a sample with straight trajectories. They are the most informative; however, very few ballistic photons survive when traversing samples greater than 1-2 mm in thickness [1]. Quasi-ballistic photons undergo several scattering events as they traverse a sample, but they retain their forward trajectory. Due to their non-direct paths,

quasi-ballistic photons are not as informative as ballistic photons; however, they are still able to generate projection images representative of the sample. When imaging through thick scattering samples (5-10 reduced mean free paths), there are significantly more quasi-ballistic photons than ballistic photons. Consequently, an image formed from quasi-ballistic photons can be generated significantly faster than an image formed from purely ballistic photons and with only a slight degradation in image quality. The tradeoff between image quality and acquisition time is often desirable for several imaging applications. Scattered photons undergo many scattering events as they traverse a sample. They do not necessarily retain their forward trajectory, and therefore do not provide high quality projection images of objects within the sample. In addition to containing minimal information, scattered photons can potentially scatter around absorbing targets and reduce image quality and contrast. Several trans-illumination imaging techniques such as frequency domain [2], time gated [3] and angular domain [4] attempt to distinguish between the informative quasi-ballistic photons and the non-informative scattered photons to generate optical shadowgrams that faithfully represent the objects inside the sample.

B.1.2 Angular domain imaging

Angular domain imaging discriminates between the different types of photons by the angle at which the photon exits the sample. Ballistic photons have not undergone any scattering events, and can be found on the axis of illumination. Quasi-ballistic photons have undergone a few forward scattering events and can be found near the axis of illumination. Scattered photons have undergone several large angle scattering events. Consequently, scattered photons can be found at large angles with respect to the axis of illumination.

One implementation of angular domain imaging utilizes an Angular Filter Array (AFA) (Figure B-1a) [5-10], an array of micro-channels etched into a silicon wafer. When the AFA is precisely aligned with the axis of illumination, ballistic and quasi-ballistic photons can pass freely through the channels, while scattered photons tend to strike the walls of the channels and attenuate. A typical AFA has 200 channels, each with a cross section of 80 μm x 80 μm and a length of 2 cm. The angular acceptance of the angular filter can be calculated geometrically from the aspect ratio. The angular acceptance for the 80 μm x 80

μm x 2 cm array was computed to be < 0.32°. In an attempt to reduce internal reflections, 2.5 μm ridges were fabricated into the channels (Figure B-1b) [8], which provided a means for reflection trapping.

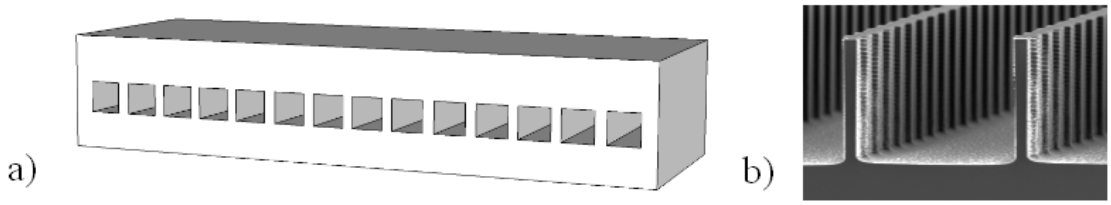

Figure B-1: a) Schematic of an AFA (channel count and dimensions not to scale). b) SEM image (top removed) of a reflection-trapped AFA.

B.1.3 Multispectral angular domain imaging

The angular filter array approach to angular domain imaging is advantageous compared to a traditional lens-pinhole angular filter as the AFA is a lens-less angular filter. Consequently, the AFA is not susceptible to the chromatic aberrations of lenses, and can theoretically provide a more uniform angular acceptance across a wide range of wavelengths. Multispectral AFA-based angular domain imaging has been previously demonstrated with multiple laser diodes at 670 nm, 808 nm, and 975 nm [7], where 520 μm resolution targets embedded in 5 mm chicken breast samples were successfully imaged. Hyperspectral AFA-based angular domain imaging has been previously conducted with a halogen lamp [11], where Intralipid®-based phantoms with embedded Indocyanine green (ICG) inclusions were imaged with an AFA and an imaging spectrometer. Tumor and muscle tissue samples from a mouse were successfully identified with the use of transmission spectra. Angular domain imaging is expected to perform better with a laser compared with a lamp, as a lamp cannot be collimated to the same degree as a laser. For example, a collimated light source has been shown to provide superior resolution for a trans-illumination imaging system when compared with a non-collimated light source [12]. The diode-based multispectral imaging system presented in ref [7] was spectrally discrete due to the availability of laser diodes. In addition, the diode-based approach required the re-collimation of the light source whenever a new

diode was introduced. We hypothesized that a multispectral imaging system based on a laser-pumped Optical Parametric Oscillator (OPO) would provide the collimation advantages of a laser, and a tunable source of light with a spectral resolution suitable for hyperspectral imaging. Also, previous AFA imaging systems utilized NIR light to interrogate imaging samples. The laser-pumped OPO used in this paper was tunable across most of the visible spectrum.

B.2 Experimental setup and methods

B.2.1 Illumination and detection

Figure B-2 displays a schematic of the OPO-based angular domain imaging system. An OPO (SLOPO, Continuum) pumped with the third harmonic (355 nm) of an Nd:YAG laser (Surelite II, Continuum) was used as a tunable pulsed laser light source. The laser produced two output beams, a signal beam (tunable within the range of 400 nm to 700 nm) and an idler beam (tunable within the range of 720 nm to 2650 nm) with a pulse width of 5 ns at 20 Hz. The output from the signal beam was used in these experiments. The output beam from the laser was spectrally filtered to remove the residual 355 nm light. The power output from the laser was adjusted with a series of neutral density filters to prevent oversaturation of the CCD. The signal detected by the CCD was dependent on both the wavelength of the illumination beam as well as the scattering level of the phantom. The laser light was then collimated with two lenses (f = 125 mm, f = 150 mm). The collimated beam then passed through a cuvette (Starnacells 93/G/10, 1 cm path length) containing the target. The light exiting the cuvette was filtered with an AFA, 200 channels, 80 μm x 80 μm x 2 cm and collected with a 16-bit linear CCD (Mightex TCE-1304-U). The AFA was placed on a 6 degree of freedom jig to precisely align the AFA with the axis of illumination. Images were collected at 13 wavelengths at 20 nm increments between 460 nm and 700 nm.

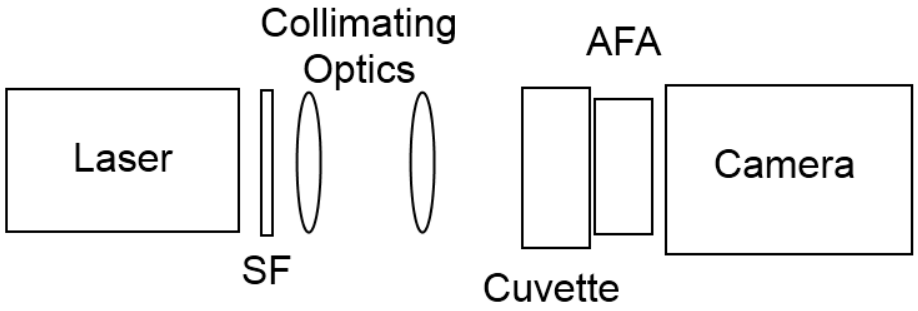

Figure B-2: Experimental Setup. Laser: Continuum Surelite OPO, SF: Spectral Filter, Collimating Optics: f = 125 mm, f = 150 mm, Cuvette: 1 cm path length, AFA: element size 80 µm x 80 µm x 2 cm, 200 elements, Camera: Mightex TCE-1304-U.

B.2.2 Imaging target

A cylindrical absorbing target (0.7 mm diameter graphite rod) was positioned in the center of a 1 x 5 x 5 cm cuvette perpendicular to the axis of the camera. The graphite rod was assumed to provide complete absorption at all test wavelengths between 460 nm and 700 nm. Hence, the graphite rod enabled the evaluation of the contrast of the imaging system at a wide range of wavelengths. The cuvette was filled with varying concentrations of Intralipid® diluted from a 20% Intralipid® stock solution to create phantoms with various scattering levels. Four concentrations of Intralipid® (0.15%, 0.2%, 0.25% and 0.3%) were used. Intralipid® is a lipid emulsion that serves as a convenient scattering medium for optical experiments [13].

B.2.3 Image pre-processing

For each of the four Intralipid® dilutions and each of the 13 illumination wavelengths, a series of one-dimensional images were collected, first with the absorbing target in place (1000 images), then with the absorbing target removed (1000 images). The images were then normalized in absolute intensity to reduce the effect of pulse to pulse power variations. The power corrected images were then averaged to improve the signal to noise ratio. The walls of the AFA casted shadows on the detector, which resulted in large periodic drops in the signal (Figure B-3a blue). The quasi-ballistic signal was approximated to be proportional to the

signal from the central 7 pixels (56 μm @ 8 μm pixel width) of each channel (Figure B-3a black). The blue line in Figure B-3a shows the raw signal for a 0.7 mm absorbing rod embedded in a 0.25% Intralipid® dilution imaged at 640 nm. The black line in Figure B-3a shows the quasi-ballistic signal computed from the raw signal. The red line in Figure B-3a shows the quasi-ballistic signal for the image collected with no absorbing target in place. The image with the target submerged in the scattering medium was normalized to the blank image with no absorbing target in the scattering medium with a pixel by pixel division to obtain the transmission due to the presence of the absorbing rod. The negative logarithm of the transmission was then computed to obtain absorption values. Figure B-3b shows the absorption calculated for the 0.7 mm absorbing rod in Figure B-3a (0.25% Intralipid® at 640 nm).

Contrast was computed from the absorption profile by evaluating the absorption at the target and the absorption at a predetermined background region. The background region consisted of a similarly sized area adjacent to the target position. In typical AFA-based angular domain imaging, the attenuation signal from an absorbing target is not perfectly localized to the target position [10]. This is due to the imperfect nature of the angular filtration. A typical AFA is unable to distinguish between quasi-ballistic photons and scattered photons that have an exit angle near the axis of illumination. As a result, the signal observed by the camera is a combination of the quasi-ballistic signal, and a background scatter signal. The presence of an absorbing target affects the quasi-ballistic signal at the target location, and also affects the background scatter signal nearby the target. Contrast (Eq. B-1) was computed as the normalized difference between the transmission observed at the target location and the transmission due to the background scatter signal.

$$Contrast = \frac{I_{object} - I_{background}}{I_{object} + I_{background}} \qquad \text{Eq. B-1}$$

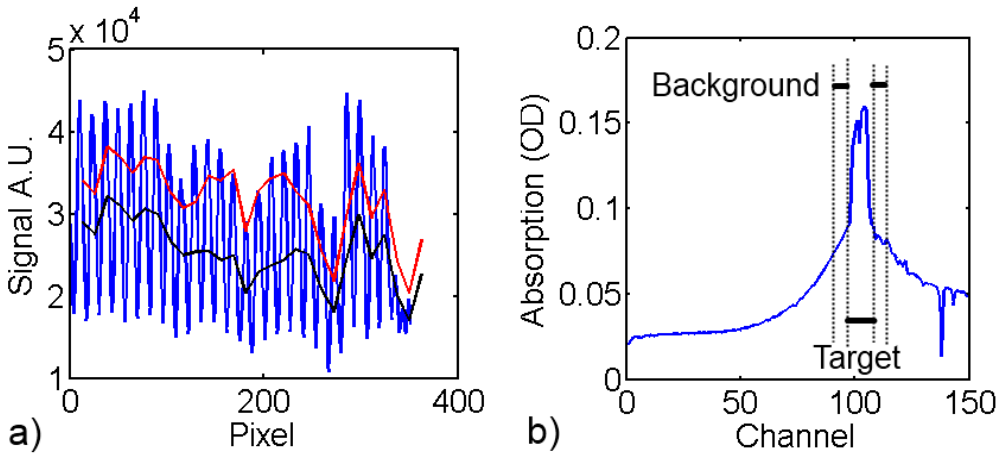

Figure B-3: a) Projection of a 0.7 mm graphite rod placed in the center of a 1 cm path length cuvette, submerged in 0.25% Intralipid®; blue: raw camera signal; black: Signal re-binning; red: Signal with no absorbing target. FOV ~2mm. b) Projection of graphite rod in (a) displayed in absorption units. FOV ~1.5cm.

B.3 Results and discussion

Figure B-4a displays the contrast of the 0.7 mm target as a function of wavelength at four different Intralipid® dilutions. The blue curve displays the contrast for the 0.15% Intralipid® dilution, the green curve shows the contrast for the 0.2% Intralipid® dilution, the red curve shows the contrast for the 0.25% Intralipid® dilution, and the teal curve shows the contrast for the 0.3% Intralipid® dilution. Generally, contrast at a particular scattering level increased with increasing wavelength. Contrast also decreased with increasing scattering level. Contrast ranged from 0.07-1 for the 0.15% Intralipid® target, 0.04-0.98 for the 0.2% Intralipid® target, 0.02-0.55 for the 0.25% Intralipid® target and 0.02-0.16 for the 0.3% Intralipid® target.

Figure B-4b-d displays the absorption measured at various wavelengths for the 0.7 mm absorbing target submerged in a 0.2% (b) 0.25% (c) and 0.3% (d) Intralipid® dilution. The blue curve shows the absorption at 480 nm; green 520 nm; red 560 nm; teal 600 nm; purple 640 nm; gold 680 nm. Contrast improved with increasing wavelength for two reasons. First, at longer wavelengths, the measured absorption at the target location was higher.

Second, the background absorption signal was lower at longer wavelengths. The target was clearly visible at wavelengths greater than 500 nm for the 0.15% Intralipid® phantom; 540 nm for the 0.2% Intralipid® phantom; 600 nm for the 0.25% Intralipid® phantom and 660 nm for the 0.3% Intralipid® phantom. The target was clearly visible when the absorption profile had a discernible increase in absorption at the target location that corresponded to the absorption of quasi-ballistic photons. This occurred when the contrast was found to be greater than 0.10.

An increase in contrast at longer wavelengths was expected for our angular domain imaging system as the scattering coefficient and the anisotropy of the scatter distribution of Intralipid® are both wavelength dependent. The reduced scattering coefficient for Intralipid® is known to decrease at longer wavelengths, which is consistent with the increase in contrast that was observed at longer wavelengths in our experiments. The results suggested that the dynamic range of an AFA-based angular domain imaging system is highly dependent on the scattering level of the imaging target.

Large decreases in absorption can be seen at a few channel locations in the absorption images. These sharp decreases in absorption typically span one channel, and are a result of defects in the AFA manufacturing process. A partially blocked channel will be insensitive to the changes in attenuation due to the presence of the absorbing rod. These blocked channels can be accounted for with digital signal processing, or by collecting a secondary image with the angular filter array shifted from its original position. The two images can then be stitched together digitally to remove artifacts due to blocked micro-channels. This correction procedure was not performed in the experiments presented in this paper. The laser-pumped optical parametric oscillator served as a tunable source of illumination with the spectral resolution needed to perform hyperspectral imaging. One drawback from the laser source was the pulse to pulse variations in power due to the non-linear nature of the OPO wavelength conversion. The inconsistent power output necessitated the normalization of the images to account for the power variations. In addition the pulse to pulse variations in power, the spatial distribution of the light varied between pulses. To compensate for this deficiency, a large number of images were obtained and averaged for each scattering level and

wavelength to minimize the variations in beam intensity. Finally, the beam profile was found to be wavelength dependent; the spatial distribution of the output light was not consistent across different wavelengths. Consequently, transmission images must be used to compare images collected at different wavelengths instead of raw projection images. Computed transmission images account for the wavelength dependent beam profile, whereas raw projection images do not account for this variation.

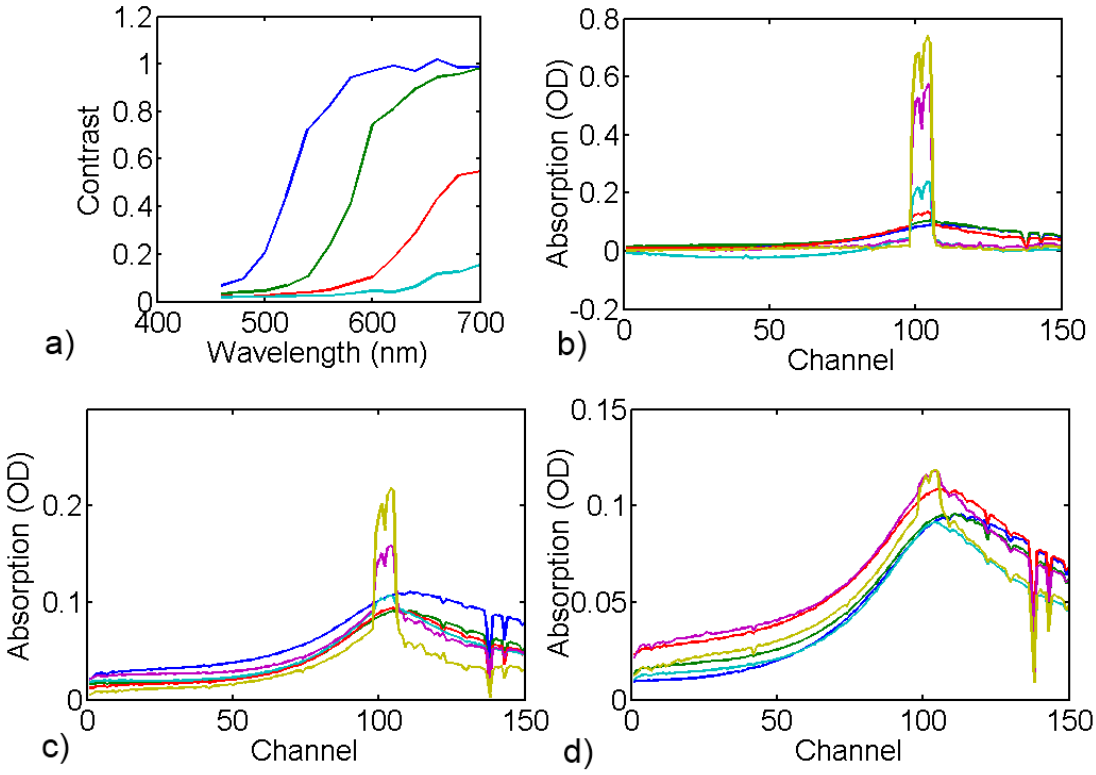

Figure B-4: a) Contrast of a 0.7 mm absorbing rod submerged in 4 levels of scattering at varying wavelengths. blue: 0.15%; green: 0.2%; red: 0.25%;teal: 0.3% Intralipid®. b-d) Computed absorption for 0.7 mm absorbing rod at Intralipid® dilutions of (b) 0.2%, (c) 0.25%, (d) 0.3%. blue: 480nm; green 520 nm; red 560 nm; teal 600 nm; purple: 640 nm; gold 680 nm. FOV ~1.5 cm.

In this experiment, a full field illumination scheme was used. The beam was approximately 1 cm in diameter. In a full field illumination setup, it is possible for light outside the imaging plane to scatter into the AFA and reduce the contrast of the imaging

system. One potential improvement would be to structure the illumination profile so that the illumination source is matched to the input of the AFA. It has been previously demonstrated that a restricted illumination [6,14] can provide an improvement in image contrast.

A previous study on AFA-based angular domain imaging with the same 80 µm x 80 µm x 2 cm AFA has successfully demonstrated the differentiation between tumor and muscle tissue for a 3 mm excised mouse tissue sample [11]. Due to the similarities between the imaging system described in [11] and the imaging system presented in this paper, we believe that the system presented in this paper will also be capable of imaging 3 mm excised mouse tissue samples.

B.4 Conclusions and Future work

Multispectral angular domain imaging was successfully conducted with an OPO-based tunable pulsed laser. A 0.7 mm graphite rod was imaged at four different scattering levels and 13 different wavelengths ranging from 460 nm to 700 nm. The contrast of the graphite rod was computed as the normalized difference between the attenuation due to the quasi-ballistic signal at the target location, and the attenuation due to the scatter signal near the target location. Contrast ranged from 0.07-1 for the 0.15% Intralipid® target, 0.04-0.98 for the 0.2% Intralipid® target, 0.02-0.55 for the 0.25% Intralipid® target and 0.02-0.16 for the 0.3% Intralipid® target. For a given scattering level contrast improved with increasing wavelength. This was due to a decrease in the reduced scattering coefficient of Intralipid® at longer wavelengths. The OPO laser provided the collimation properties of a laser with the spectral resolution necessary to perform hyperspectral imaging. However, the laser was subject to power fluctuations and spatial variations, which necessitated image averaging. The results suggest that the OPO-based angular domain imaging system could be applicable to collecting projection images of thin tissue samples (3-4 mm).

B.5 Acknowledgements

This project was funded by grants from the Natural Sciences and Engineering Research Council (NSERC Discovery), Lawson Health Research Institute (Innovation Prize), and the Canadian Foundation for Innovation (CFI) to J. J. L. Carson. E. Ng was supported by

a Natural Sciences and Engineering Research Council of Canada CGS-M scholarship, a joint Canadian Institutes of Health Research (CIHR) Strategic Training Program in Cancer Research and Technology Transfer (STP CaRTT), London Regional Cancer Program (LRCP) Translational Breast Cancer Research Unit (TBCRU) studentship, and an SPIE student scholarship. F. Vasefi was supported by a scholarship from the LRCP TBCRU post-doctoral fellow award.

B.6 References

1. A. C. Boccara, "Imaging through scattering media," in *Encyclopedia of Modern Optics*, B. D. Guenther, A. Miller, L. Bayvel, and J. E. Midwinter, eds. (Academic Press, 2004), pp. 143.

2. E. M. Sevick, J. R. Lakowicz, H. Szmacinski, K. Nowaczyk, and M. L. Johnson, "Frequency domain imaging of absorbers obscured by scattering," J. Photochem. Photobiol. B. **16,** 169-185 (1992).

3. J. C. Hebden, R. A. Kruger, and K. S. Wong, "Time resolved imaging through a highly scattering medium," Appl. Opt. **30,** 788-794 (1991).

4. S. P. Schilders, X. S. Gan, and M. Gu, "Microscopic imaging through a turbid medium by use of annular objectives for angle gating," Appl. Opt. **37,** 5320-5326 (1998).

5. M. S. Tank and G. H. Chapman, "Micromachined silicon collimating detector array to view objects in a highly scattering medium," Can. J. Elect. & Comp. Eng. **25,** 13 (2000).

6. G. H. Chapman, M. Trinh, N. Pfeiffer, G. Chu, and D. Lee, "Angular domain imaging of objects within highly scattering media using silicon micromachined collimating arrays," Selected Topics in Quantum Electronics, IEEE Journal of **9,** 257-266 (2003).

7. F. Vasefi, B. Kaminska, P. K. Chan, and G. H. Chapman, "Multi-spectral angular domain optical imaging in biological tissues using diode laser sources," Opt. Express **16,** 14456-14468 (2008).

8. F. Vasefi, M. Najiminaini, E. Ng, B. Kaminska, G. H. Chapman, and J. J. L. Carson, "Angular domain transillumination imaging optimization with an ultrafast gated camera," J. Biomed. Opt. **15,** 061710 (2010).

9. F. Vasefi, E. Ng, B. Kaminska, G. H. Chapman, K. Jordan, and J. J. L. Carson, "Transmission and fluorescence angular domain optical projection tomography of turbid media," Appl. Opt. **48,** 6448-6457 (2009).

10. E. Ng, F. Vasefi, B. Kaminska, G. H. Chapman, and J. J. L. Carson,"Contrast and resolution analysis of angular domain imaging for iterative optical projection tomography reconstruction" in *Proc. SPIE* **7557,** 755714(2010).

11. F. Vasefi, M. Najiminaini, E. Ng, A. Chamson-Reig, B. Kaminska, M. Brackstone, and J. J. L. Carson, "Transillumination hyperspectral imaging for histopathological examination of excised tissue," J. Biomed. Opt. **16,** 086014 (2011).

12. A. O. Wist, P. P. Fatouros, and S. L. Herr, "Increased spatial resolution in transillumination using collimated light," IEEE Trans. Med. Imaging **12,** 751-757 (1993).

13. H. J. van Staveren, C. J. Moes, J. van Marie, S. A. Prahl, and M. J. van Gemert, "Light scattering in Intralipid-10% in the wavelength range of 400-1100 nm," Appl. Opt. **30,** 4507-4514 (1991).

14. K. Takagi, Y. Kato, and K. Shimizu, "Extraction of near-axis scattered light for transillumination imaging," Appl. Opt. **48,** D36-44 (2009).

Curriculum Vitae

Name

Eldon Ng

Post-secondary Education and Degrees

Queen's University
School of Medicine
Kingston, Ontario, Canada
2012- M.D.

The University of Western Ontario
Department of Medical Biophysics, Schulich School of Medicine and Dentistry
London, Ontario, Canada
2010-2013 M.Sc.

The University of Western Ontario
Basic Medical Sciences, Department of Medical Biophysics, Schulich School of Medicine and Dentistry
London, Ontario, Canada
2006-2010 B.M.Sc.

Honours and Awards

Joint Translational Breast Cancer Research Unit (TBCRU) and Canadian Institute for Health Research (CIHR) Strategic Training Program (STP) in Cancer Research and Technology Transfer (CaRTT) scholarship
2011-2012

Natural Sciences and Engineering Research Council of Canada (NSERC) Canada Graduate Scholarship (CGS-M)
2010-2011

Schulich Graduate Scholarship
2010-2012

Natural Sciences and Engineering Research Council of Canada (NSERC) Undergraduate Student Research Award (USRA)
2008-2009

SPIE Scholarship
2009-2012

UWO In-Course Scholarship
2007

Dean's Honor List
2006-2010

Western Scholarship of Excellence
2006

Related Work Experience

Research Assistant
The University of Western Ontario
2008-2013

Publications:

Peer Reviewed Manuscipts Published in Refereed Journals

M. Roumeliotis, R. Z. Stodilka, M. A. Anastasio, **E. Ng**, & J. J. L. Carson, "Singular value decomposition analysis of a photoacoustic imaging system and 3D imaging at 0.7 FPS," Opt. Express **19**, 13405-13417 (2011).

F. Vasefi, M. Najiminaini, **E. Ng**, A. Chamson-Reig, B. Kaminska, M. Brackstone, & J. J. L. Carson, "Transillumination hyperspectral imaging for histopathological examination of excised tissue," J. Biomed Optics **16**, 086014 (2011).

F. Vasefi, M. Najiminaini, **E. Ng**, B. Kaminska, G. H. Chapman, J. J. L. Carson, "Angular domain transillumination imaging optimization with an ultrafast gated camera," J. Biomed Optics **15,** 061710 (2010).

E. Ng, F. Vasefi, B. Kaminska, G. H. Chapman, J. J. L. Carson, "Contrast and resolution analysis of iterative angular domain optical projection tomography," Opt. Exp. **18**,19444-19455 (2010).

M. Roumeliotis, R. Z. Stodilka, M. A. Anastasio, G. Chaudhary, H. Al-Aabed, **E. Ng**, A. Immucci, J. J. L. Carson, "Analysis of a photoacoustic imaging system by the crosstalk matrix and singular value decomposition," Opt. Exp **18**, 11406-17 (2010).

F. Vasefi, **E. Ng**, B. Kaminska, G. H. Chapman, K. Jordan, J. J. L. Carson, "Transmission and fluorescence angular domain optical projection tomography of turbid media," Appl. Opt. **48**, 6448-57 (2009).

Manuscripts in preparation

E. Ng, J. J. L. Carson, "Angular domain imaging with a 2D angular filter array," (2013).

E. Ng, J. J. L. Carson, “Two dimensional angular domain imaging with a 3D printed angular filter array,” (2014).

Conference Presentations, Abstracts, and Proceedings

E. Ng, J. J. L. Carson, “Two-dimensional angular filter array for angular domain imaging with 3D printed angular filters,” Proc. SPIE Vol. 8579, 85790W (2013).

E. Ng, J. J. L. Carson, “Resolution analysis of an angular domain imaging system with two dimensional angular filters,” Proc. SPIE Vol. 8579, 857913 (2013).

E. Ng, J. J. L. Carson, “Multispectral angular domain imaging with a tunable pulsed laser light source” Oncology Research & Education day, London, Ontario (2012).

E. Ng, F. Vasefi, J. J. L. Carson, “Multispectral angular domain imaging with a tunable pulsed laser light source,” Proceedings of SPIE Vol. 8225, 82252C (2012).

F. Vasefi, **E. Ng**, M. Brackstone, J. J. L. Carson, “Trans-illumination hyperspectral imaging for histopathological examination of in vitro tissue,” Oncology Research & Education day, London, Ontario, (2011).

E. Ng, F. Vasefi, B. Kaminska, J. J. L. Carson, “Three dimensional angular domain optical projection tomography,” Proceedings of SPIE Vol. 7897, 78970V (2011).

F. Vasefi, M. Najiminaini, **E. Ng**, B. Kaminska, J. J. L. Carson, “Angular-domain spectroscopic imaging of turbid media: derivative analysis,” Proceedings of SPIE Vol. 7897, 78971Q (2011).

Y. Zhang, F. Vasefi, **E. Ng**, A. Chamson-Reig, B. Kaminska, J. J. L. Carson, “Deep illumination angular domain spectroscopic imaging: tissue-mimicking phantom study,” Proceedings of SPIE Vol. 7896, 789634 (2011).

F. Vasefi, M. Najiminaini, **E. Ng**, B. Kaminska, H. Zeng, G. H. Chapman, J. J. L. Carson, “Angle-resolved spectroscopy using a radial angular filter array,” Proceedings of SPIE Vol. 7562, 756209 (2010).

E. Ng, F. Vasefi, B. Kaminska, G. H. Chapman, J. J. L. Carson, "Contrast and resolution analysis of angular domain imaging for iterative optical projection tomography reconstruction," Proceedings of SPIE Vol. 7557, 755714 (2010).

M. Roumeliotis, G. Chaudhary, M. Anastasio, R. Stodilka, A. Immucci, **E. Ng**, J. J. L. Carson, "Analysis of a photoacoustic imaging system by singular value decomposition," Proceedings of SPIE Vol. 7564, 756432 (2010).

F. Vasefi, **E. Ng**, M. Najiminaini, G. Albert, B. Kaminska, G. H. Chapman, J. J. L. Carson, "Angular domain spectroscopic imaging of turbid media using silicon micromachined microchannel arrays," Proceedings of SPIE Vol. 7568, 75681K (2010).

E. Ng, F. Vasefi, B. Kaminska, G. H. Chapman, J. J. L. Carson, "*Hyperspectral angular domain optical imaging*," 4th Annual London Imaging Discovery Workshop (2009).

E. Ng, F. Vasefi, B. Kaminska, G. H. Chapman, J. J. L. Carson, "Image contrast enhancement during time-angular domain imaging through turbid media by estimation of background scattered light," Lawson Research Day (2009).

E. Ng, F. Vasefi, B. Kaminska, G. H. Chapman, J. J. L. Carson, "Image contrast enhancement during time-angular domain imaging through turbid media by estimation of background scattered light," Proceedings of SPIE Vol. 7182, 71821C (2009).

F. Vasefi, **E. Ng**, B. Kaminska, G. H. Chapman, J. J. L. Carson, "Effect of time gating and polarization discrimination of propagating light in turbid media during angular domain imaging (ADI)," Proceedings of SPIE Vol. 7182, 718217 (2009).

F. Vasefi, **E. Ng**, B. Kaminska, G. H. Chapman, J. J. L. Carson, "Angular domain fluorescent lifetime imaging in turbid media," Proceedings of SPIE Vol. 7183, 71830I (2009).